Summer 8-2023

Study of Microphonic Effects on the C100 Cryomodule for High Energy Electron Beam Accelerators

Caleb James Hull
Old Dominion University, chull001@odu.edu

Recommended Citation

Hull, Caleb J.. "Study of Microphonic Effects on the C100 Cryomodule for High Energy Electron Beam Accelerators" (2023). Master of Science (MS), Thesis, Mechanical & Aerospace Engineering, Old Dominion University, DOI: 10.25777/xx52-5f44
https://digitalcommons.odu.edu/mae_etds/365

STUDY OF MICROPHONIC EFFECTS ON THE C100 CRYOMODULE FOR HIGH ENERGY ELECTRON BEAM ACCELERATORS

by

Caleb James Hull
B.S.M.E December 2019, Old Dominion University

A Thesis Submitted to the Faculty of
Old Dominion University in Partial Fulfillment of the
Requirements of the Degree of

MASTER OF SCIENCE

MECHANICAL ENGINEERING

OLD DOMINION UNIVERSITY
August 2023

Approved by:

Tian-Bing Xu (Director)

Thomas Alberts (Member)

Drew Landman (Member)

Geoffrey Krafft (Member)

ABSTRACT

The Continuous Electron Beam Accelerator Facility (CEBAF) at Thomas Jefferson National Laboratory (JLab) is a particle accelerator which can accelerate an electron beam to relativistic speeds and apply the beam onto target samples. The C100 superconducting radio frequency (SRF) cavity is the primary accelerating structure of the C100 cryomodule, one of the many cryomodules which compose the CEBAF linear accelerator. SRF cavities are particularly sensitive to internal and external vibrations that can result in a phenomenon called microphonics which degrade the operational stability of a cryomodule.

The purpose of this thesis is to investigate the significance of mechanical disturbances on the electromagnetic resonant frequency of a C100 SRF cavity. Knowledge of the mechanical resonance of the cavities and cryomodule sheds light into how these disturbances are most easily realized as deformation which causes radio frequency (RF) detuning. Three studies were conducted: the development and hammer test calibration of a Finite Element Analysis (FEA) model of a C100 cavity, the development and hammer test calibration of an FEA model of a C100 cavity string, and the hammer test of the C100-10R cryomodule at the Cryomodule Test Facility (CMTF).

The cavity FEA model was found to accurately predict two modes found in two real cavities in a simply supported configuration. The cavity string FEA model leveraged the calibrated cavity FEA model but was not found to accurately predict the modal behavior of a real cavity string. Even so, the modal behavior of the cavity string inside the C100-10R cryomodule was captured during a hammer test while it was partially assembled.

Finally, the C100-10R cryomodule was placed in the CMTF to study RF detuning. The RF detuning spectra during hammer hits and background noise was captured. The results of the hammer testing indicate two strong peaks at low frequencies (9-10 Hz and 22-23 Hz). These two frequencies were found to be nearly coincident to four instances of mechanical resonance found during the hammer testing done on the partially-assembled C100-10R. Because of this, these two modes are believed to contribute to RF detuning of the cryomodule. This test event also included the testing of the effectiveness of a configuration of BNNT canisters designed to act as dampers. While these tests show promising results, the lurking variables render these tests somewhat inconclusive.

This thesis is dedicated to my family.

This work is supported by the U. S. Department of Energy Graduate Traineeships in Accelerator Engineering and Physics Award No. DE-SC0022309.

This material is based upon work supported by the U.S. Department of Energy, Office of Science, Office of Nuclear Physics under contract DE-AC05-06OR23177.

ACKNOWLEDGEMENTS

To all who have helped me over the course of this project, thank you. In particular:

My committee members for their leadership and expertise.

Thomas Jefferson National Accelerator Facility and the Virginia Innovation Traineeship in Accelerators program for supporting me during this project.

Peter Owen and Tom Powers for teaching me how to perform hammer tests and making the materials available.

Dr. Roy Whitney and Stacy Jarrell of BNNT, LLC for allowing me to study their products.

George Biallas for his expertise.

My family for their support.

NOMENCLATURE

AFC	Adaptive Feedforward Control
ANOVA	Analysis of Variance
BNNT	Boron Nitride Nanotubes
CBETA	Cornell-BNL ERL Test Accelerator
CEBAF	Continuous Electron Beam Accelerator Facility
CEPC	Circular Electron Positron Collider
CMS	Component Mode Synthesis
CMTF	Cryomodule Test Facility
ERL	Cornell Energy Recovery Linac
FEA	Finite Element Analysis
FRF	Frequency Response Function
HOM	Higher Order Mode
Jlab	Thomas Jefferson National Accelerator Facility, Jefferson Labs
LCLS-II	Linac Coherent Light Source II
LFD	Lorentz Force Detuning
LLRF	Low Level Radio Frequency
LoF	Lack of Fit
MAC	Modal Assurance Criterion
MIF	Mode Indicator Function
MIF_1	Normal Mode Indicator Function
NSCL	National Superconducting Cyclotron Laboratory
ODS	Observed Deflection Shape
PI	Prediction Interval
PMAC	Partial Modal Assurance Criterion
PRESS	Prediction Error Sum of Squares
QWR	Quarter Wave Resonator

RF	Radio Frequency
SRF	Superconducting Radio Frequency (Cavities)
XMAC	Directional MAC calculated in the X direction
YMAC	Directional MAC calculated in the Y direction
ZMAC	Directional MAC calculated in the Z direction

TABLE OF CONTENTS

Page

LIST OF TABLES

Table Page

LIST OF FIGURES

Figure Page

Figure Page

Figure Page

CHAPTER 1

INTRODUCTION

1.1 Background

Particle accelerators are some of the most complex machines ever made. Even so, the underlying principle of particle acceleration is fundamentally very simple: leverage an electromagnetic field to apply forces onto charged particles such that they can be accelerated, focused into a beam, and used for specific purposes. The range of uses for such devices is as wide as the imagination, ranging from scientific discovery, medical treatment, and entertainment [1].

Figure 1:Cryomodules in the CEBAF Linear Accelerator (Image used Courtesy of Jefferson Lab)

The Continuous Electron Beam Accelerator Facility (CEBAF) at Thomas Jefferson National Laboratory (Jefferson Labs or JLab) is a particle accelerator which can accelerate an electron beam to relativistic speeds and apply the beam onto target samples. This allows scientists to study “the basic building blocks of matter within the nucleus” [2]. This facility contains two linear accelerators made of a small variety of cryomodules (shown in Figure 1), including the C100 cryomodule (shown in Figure 2) which is to be studied as a part of this thesis.

Figure 2: C100-10R Cryomodule (Image used Courtesy of Jefferson Lab)

The primary accelerating structure of a C100 cryomodule is the C100 superconducting radio frequency (SRF) cavity (shown in Figure 3). These cavities are electromagnetically resonant at a specific frequency (1497 MHz) so that as much electromagnetic energy from the incoming radio frequency (RF) waves is transferred to the electron beam as achievable. To minimize the losses in this energy transfer due to surface resistance in the cavity walls, the C100 cavities are made of niobium and cryogenically cooled to 2 Kelvin which allows the cavities to become superconductors. Unfortunately, the use of superconductive materials in RF cavities reduces their RF bandwidth which makes them sensitive to disturbances [3-6]. This thesis focuses on microphonics, a particular type of mechanical disturbance which originates from vibrations internal or external to the cryomodule. To study how vibrations can most easily affect these cavities, mechanical resonance in a C100 cryomodule was studied leveraging Modal Analysis using Finite Element Analysis (FEA) models.

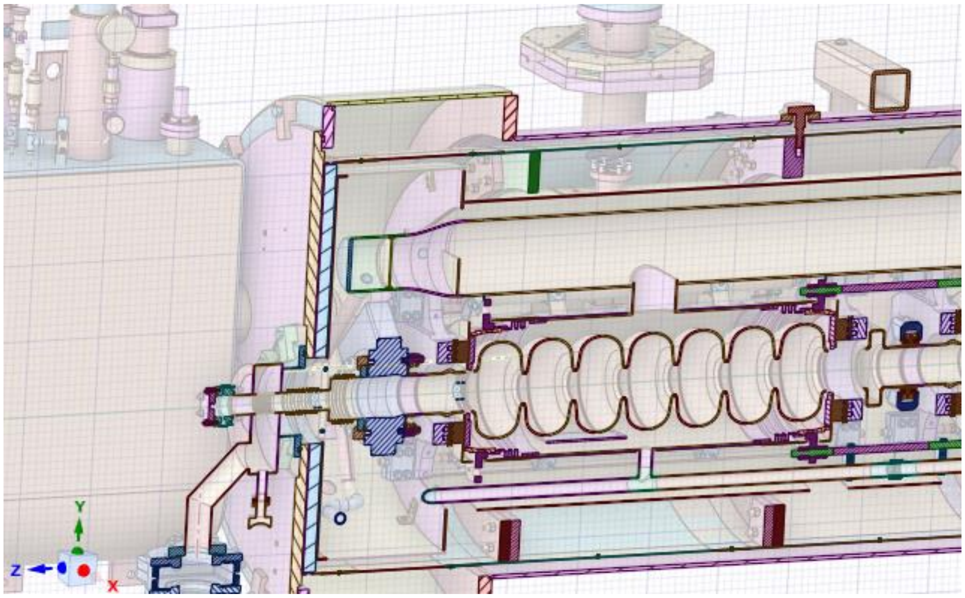

Figure 3: Cross-Section of a C100 Cryomodule (Image used courtesy of ANSYS, Inc.)

1.2 Literature Review

The development of particle accelerators is as complex as the machines themselves, leaving behind a rich and fascinating history. Rutherford's experimentation in the early 1900's led to a need for high-energy beams [1]. Different solutions to this problem were implemented, but the first resonant accelerators began development in the late 1920's [1]. These accelerators leveraged normal conducting RF cavities, often made of copper. Restraints due to surface resistance in these cavities led to the application of superconducting materials in RF resonators [3]. While the implementation of superconducting materials reduces the surface resistance of the cavity and increases the quality factor Q, it also decreases the RF bandwidth [3-6]. Cavities with small bandwidths are sensitive to disturbance [4, 5]. Slater's Perturbation Theorem describes how the RF resonant frequency of a cavity changes when it is disturbed [7-11]:

$$\frac{\Delta\omega}{\omega} = -\frac{\int_S dS\, \vec{n}(\vec{r}) \cdot \vec{\xi}(\vec{r}) \left[\frac{\mu_0}{4} H^2(\vec{r}) - \frac{\varepsilon_0}{4} E^2(\vec{r})\right]}{\int_V \left[\frac{\mu_0}{4} H^2(\vec{r}) + \frac{\varepsilon_0}{4} E^2(\vec{r})\right]}$$

This shows that the disturbed frequency is a function of the electromagnetic content of the cavity and its disturbed geometry. From a mechanical point of view, it is of interest to identify the different ways in which this geometry can become disturbed.

During operation, the inside of the SRF cavities is kept under a very high vacuum while the outside is immersed in a bath of liquid helium. Pressure fluctuations in the helium bath can directly disturb cavity shape and volume. A correlation between the pressure fluctuations of the liquid helium and RF detuning in Linac Coherent Light Source II (LCLS-II) cryomodules was identified by Contreras-Martinez [9]. Posen and Liepe [12] leveraged FEA to predict the RF detuning caused by pressure fluctuations in order to optimize the design of cavities at the Cornell

Energy Recovery Linac (ERL). Zhang et al [13] simulated and studied these effects on cavities in the Circular Electron Positron Collider (CEPC). Schappert [14] notes that feedback control methods can be used to help mitigate the effects of helium pressure fluctuations.

Thermoacoustic oscillations in liquid helium can generate noise within a cryomodule. This occurs when a pipe or channel has a large temperature difference and the warm end is closed [15]. Luck and Trepp characterized the mechanism that causes these effects leveraging a thermodynamic heat engine approach [15-17]. Hansen et al observed thermoacoustic oscillations in the LCLS-II [18].

Currents within the cavity walls can interact with the magnetic field from the RF and apply a Lorentz force on the wall [9, 19, 20] which leads to changes in cavity geometry and RF resonant frequency. This effect is called Lorentz Force Detuning (LFD). LFD was related to Slater's Perturbation Theorem by Kandil [10]. LFD was observed in the Horizontal Test Bed during a test at Jefferson Labs [21]. The LFD transfer function that relates the RF detuning as caused by a modulated RF field was characterized by Delayen [11]. A method of characterizing the LFD transfer function leveraging a grey-box model was described by Qiu et al [22]. A state space model of this effect was described by Echevarria et al [23] and Keikha et al [24].

The cavities can also be disturbed by external mechanical disturbances called 'microphonics' [11]. Mechanical resonance in structures becomes critical in this area of study because small amounts of energy can cause significant deflections. Resonance in SRF cavities and the structures around them can therefore lead to the cavity RF detuning. Simrock et al [25] developed a control system to reduce the effects of microphonics on a Quarter Wave Resonator (QWR) using a piezoelectric tuner. Banerjee et al [4] implemented both passive and active vibration mitigation techniques to improve cryomodule performance at the Cornell-BNL ERL Test Accelerator (CBETA). An active noise control algorithm was developed using a slow and fast tuner. Contreras-Matrinez [9] studied microphonics mechanical excitations and stochastic microphonics in LCLS-II cryomodules. Active resonance control algorithms for the SRF cavity was developed and implemented using slow and fast tuners. Delayen [11] describes methods for characterizing microphonics. Kandil [10] developed an Adaptive Feedforward Control (AFC) algorithm to mitigate disturbances on SRF cavities, including microphonics. Usher [5] developed a Low-Level RF (LLRF) controller using an AFC algorithm to mitigate disturbances in the National Superconducting Cyclotron Laboratory (NSCL). Zimmermann [26] proposed and simulated a control system for mitigating mechanical disturbances on radiation detectors. Keikha et al [24] developed and simulated an RST feedback control system to mitigate microphonics and LDF. This study included an FEA Modal Analysis of a TRIUMF 9 cell cavity. Schappert [14] described an active resonance control system developed at Fermi National Accelerator Laboratory. Davis et al [21] studied the effect of different excitation types on the Horizontal Test Bed at Jefferson Labs. This includes studying background vibrations, mechanical sine sweeps, RF pulses, and hammer hits. Davis et al [27] built a one-dimensional FEA model of a C100 cryomodule cavity string assembly at Jefferson Labs which predicted three critical vibration modes.

1.3 Thesis Statement

Key works with respect to this thesis are Davis et al [21] and Davis et al [27]. Davis et al [21] identifies FEA as a method to shorten the design cycle of solutions. Later, Davis et al [27] built a simplified FEA model of a C100 cavity string, the assembly of parts containing the cavities and the systems immediately outside of them. Three vibration modes were identified as a part of this study. It is the purpose of this thesis to advance these ideas by correlating mechanical resonance behavior in a C100 cryomodule with the RF detuning of its cavities leveraging FEA. Specifically, this thesis will follow the development of a more detailed cavity string FEA model that could be used as a virtual test bed for prototype assessment. Additionally, one such prototype solution was investigated. BNNT, LLC proposed a set of canisters which are designed to serve as vibration attenuators. The effects of these devices on a C100 cryomodule were experimentally captured.

1.4 Thesis Organization

This thesis is organized into five chapters. Chapter 1 provides an introduction and background to this thesis. Chapter 2 describes the methods used during this project, specifically detailing the dynamics of vibrations, methods of developing, calibrating, and statistically describing FEA models. Chapter 3 describes three studies carried out to support this thesis. This includes two FEA modeling efforts each accompanied by an appropriate testing effort and a test of a cryomodule in an application-representative environment used to assess the BNNT canisters. Chapter 4 summarizes the results of these modeling and testing efforts and draws conclusions. Chapter 5 summarizes this thesis and provides recommendations to continue research in this area.

CHAPTER 2

METHODS

Resonance is a type of structural behavior in which the application of a small excitation at a specific frequency produces significant motion. This is critical in the case of SRF cavities as cavity deflection leads directly to RF detuning, which hinders the performance of the cavity and the rest of the cryomodule. It is therefore desired to study the resonance behavior in the C100 cryomodule to identify how this behavior correlates to RF detuning. Given the complex geometry, extreme temperature distributions, and diversity of materials in a C100 cryomodule, it is of great value to leverage FEA to shed light in this area.

A review of modal analysis is provided in Section 2.1. Quantitative methods for comparing models to test data are provided in Section 2.2. An introduction into hammer test methods is provided in Section 2.3. A review of the FEA methods used during this thesis is provided in Section 2.4. Finally, a review of methods used during the Design of Experiments is provided in Section 2.5.

2.1 Vibrations and Modal Analysis

This section is a summary of modal analysis described by Brandt [28]. To begin, consider a finite set of masses $[M]$ acted upon by external forces $\{F(t)\}$ and the springs $[K]$ and dampers $[C]$ which connect them. The motion $\{u(t)\}$ of these masses is related according to the linear differential equation [28]:

$$[M]\{\ddot{u}\} + [C]\{\dot{u}\} + [K]\{u\} = \{F(t)\} \tag{2.1.1}$$

For simplicity, the damping matrix $[C]$ is considered insignificant and will be removed, though the validity of this proof will be maintained. The undamped system is described:

$$[M]\{\ddot{u}\} + [K]\{u\} = \{F(t)\} \tag{2.1.2}$$

Free vibration occurs when the system is able to move without the application of external forces. This is mathematically described by arguing that the force vector $\{F(t)\}$ is a zero vector, that is [28]:

$$[M]\{\ddot{u}\} + [K]\{u\} = \{0\} \tag{2.1.3}$$

The Laplace Transform is found [28]:

$$[M](s^2\{U\}) + [K]\{U\} = \{0\} \tag{2.1.4}$$

$$(s^2[M] + [K])\{U\} = \{0\} \tag{2.1.5}$$

This equation is placed into a form in which the eigenvalues and eigenvectors can be found [28]:

$$[M^{-1}](s^2[M] + [K])\{U\} = \{0\} \tag{2.1.6}$$

$$([M^{-1}][K] + s^2[I])\{U\} = \{0\} \tag{2.1.7}$$

$$[A] = [M^{-1}][K] \tag{2.1.8}$$

$$\lambda = -s^2 \tag{2.1.9}$$

$$([A] - \lambda[I])\{U\} = \{0\} \tag{2.1.10}$$

Now that this equation is in this form, the system can be solved to yield the rth eigenvalues λ_r and eigenvectors $\{\Psi\}_r$ [28].

$$([A] - \lambda_r [I])\{\Psi\}_r = \{0\} \tag{2.1.11}$$

To interpret these results, consider the following [28]:

$$s = i\omega \tag{2.1.12}$$

$$\lambda = -s^2 = -(i\omega)^2 = \omega^2 \tag{2.1.13}$$

$$\omega_r = \pm\sqrt{\lambda_r} \tag{2.1.14}$$

That is, ω_r represents the frequency at which the system is expected to be able to experience unforced vibrations and $\{\Psi\}_r$ is the deflection that is expected to be observed at that frequency. It is worthy of note that the nature of $\{\Psi\}_r$ as an eigenvector indicates that any scalar multiple of $\{\Psi\}_r$ is also a solution to the rth eigenvalue problem. As such, the benefit of calculating $\{\Psi\}_r$ is not the exact value of any particular element within the vector, but the relative magnitude of one element with respect to all others – that is – its shape. It is these two ideas, ω_r (mode frequency) and $\{\Psi\}_r$ (mode shape), which analytically define a vibration mode.

While ω_r and $\{\Psi\}_r$ are interesting pieces of information when studying resonance, they do not describe the system response at all frequencies. To do this, the modal coordinates $\{q(t)\}$, $\{Q(s)\}$ are defined [28]:

$$\{u(t)\} = [\Psi]\{q(t)\} \tag{2.1.15}$$

Here, the mode shape matrix $[\Psi]$ is defined as a matrix containing a sufficient list of mode shape vectors $\{\Psi\}_r$ [28].

$$[\Psi] = [\{\Psi\}_1 \quad \{\Psi\}_2 \quad \dots \quad \{\Psi\}_r \quad \dots \quad \{\Psi\}_k] \tag{2.1.16}$$

The modal coordinate vector is similarly defined [28]:

$$\{q(t)\} = \begin{vmatrix} q_1 \\ q_2 \\ \cdots \\ q_r \\ \cdots \\ q_k \end{vmatrix} \tag{2.1.17}$$

By Equation $(2.1.15)$, the time-domain deflection response $\{u(t)\}$ is a linear combination of the mode shapes. The Laplace Transform of this equation is found:

$$\{U(s)\} = [\Psi]\{Q(s)\} \tag{2.1.18}$$

The frequency-domain deflection response is therefore a linear combination of the mode shapes. This is an important statement because Equation $(2.1.18)$ provides a conceptual description of the system at all frequencies once $[\Psi]$ and $\{Q(s)\}$ are known. Knowing this, Equation $(2.1.15)$ is substituted into Equation $(2.1.18)$.

$$[M][\Psi]\{\ddot{q(t)}\} + [K][\Psi]\{q(t)\} = 0 \tag{2.1.19}$$

$$s^2[M][\Psi]\{Q(s)\} + [K][\Psi]\{Q(s)\} = 0 \tag{2.1.20}$$

$$(s^2[M] + [K])[\Psi]\{Q(s)\} = 0 \tag{2.1.21}$$

$$[M^{-1}](\, s^2[M] + [K])[\Psi]\{Q(s)\} = 0 \tag{2.1.22}$$

$$([M^{-1}][K]{+}s^2[I])[\Psi]\{Q(s)\} = 0 \tag{2.1.23}$$

$$([A] - \lambda[I])[\Psi]\{Q(\lambda)\} = 0 \tag{2.1.24}$$

This equation can be solved for its eigenvalues. Since the system matrix $[A]$ is identical to Equation (2.1.8), the eigenvalues of this equation are the same as that found earlier, that is, λ_r. Given that the system and eigenvalues are identical, the eigenvectors can also be said to be identical, that is:

$$[\Psi]\{Q(\lambda_r)\} = \{\Psi\}_r \tag{2.1.25}$$

Therefore, the eigenvectors (mode shapes) of the system are realized as the unforced deflection response at frequencies predicted by the eigenvalues (the associated mode frequencies).

To find these mode frequencies, consider the same system under forced conditions by taking the Laplace Transform of Equation (2.1.2) to find the transfer matrix:

$$(s^2[M] + [K])\{U\} = \{F\} \tag{2.1.26}$$

When a force is applied at a mode frequency:

$$\{U\} = ([K] - \lambda_r[M])^{-1}\{F\} = [H]\{F\} = \left\{\frac{const.}{0}\right\} = \{\infty\} \tag{2.1.27}$$

Here, the transfer matrix $[H]$ is defined as the transformation from applied forces to displacement. The elements H_{PQ} within this matrix refer to the displacement of the Pth point due to the Qth force in terms of a frequency-dependent complex number. In the case of the forced response of this system at a resonant frequency, values of H_{PQ} would theoretically become infinite. Equation $(2.1.27)$ indicates that as the transfer matrix $[H(i\omega_r)]$ becomes infinite, $\{U(i\omega_r)\}$ would also become infinite. Since only the solutions to Equation $(2.1.3)$ exhibit this property, the deflections $\{U(s \neq i\omega_r)\}$ will be finite in value. This makes the mode frequencies unique in the real world in that they are the frequencies where the response at those frequencies appears as a globally significant local maximum, or 'peak'. Per Equation $(2.1.11)$, the deflection of the system at these frequencies is representative of mode shapes. As such, the theoretical modal properties of a system are physically realizable and potentially measurable. In the broader picture, these properties embody the ideas of resonance.

2.2 Model Comparison Tools

With the modal properties defined and established as physically realizable in Section 2.1, some mathematical tools are required to work with them in real data. Two tools are presented here: the Normal Mode Indicator Function (MIF_1) and the Modal Assurance Criterion (MAC). The former is used in conjunction with peak finding to determine the value of mode frequencies and the latter is used to compare two mode shapes. Throughout this project, MATLAB [29] was used to calculate and graph these values.

2.2.1 Normal Mode Indicator Function (MIF_1)

While it is predicted that vibrational systems would naturally resonate at their mode frequencies and nowhere else under free vibration conditions, this is not always observed in the real world. For example, evidence of modal behavior (peaks in magnitude) is found in numbers and places which do not match model predictions. Perhaps also – for a variety of reasons – an expected mode shape might not be adequately excited such that it produces clear enough signals to be found as a peak. One method of dealing with these issues is the use of a Mode Indicator Function (MIF) [28]. While there are different MIF functions, the Normal MIF (MIF_1) [28] is used for this analysis.

$$MIF_1 = \frac{\sum_P \left[\left|Re\big(H_P(f)\big)\right|^2\right]}{\sum_P[|H_P(f)|^2]} \tag{2.2.1}$$

In this case, the term $H_P(f)$ refers to an element in the broader transfer matrix $[H]$ as defined in Equation $(2.1.27)$ in the specific case where one force (the hammer) acts on the system. This function works on the principle that "off the natural frequencies of a structure, the FRF [Frequency Response Function] is approximately real, whereas exactly at the undamped natural frequency, it is purely imaginary" [28]. Considering this, it is reasoned that the MIF_1 is an estimate of the real mode frequencies by providing the analyst with a measurement of the significance of the imaginary response on the whole system response as a function of frequency. Evidence of modal behavior is found where the MIF_1 function experiences a 'dip' in value where the imaginary component becomes locally more significant. As a part of this analysis, sets of modal frequencies were selected from test data leveraging this tool and the magnitude peaks.

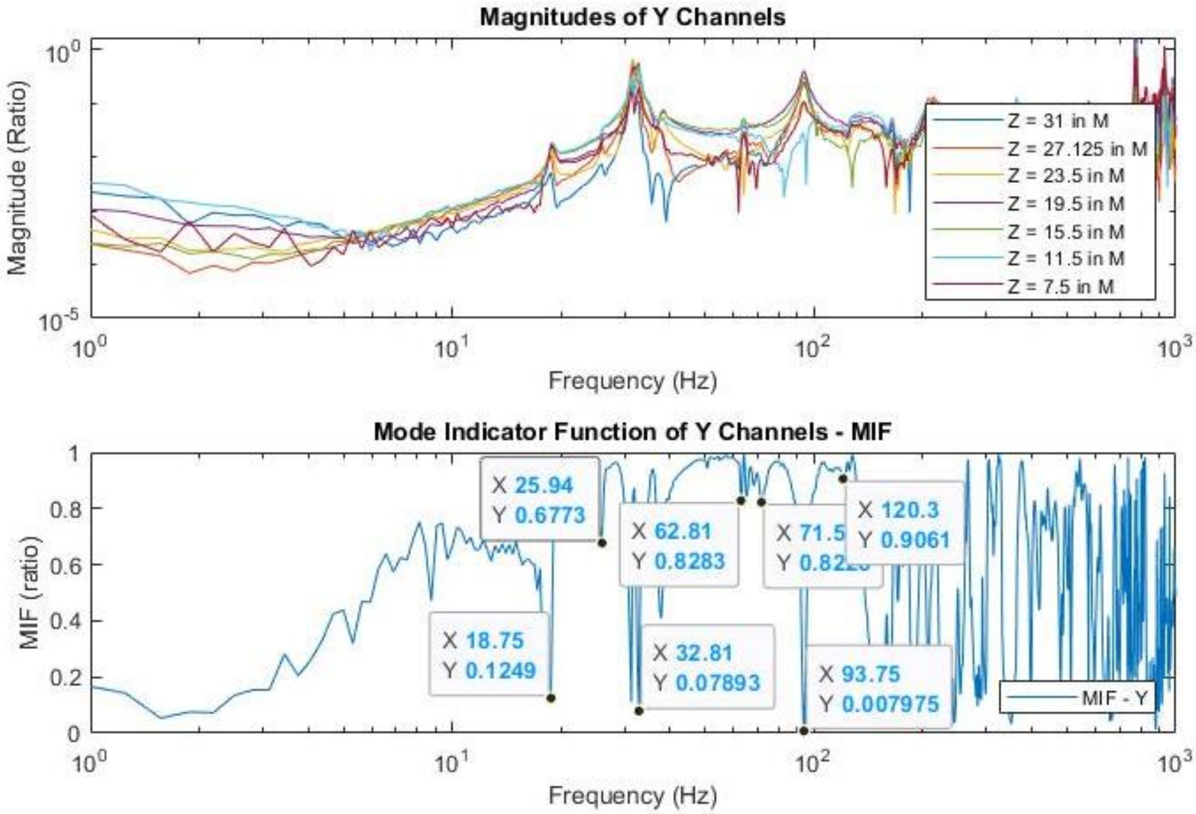

Figure 4: Example of the Normal MIF (MIF_1) and Response Peaks

An example of the mode frequency selection process is shown in Figure 4. In this case, a C100 cavity is arranged in a hammer test configuration in which accelerometers were placed at key locations to capture its resonance behavior. The upper graph presents the spectra of vertical acceleration experienced by each of the sensors. Clear peaks in magnitude can be seen which indicate the values of mode frequencies. The spectrum of the MIF_1 is presented in the lower graph shows dips in the function which provides additional evidence that many of these peaks represent modes.

2.2.2 Modal Assurance Criterion (MAC)

This analysis requires a quantitative comparison of mode shapes to characterize how close they match, especially when concerned with comparing a response shape from test data – called an observed deflection shape (ODS) – at a particular frequency (ODS frequency) to the corresponding analytical mode shape from a model. First, the ODS shape is normalized to form the test vector $\{\psi\}_t$ which takes the form of a complex column vector. The analytical vector $\{\psi\}_r$ is generated in a model and takes the form of a real-valued column vector of the same size. The Modal Assurance Criterion (MAC) is used to compare these two vectors in the form of a single scaler. Brandt defines the MAC [28] as:

$$MAC_{tr} = \frac{\left|{\psi_t}^H \psi_r\right|^2}{\left({\psi_t}^H \psi_t\right)\left({\psi_r}^H \psi_r\right)} \qquad (2.2.2)$$

2.3 A Note on the Conduct of a Hammer Test

This section contains a mathematical justification for the use of hammer tests and a verification that the data collected from such a test can be used for the purposes of modal analysis. A note is provided which describes an important consideration related to the directional nature of excitations delivered by a hammer strike. As a mitigation to this issue, the method of calculating the MAC was adjusted. Additionally, a note is provided which describes the origin and mitigation of reflected asymmetric mode shapes in test data.

2.3.1 Basic Function of a Hammer Test

In Section 2.1, it was determined that the mode frequencies and shapes are physically realizable. Hammer tests are used to capture this modal behavior in real systems by exciting the modes with a small amount of energy and studying the free vibration response. To do this, the system is arranged such that it can freely vibrate (that is, it is an unforced system) once energy is imparted onto it. Accelerometers or like devices are affixed to the system in such a quantity and configuration that critical features in analytical mode shapes will be adequately captured. Energy is imparted onto the system in the form of a hammer strike and the acceleration of the sensors is recorded long enough to capture the transient, free vibration response. This time-domain data is fed through a discrete function (for example, a Discrete Fourier Transform or a Fast Fourier Transform) which produces the frequency spectrum of their motion.

Hammer tests were performed on two C100 representative SRF cavities and the C100-10R cryomodule. Also, a load cell was affixed to the tip of the hammer used to impart energy onto the systems. The forces on the tip of the hammer were sampled and the frequency spectrum of each hammer hit was determined. This information was used to bound the region of frequencies which could be said to be ‘effectively excited’ during the tests. The data acquisition device used to capture the data in each test formed $H_i(f)$, an estimate of a Frequency Response Function (FRF) using the frequency spectra of each of the accelerometers and the hammer force spectrum.

$$H_i(f) = \frac{A_i(f)}{F(f)} \frac{[g]}{[lbF]} \qquad (2.3.1)$$

While it may appear that this function is a transfer function of acceleration with respect to a specific input force, it is not. It would be an issue if it were, in that $H_i(f)$ would represent forced response, not unforced modal response. To demonstrate that $H_i(f)$ is applicable to this test, it is derived. To begin, the ideal deflection of each sensor when vibrating in one direction can be described as simple harmonic motion.

$$u_i(t) = M_i \sin(\omega t + \varphi_i) \tag{2.3.2}$$

The acceleration of this motion is found with the second time derivative.

$$a_i(t) = -\omega^2 M_i \sin(\omega t + \varphi_i) = -\omega^2 u_i(t) \tag{2.3.3}$$

The acceleration functions of each accelerometer can be placed into a vector $\{a(t)\}$. After a Laplace Transform of this vector, it can be concluded that the frequency-domain acceleration vector at a given frequency is a scalar multiple of the frequency-domain deflection vector:

$$\{A(s)\} = -\omega^2 \{U(s)\} \tag{2.3.4}$$

The data acquisition device used this data to generate an estimate of the transfer functions between the hammer hit forces and the accelerations of each of the accelerometers. While the exact methods by which the data acquisition device performed this estimation were not investigated, a transfer function between the hammer hit forces and the accelerometer accelerations can be described as:

$$\{|H_i(f)|\} = \begin{Bmatrix} |H_1(f)| \\ \dots \\ |H_n(f)| \end{Bmatrix} = \frac{1}{|F(f)|} \begin{Bmatrix} |A_1(f)| \\ \dots \\ |A_n(f)| \end{Bmatrix} = \frac{(2\pi f)^2}{|F(f)|} \begin{Bmatrix} |U_1(f)| \\ \dots \\ |U_n(f)| \end{Bmatrix} \tag{2.3.5}$$

$$\{\angle H_i(f)\} = \begin{Bmatrix} \angle H_1(f) \\ \dots \\ \angle H_n(f) \end{Bmatrix} = \begin{Bmatrix} \angle A_1(f) - \angle F(f) \\ \dots \\ \angle A_n(f) - \angle F(f) \end{Bmatrix} = \begin{Bmatrix} \angle U_1(f) - \pi - \angle F(f) \\ \dots \\ \angle U_n(f) - \pi - \angle F(f) \end{Bmatrix} \tag{2.3.6}$$

This shows that the function $H_i(f)$ of Equation (2.3.1) cannot be said to be a true transfer function; rather, it is representative of the free vibration acceleration frequency response normalized by the excitation applied to the system. As such, the data collected represents the spectrum of ODS shapes.

Given this, consideration must be given to the eigenvector $\{\Psi\}_r$. In an FEA model with many nodes, the efficient modeler will ensure that there will exist nodes which can be used to represent the motion of the accelerometers used in hammer tests. Once the analytical mode shape $\{\Psi\}_r$ of the whole system is found, the predicted motion of the accelerometers can be extracted from $\{\Psi\}_r$ to yield a more condensed analytical mode shape $\{\psi\}_r$. Furthermore, if a particular frequency in the test data f_t coincides with the r^th^ analytical mode frequency, it is expected that the deflection $\{U(f_t)\}$ would be a scalar multiple of this truncated analytical mode shape $\{\psi\}_r$ and – from the above equations – it follows that the function $\{H(f_t)\}$ would be as well:

$$\{|H_i(f_t)|\} = \begin{Bmatrix} |H_1(f_t)| \\ \dots \\ |H_n(f_t)| \end{Bmatrix} = \frac{(2\pi f_t)^2}{|F(f_t)|} \begin{Bmatrix} |U_1(f_t)| \\ \dots \\ |U_n(f_t)| \end{Bmatrix} \propto \begin{Bmatrix} |\psi_1|_r \\ \dots \\ |\psi_n| \end{Bmatrix}_r \qquad (2.3.7)$$

$$\{\angle H_i(f_t)\} = \begin{Bmatrix} \angle H_1(f_t) \\ \dots \\ \angle H_n(f_t) \end{Bmatrix} = \begin{Bmatrix} \angle U_1(f_t) - \pi - \angle F(f_t) \\ \dots \\ \angle U_n(f_t) - \pi - \angle F(f_t) \end{Bmatrix} \cong \begin{Bmatrix} \angle\{\psi_1\}_r + \varphi_{ref} \\ \dots \\ \angle\{\psi_n\}_r + \varphi_{ref} \end{Bmatrix} \qquad (2.3.8)$$

These two conclusions (that $\{H(f)\}$ represents unforced ODS deflections and that a vector of the ODS $\{H(f_t)\}$ is analogous to $\{\psi\}_r$) demonstrate that the collected data in the form of the function $\{H(f)\}$ contains the modal behavior of the system. An example of an ODS shape (blue) being compared to a truncated analytical mode shape (red) is presented in Figure 5.

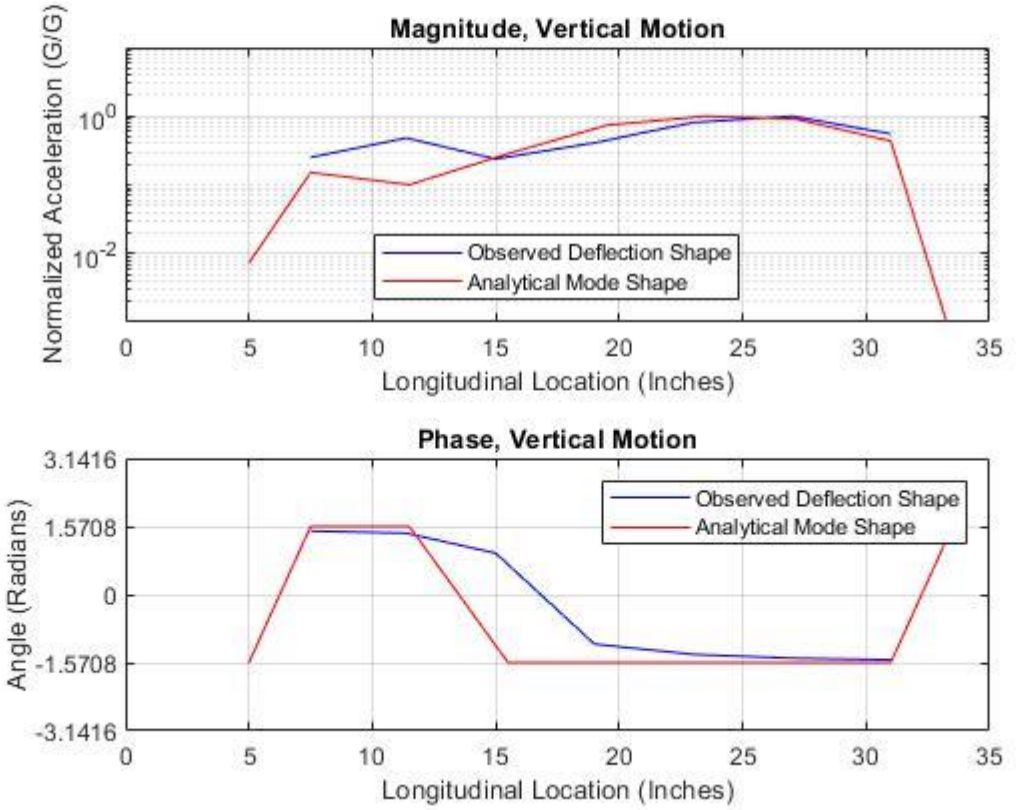

Figure 5: Example Comparison of ODS Shape and Analytical Mode Shape

2.3.2 A Note on Directional Preferences

The earlier introduction of the MAC is a critical point in this analysis in that it allows two modes shapes to be compared. While the observed resonant frequencies can be compared to analytical mode frequencies leveraging one-dimensional descriptive statistics, the ODS vector $\{H(f_t)\}$ cannot be so easily compared to the analytical mode shapes $\{\psi\}_r$. However, the reduction in information from a pair of vectors to a single scalar simplifies this issue. More importantly, the introduction of the MAC allows for the simultaneous comparison of the ODS shape and frequency to an analytical mode shape and frequency using scalar quantities; in short, similar modes are now comparable.

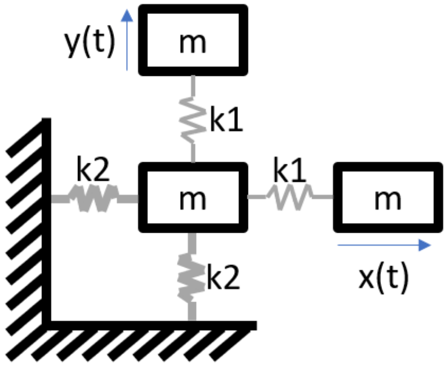

Figure 6: Justification for Directional MACs

With the above in mind, consider the system described in Figure 6. In this case, there are three objects of equal mass that are constrained in different ways. The upper-most mass is only allowed to move vertically, the right-most mass is only allowed to move horizontally, and the mass in the lower left corner can translate horizontally and vertically. The masses are connected as shown with two types of springs: springs marked k1 are relatively weak while the springs marked k2 are – say – 100 times stronger than k1. The value of k2 was chosen to be sufficiently strong such that – while the corner mass is technically part of the overall dynamic system – it only moves a negligible amount at any time. This allows for the transfer of energy imparted onto the corner mass to the upper-most and right-most masses without its motion being significant to any mode shape. Additionally, the restriction of motion on the corner mass will prevent its inertia from applying significant forces onto the other masses. For this illustration, the insignificance of the acceleration and displacement of the corner mass allow it to be removed from the analysis of vibration modes. The reduced system is described using Equation $(2.1.3)$ as:

$$\begin{bmatrix} m & 0 \\ 0 & m \end{bmatrix} \begin{Bmatrix} \ddot{x}(t) \\ \ddot{y}(t) \end{Bmatrix} + \begin{Bmatrix} k_1 & 0 \\ 0 & k_1 \end{Bmatrix} \begin{Bmatrix} x(t) \\ y(t) \end{Bmatrix} = \begin{Bmatrix} 0 \\ 0 \end{Bmatrix} \tag{2.3.9}$$

This system is solved for its eigenvalues:

$$\left(\frac{k_1}{m} \begin{vmatrix} 1 & 0 \\ 0 & 1 \end{vmatrix} + s^2 \begin{vmatrix} 1 & 0 \\ 0 & 1 \end{vmatrix} \right) \begin{Bmatrix} x \\ y \end{Bmatrix} = \begin{Bmatrix} 0 \\ 0 \end{Bmatrix}; \quad s = \pm i \sqrt{\frac{k_1}{m}}; \quad \lambda_{1,2} = \frac{k_1}{m} \tag{2.3.10}$$

Two identical mode frequencies are found:

$$f_{1,2} = \sqrt{\lambda_{1,2}} = \sqrt{\frac{k_1}{m}}, \sqrt{\frac{k_1}{m}} \tag{2.3.11}$$

Their mode shapes are found with the eigenvectors:

$$\left(\frac{k_1}{m}\begin{vmatrix}1 & 0\\ 0 & 1\end{vmatrix}+\left(-i\sqrt{\frac{k_1}{m}}\right)^2\begin{vmatrix}1 & 0\\ 0 & 1\end{vmatrix}\right)\begin{Bmatrix}x\\ y\end{Bmatrix}=\begin{Bmatrix}0\\ 0\end{Bmatrix} \tag{2.3.12}$$

$$2\frac{k_1}{m}\begin{vmatrix}1 & 0\\ 0 & 1\end{vmatrix}\begin{Bmatrix}x\\ y\end{Bmatrix}=\begin{Bmatrix}0\\ 0\end{Bmatrix} \tag{2.3.13}$$

$$\{\Psi\}_{1,2}=\begin{Bmatrix}1\\ 0\end{Bmatrix},\begin{Bmatrix}0\\ 1\end{Bmatrix} \tag{2.3.14}$$

Consider how this type of system would be studied in a hammer test. In this experiment, accelerometers are attached to the upper-most and the right-most masses such that the motion x and y are measured. Furthermore, let it be so that the operator can only apply a hammer hit to the corner mass, not the upper-most or right-most masses. While it would be ideal to excite the two modes with hammer strikes such that each mode perfectly embodies the mode shapes, this is not always possible. In this case, the corner mass would have to have energy deposited exactly along the vertical or horizontal directions for this to occur.

To illustrate the significance of this point, let it be so that the operator was not able to strike the system ideally as described. Under such conditions, the hammer hits will inevitably excite both modes simultaneously. In the realistic but extreme example of this, both the upper-most and the right-most masses are excited equally. Such response could be represented leveraging Equation (2.3.7) as the following:

$$\left\{\left|H_i\left(f_1=\sqrt{\frac{k_1}{m}}\right)\right|\right\}=\begin{Bmatrix}|H_1(f_1)|\\ \dots\\ |H_n(f_1)|\end{Bmatrix}=\frac{(2\pi f_1)^2}{|F(f_1)|}\begin{Bmatrix}1\\ 1\end{Bmatrix} \tag{2.3.15}$$

The MAC calculation between the ODS vector $\begin{Bmatrix}1\\1\end{Bmatrix}$ of this case and the first analytical mode shape $\begin{Bmatrix}1\\0\end{Bmatrix}$ (or the second mode shape) will suffer.

$$MAC = \frac{\left|\{1 \quad 1\}\begin{Bmatrix}1\\0\end{Bmatrix}\right|^2}{\left(\{1 \quad 1\}\begin{Bmatrix}1\\1\end{Bmatrix}\right)\left(\{1 \quad 0\}\begin{Bmatrix}1\\0\end{Bmatrix}\right)} = .5 \qquad (2.3.16)$$

It is not the purpose of this example to describe a system with a pair of coincident modes (the modal coordinates described in Eq $(2.1.15)$ would be of assistance in that case); rather, it is to demonstrate how serious the directional deposition of energy by the hammer is to this analysis. This issue would be compounded if instead of the two accelerometers in the above test system, a whole group of accelerometers were spread across a system having more complex mode shapes and the energy imparted onto this system was not consistently applied. Hammer hits are more chaotic than not; control over the directional deposition of energy onto the system is hard to establish. In the above example, the ODS was considered above to be $\begin{Bmatrix}1\\1\end{Bmatrix}$, but a slight rotation of the hand could have resulted in $\begin{Bmatrix}1\\.9\end{Bmatrix}$ or $\begin{Bmatrix}.9\\1\end{Bmatrix}$, leading to more problems in the MAC calculations. This directional preference in the deposition of energy by the hammer and the noted unpredictability is a serious issue and would almost be grounds to not use the MAC.

To help deal with directional preferences associated with the deposition of energy by the hammer and the mathematical realization of the mode shapes, the MACs were calculated and studied on the mode shapes in the principal directions (X – broadside, Y – vertical, and Z – axial) of the test articles as shown in Figure 7. This is an application of the Partial Modal Assurance Criterion (PMAC) as described by Allemang [30]. The whole-eigenvector MACs were calculated, but the calculated values were found to be extraordinarily low even in cases where the Directional MACs were found to be quite high. It was reasoned that this behavior was caused by the directional preferences described above and it was decided to not use the whole-eigenvector MACs for this analysis but to leverage the Directional MACs instead.

2.3.3 A Note on Data Reflections

An additional artifact that these tests are studies of transient response in real systems is the presence of reflections in the data. Specifically, consider the profile of the C100 cavity presented in Figure 7. In many ways, it is symmetrical though there are differences in the geometry at the extremities. Though this system is largely symmetrical, asymmetrical mode shapes (like that shown in Figure 5) were predicted in the FEA model and observed in the hammer test. One curious observation with respect to the collected data was that these asymmetric mode shapes were at times observed exactly as predicted by the model and at other times found to be reflected longitudinally. It was reasoned that the general symmetry of the configuration allowed this asymmetric mode shape to exist in both forms at the same frequency. If both forms of the mode shape can exist at the same frequency, it is reasonable to conclude that the data acquisition system used in this test would not be able to choose between the two forms, thus the reported mode shape would be somewhat arbitrarily chosen. This was further compounded by the fact that it was found that the observed responses were not reflected in all axes at the same time. For example, the horizontal and axial data could be found as predicted by the FEA model, but the vertical data was captured in a reflected form.

To mitigate this issue, the reflected mode shapes needed to be un-reflected. Since the sensors were placed in a longitudinally symmetrical configuration, the response can be corrected by simply reversing the order of the responses. To determine if a particular part of the data set needed to be un-reflected, the Directional MAC was calculated with both the original and reflected data set. Whichever yielded the highest Directional MAC value was considered to be the correct form.

Figure 7: Profile of a C100 Cavity (Image used Courtesy of Jefferson Lab)

2.4 FEA Methods

With respect to the broader question of resonance on the cryomodule while in use, it would be convenient to attach accelerometers onto the cavities, perform a hammer test or record pure noise, study the spectra, identify a clear problem area, and identify a clear solution. Unfortunately, the cryogenic environment around the cavities (achieving temperatures around 2 K) is too extreme for sensors available at this time. Because of this, it is not possible to get raw acceleration (or any other form of deflection) data from the cavities. Additionally, it would be convenient to study a cryomodule while it was partially assembled and perform the same analysis. While this was done, there are several variables which must be considered:

- The temperature variation from warm (~300K) to cold (~2K) is very large. Temperature has real effects on material properties. There are many complex parts in a cryomodule and they are made of many different materials. How does this temperature variation change resonance behavior in the cryomodule?
- The study of resonance is convenient for studying the behavior of vibrational systems because resonance readily transforms applied energy into displacement. However, if there exists a strong enough off-resonant excitation, the system can become disturbed and adjusting resonance could become insufficient to solving the problem. How can system response due to resonance and strong off-resonance excitation be distinguished?

To answer these questions, one must have a model of the system. While it is not possible to answer these questions through data collection on the system while in use, one can build an FEA model of the system and perform a modal analysis. If the model can be shown to be accurate using warm material properties, it might be usable to make predictions using cryogenic material properties. This can be used to predict the resonant behavior in the cryomodule when cryogenically cooled and to distinguish the responses from resonant behavior and strong off-resonant excitation. FEA models of the C100 SRF cavities and cavity string were developed for this purpose. This section introduces the FEA methods that were used as a part of this effort and includes an introduction to element theory (Section 2.4.1); an introduction to shell and beam elements (Section 2.4.2); an introduction to Component Mode Synthesis (Section 2.4.3); an introduction to symmetrical and asymmetrical boundary conditions; and a summary discussing the use of FEA for modal analysis (Section 2.4.4).

2.4.1 Standard Elements and Methods

FEA models describe structures as a set of discrete parts called ‘elements’ through a process called ‘meshing.’ Each element is connected to adjacent elements at their corners called ‘nodes.’ Each node represents one ‘subsystem’ in the vibrational system and the mesh of nodes represents the vibrational system itself. Each node is connected to adjacent nodes using equations of motion for springs, masses, and dampers. All of the equations from these connections are formed into the linear differential equation described in Equation (2.1.3) [31]. Various methods for solving for the eigenvalues and eigenvectors are then employed to find the mode shapes and frequencies of the meshed geometry [31].

The primary objective of FEA modeling with respect to modal analysis is the correct description of mass and stiffness of complex geometry. Mass is generally determined through material density and the geometry of the mesh. Stiffness in an FEA model is derived from material properties, geometry of the mesh, and the composition of the mesh itself. The effect of damping was not specifically addressed in this study though there do exist Damped Modal Analysis techniques [31].

For the sake of this thesis, the material properties were provided by Jefferson Labs and were assumed to be correct without further investigation. This was done for two specific reasons: while the provided theoretical material properties and the real material properties might be slightly different, the variation in material properties – and therefore modal properties – between warm and cold conditions was assumed to be sufficiently accurate for analysis and that the impact of the error in material properties was less damaging to the results than a bad mesh. Since the geometries of the cavities and components in the cryomodule were provided by Jefferson Labs, this too was considered to be accurate enough to not perform further adjustment. The variable that was adjusted in the model was the mesh.

The development of a mesh is the way that a modeler communicates to the solver what components in the system geometry are important. For example, a ½" hole in the middle of a ⅛" x 1" x 4" bar might be considered significant due to loss of mass, stress concentration, local reduction in stiffness, etc. On the other hand, a C100 cryomodule is a relatively large structure and it can be reasoned that the major contributions to stiffness and mass in these structures comes from the relatively large components (like the vacuum vessel, space frame, cavity string, etc.), not the relatively small objects (screws, nuts, bolts, washers, etc.). The hole in the aforementioned bar – and sometimes the bar itself – can be neglected from a model of this size without serious impact to the results. This process, called 'defeaturing,' gives the modeler flexibility in what is considered significant during the pursuit of an accurate model.

With respect to the mesh itself, there are ways to assess its quality regardless of the geometry. Specifically, element quality is defined according to the following [32]:

$$Quality = C\left(\frac{area}{\sum(EdgeLength)^2}\right) \tag{2.4.1}$$

$$Quality = C\left(\frac{volume}{\sqrt{\left[\sum(EdgeLength)^2\right]^3}}\right) \tag{2.4.2}$$

The value of C is specially defined for different element shapes. These quantities provide an estimate of how skewed an element is. For example, a hexahedral element which is highly elongated and sheared will have low quality due to the ratio of low volume to large edge lengths; conversely, a perfect cube will have the highest ratio between volume and edge length and thus high quality. The minimum element quality is a helpful metric in that it provides a measure of the mesh overall. With respect to this, the default Target Element Quality (minimum acceptable element quality) is .05 [32]. A spatial distribution of element quality can help the modeler identify regions in geometry which need to be re-meshed, defeatured, or removed.

The pursuit of a mesh with high element quality is often limited by node count. While inundating a geometry with an extraordinary quantity of elements might improve element quality, the model matrices will increase significantly in size and result in a model which is time-consuming, not runnable, or not any more valuable than a smaller model. It then becomes the objective of the modeler to build a mesh which has a balance between a high quality, low node count, and acceptable model predictions. This balance has brought about useful developments of FEA elements and methods discussed in the following sections.

2.4.2 Beam and Shell Elements

Consider how one might model a piece of printer paper leveraging FEA. Should one desire a mesh with perfect mesh quality using hexahedrons, all of the side lengths of the elements would have to be near the thickness of the piece of paper. An incredible quantity of elements would be required to satisfy this requirement for only a single layer of elements. This issue is further compounded should nonplanar loading and response be studied. For example, a modeler would desire multiple layers of elements to describe bending which would further shrink element size to provide the needed element quality. Put simply, this is not a reasonable strategy.

Shell elements can be used to solve this issue. Within Ansys® SpaceClaim [33], a modeler can simplify the geometry of a thin component into a surface body having a constant thickness. These bodies can be meshed with shell elements which include information related to the shell thickness [34]. With this, a single layer of elements of a reasonable quantity and size can provide accurate results for nonplanar loading and response. Similar problems and solutions exist for beams; a beam-like object, having significant length in comparison to other dimensions and having a constant cross-section, can be modeled as a line body and meshed with beam elements to the same effect [34].

2.4.3 Condensed Geometry.

Within Ansys® Mechanical [35] is the ability to perform substructure analysis. Once a system, being composed of a set of objects, has been properly meshed, a group of those objects can be selected to be represented as a substructure of the system. By doing this, the elements within the substructure are replaced with a single superelement which will act as a mathematical equivalent to the nodes which interface to the replaced elements [31, 34]. This has many benefits, including a reduced model size, lower runtime, and the ability to study and calibrate models of substructures in isolation before the final analysis is done.

One particularly useful application of substructure analysis is Component Mode Synthesis (CMS) [31]. After a substructure has been made, a modal analysis up to a specified number of modes is performed on it. Once this is done, the substructure is replaced by the superelement equivalent. By doing so, the modal properties of the substructure will continue to contribute to the overall modal behavior of the larger system even though the substructure elements have been replaced. This makes it possible to perform modal analysis on large systems – say, a cryomodule – without having to compromise on the accuracy of critical subsystems – say, an SRF cavity.

2.4.4 Symmetrical and Anti-symmetrical Boundary Conditions

When working with symmetrical models under symmetrical loading conditions, it is at times useful to leverage the symmetry of the situation to predict the behavior of that system, assuming that its behavior will also be symmetrical. Ansys® Mechanical [35] has the ability to define and work with symmetrical and anti-symmetrical systems and configurations leveraging a type of boundary condition called a ‘symmetry region’. For example, a symmetry region leveraging symmetry is defined across a plane such that “out-of-plane [nodal] displacements and in-plane [nodal] rotations are set to zero” [34]. This allows models to be divided in half thereby significantly reducing the node count, model size, and run time. An example of a symmetry boundary condition is shown in Figure 8 where the plane of symmetry is shown in red.

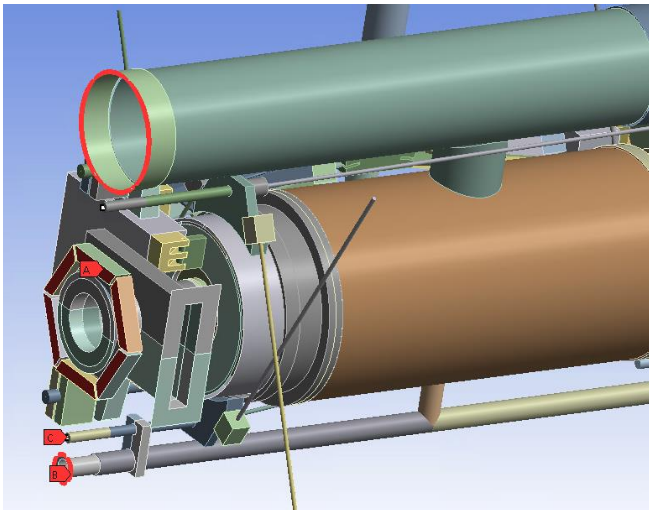

Figure 8: Plane of Symmetry on the Cryomodule Model (Image used courtesy of ANSYS, Inc.)

2.5 Design of Experiments

2.5.1 Method Justification

The primary output of modal analysis is a description of the vibration modes: a simultaneous realization of a specific mode shape at a specific mode frequency. For a modal model of a system in some configuration to be accurate, both shape and frequency must be predicted correctly. For the purposes of calibration, it is necessary to quantify the error in the output of a model when compared to reality such that this error can be minimized. A statistical method is therefore required with respect to mode shapes and frequencies for modal analysis.

One key idea presented in Section 2.1 is that the modal behavior of a system in a particular configuration is a property of that system in that configuration. This implies that the vibration modes should be the same no matter how they are brought about. Specific to hammer tests, it is expected that the modal behavior of a structure does not change depending on the hammer hit location. While this may be theoretically true, it is critical to verify that this is so. This section discusses statistical methods used to study these types of claims. Section 2.5.2 introduces least squares regression models and the Analysis of Variance (ANOVA). Section 2.5.3 describes metrics used to assess the quality of these models. Section 2.5.4 describes how the modes can be used.

2.5.2 Least Squares Regression Modeling and ANOVA

When working to characterize a system whose behavior is governed by certain treatments, it is valuable to develop a statistical model which describes the behavior of that system as a function of those treatment parameters. One effective way of doing this is to develop a least squares regression model. The following is a summary of a method described by Montgomery [36]. To begin, consider a linear statistical model in the form of an effects model [36].

$$y_{ij} = \mu + \tau_i + \epsilon_{ij} \begin{cases} i = 1,2, \dots, a \\ j = 1,2, \dots, n \end{cases} \tag{2.5.1}$$

In this model, μ represents the overall mean, τ_i is the ith treatment effect, y_{ij} is the jth measurement of the response y under the ith treatment, and ϵ_{ij} is the random error associated with y_{ij} [36]. It is desired to estimate the parameters μ and τ_i such that the error in this model is minimized. To do this, the Least Squares Estimation technique begins by characterizing the error of the model L as the sum of squares of the errors ϵ_{ij} [36]:

$$L = \sum_{i=1}^{a}\left[\sum_{j=1}^{n}\left[{\epsilon_{ij}}^{2}\right]\right] = \sum_{i=1}^{a}\left[\sum_{j=1}^{n}\left[\left(y_{ij} - \mu - \tau_i\right)^{2}\right]\right] \qquad (2.5.2)$$

In order to have an optimally accurate model, the error L must be minimized with respect to the parameters μ and τ_i. A minimization implies that the partial derivative of L with respect to these variables must be zero at the particular optimal values $\hat{\mu}$ and $\widehat{\tau_\iota}$, that is [36]:

$$0 = \left.\frac{\partial L}{\partial \mu}\right|_{\hat{\mu},\widehat{\tau_\iota}} = -2\sum_{i=1}^{a}\left[\sum_{j=1}^{n}\left[\left(y_{ij} - \hat{\mu} - \widehat{\tau_\iota}\right)\right]\right] \qquad (2.5.3)$$

$$0 = \left.\frac{\partial L}{\partial \tau_i}\right|_{\hat{\mu},\widehat{\tau_\iota}} = -2\sum_{j=1}^{n}\left[\left(y_{ij} - \hat{\mu} - \widehat{\tau_\iota}\right)\right] \qquad (2.5.4)$$

These equations can be simplified to become [36]:

$$\sum_{i=1}^{a}\left[\sum_{j=1}^{n}\left[y_{ij}\right]\right] = an\hat{\mu} + n\sum_{i=1}^{a}\left[\widehat{\tau_\iota}\right] \qquad (2.5.5)$$

$$\sum_{j=1}^{n}\left[y_{ij}\right] = n\left(\hat{\mu} + \widehat{\tau_\iota}\right) \qquad (2.5.6)$$

These two represent $a + 1$ equations called the ‘least squares normal equations’ [36]. Unfortunately, these equations are not linearly independent and one more equation is required. A constraint that is often applied to overcome this issue is the following [36]:

$$\sum_{i=1}^{a}\left[\widehat{\tau_\iota}\right] = 0 \qquad (2.5.7)$$

Leveraging this constraint, the following conclusions can be made [36]:

$$\hat{\mu} = \frac{1}{an}\sum_{i=1}^{a}\left[\sum_{j=1}^{n}[y_{ij}]\right] \tag{2.5.8}$$

$$\hat{\tau_i} = \frac{1}{a}\sum_{j=1}^{n}[y_{ij}] - \frac{1}{an}\sum_{i=1}^{a}\left[\sum_{j=1}^{n}[y_{ij}]\right] \tag{2.5.9}$$

2.5.3 Assessment of Statistics Models

Now that a statistical model has been built, it is necessary to assess its quality and draw conclusions. The R^2 metric and its various instantiations are commonly used to assess the quality of such a model. The standard definition of R^2 is found [36]:

$$R^2 = \frac{SS_{Model}}{SS_{Total}} \tag{2.5.10}$$

This is an appropriate method of model assessment in that "it measures the proportion of total variability explained by the model" [36] Another form used is the Adjusted R^2 which is defined [36]:

$$R^2_{Adj} = 1 - \frac{SS_e / df_e}{SS_{Total} / df_{Total}} \tag{2.5.11}$$

This metric is defined because this value decreases as insignificant terms are added. As such, significant variability between R^2_{Adj} and R^2 is a good indicator that insignificant terms have been added [36]. Finally, the Predicted R^2 is defined [36]:

$$R^2_{Pred} = 1 - \frac{PRESS}{SS_{Total}} \qquad (2.5.12)$$

Note here that the Prediction Error Sum of Squares (PRESS) follows a very specific definition:

> To calculate PRESS, we select an observation – for example, i. We fit the regression model onto the remaining $n - 1$ observations and use this equation to predict the withheld observation y_i. Denoting this predicted value $\hat{y}_{(i)}$, we may find the prediction error for point i as $e_i = y_i - \hat{y}_{(i)}$. The prediction error is often called the ith PRESS residual. This procedure is repeated for each observation $i = 1, 2, \dots, n$, producing a set of n PRESS residuals $e_{(1),}\, e_{(2)}, \dots, e_{(n)}$. Then the PRESS statistic is defined as the sum of squares of the n PRESS residuals as in: [36]

$$PRESS = \sum_{i=1}^{n} \left[y_i - \hat{y}_{(i)}\right]^2 \qquad (2.5.13)$$

“A model with a small PRESS indicates that the model is likely to be a good predictor” [36] which indicates that a model with a high R^2_{Pred} will be as well.

2.5.4 Output of a Statistics Model

As mentioned, there are two driving desires behind this application of the Design of Experiments: to quantify the error in the FEA models and to demonstrate that the various treatments in this experiment did not significantly affect the modal behavior of the system. Since the information studied here involves describing the modal behavior of a real system, it is necessary to quantitatively capture the error information on the mode shapes and frequencies of that system in its configuration. While this is simple to do with scalar quantities (like the mode frequency), the mode shape is a vector.

The FEA model can be used to make predictions with respect to a particular mode. The predicted mode shape can be proposed as a reference and the Directional MACs can be calculated between this reference and the ODS shapes extracted from test data at peaks near the FEA-predicted mode frequency. This allows the error in the mode shape to be quantified as a scaler, which can be imported into a statistics model. Such a model would therefore make predictions related to the significance of the treatments in changing the observed mode shape away from the FEA-predicted reference. If the FEA-predicted reference is a good match to reality, the statistics model should predict that the Directional MAC values would be above a desired tolerance (say, .8). Mode frequencies are much simpler to explain: if the FEA-predicted mode frequency falls within the Prediction Interval (PI) of the observed mode frequencies, it can be argued that an acceptable match has been found. If the regression models for a particular mode indicate that its mode frequency and all Directional MAC values indicate a sufficient match, the mode can be said to be sufficiently predicted. To determine if the treatments had a significant effect on the modal behavior of the system, standard ANOVA techniques in Table 1 can be applied [36].

Table 1: ANOVA Table

Source of Variation	Sum of Squares	Degrees of Freedom	Mean Square	F$_0$
Between Treatments	$SS_{Treat} = n\sum_{i=1}^{a}\left[\hat{\tau}_i^{\,2}\right]$	$a-1$	MS_{Treat}	$F_0 = \frac{MS_{Treat}}{MS_E}$
Error (within treatments)	$SS_E = SS_T - SS_{Treat}$	$na-a$	MS_E	
Total	$SS_T = \sum_{i=1}^{a}\left[\sum_{j=1}^{n}\left[\left(y_{ij}-\hat{\mu}\right)^2\right]\right]$	$na-1$		

Based on these definitions, it can be said that the treatments were significant to the modal behavior if [36]:

$$F_0 > F_{\alpha,\alpha-1,N-a} \tag{2.5.14}$$

CHAPTER 3

STUDIES

At its core, this thesis is an investigation into the significance of mechanical disturbances on the RF resonant frequency of the C100 SRF cavities such that problems caused by this effect can be mitigated. If it can be demonstrated that RF detuning follows the behavior of mechanical resonance in the cryomodule, it can be argued that the mitigation of resonance would lead to a mitigation of RF detuning. By studying the mode shapes and frequencies in the cryomodule and cavities, specific mitigation strategies to resonance can be proposed and targeted towards specific problem areas.

As a part of this thesis, modal analysis was used to study resonance in C100 SRF cavities and cryomodules to shed light in this area. Specifically, FEA models were developed within Ansys® Mechanical [35] to estimate the vibration mode shapes and frequencies of the cavities and cryomodules. Each FEA modeling effort was accompanied by a calibration leveraging a hammer test of a real system. This was done to compare each model to reality and mathematically assess its accuracy. Finally, a test which was designed to specifically measure RF detuning as caused by mechanical disturbances in a cryomodule while in use was conducted. This test was used to assess the effectiveness of the canisters developed by BNNT, LLC. that was proposed as a solution to the observed problems.

3.1 Study 1: Cavity Model

3.1.1 Model Justification

There are tens of thousands of components within a C100 cryomodule, most of which are not significant to the study of its resonance. However, the SRF cavities are especially important because the cavities can transform mechanical disturbances into RF detuning. The deflection of the cavities caused by a disturbance – and the modal properties which characterize how those deflections are realized – is therefore a critical piece of knowledge in this puzzle. To shed light on this, an accurate FEA model needs to be made and calibrated.

3.1.2 Model Development

Though the cavities are composed of some irregular shapes, there are many geometrical simplifications which can be made. Figure 9 shows a real C100 SRF cavity (#C100-01) in a hammer test configuration and Figure 10 shows the same cavity in the same configuration modeled in FEA. These SRF cavities are largely made from metal sheets, yielding a geometry that resembles thin plates. Shell elements were used for all components in this model except for some small parts of the Higher Order Mode (HOM) can assemblies which were left as solid elements. In the end, this model had 41,686 nodes and 32,859 elements.

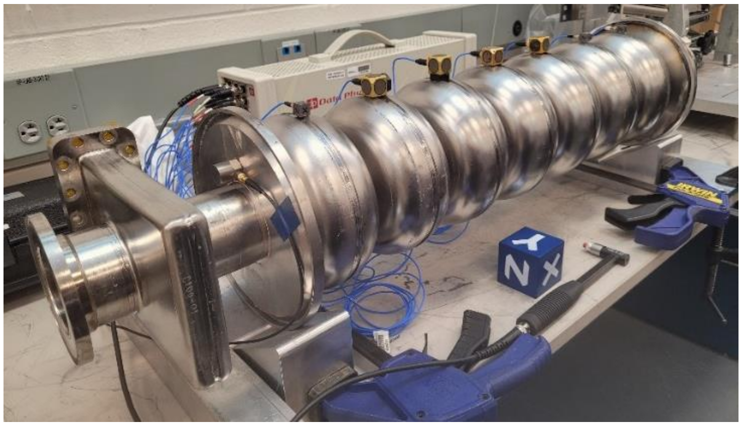

Figure 9: C100-01 SRF Cavity (Image used Courtesy of Jefferson Lab)

Figure 10: Modeled C100 SRF Cavity (Image used courtesy of ANSYS, Inc.)

The primary objective of this modeling effort to develop an accurate mesh. Since the SRF cavities are approximately cylindrical, it is reasonable to expect that the mode shapes would generally be transverse and compression mode shapes. To capture this motion in a hammer test, it is desired to place the accelerometers on the cavity along its length as shown in Figure 9. It is not possible to achieve this configuration while the helium vessel is installed; therefore, this test is not doable while the cavity is a part of a whole cryomodule. To mitigate this constraint, the cavities were tested in isolation in a simply-supported configuration shown in Figure 9. The FEA model developed in Ansys® Mechanical [35] was then used to predict the mode shapes of this configuration in order to develop an accurate mesh. Modes up to 100 Hz were considered which includes the first seven modes. These mode frequencies are listed in Table 2. The nodes shown in Figure 11 were selected to represent the truncated analytical mode shape and were extracted for each mode.

Table 2: Cavity Mode Frequencies

Mode	Mode Frequencies (Hz)
1	17.367
2	26.543
3	35.838
4	64.202
5	68.075
6	93.115
7	108.31

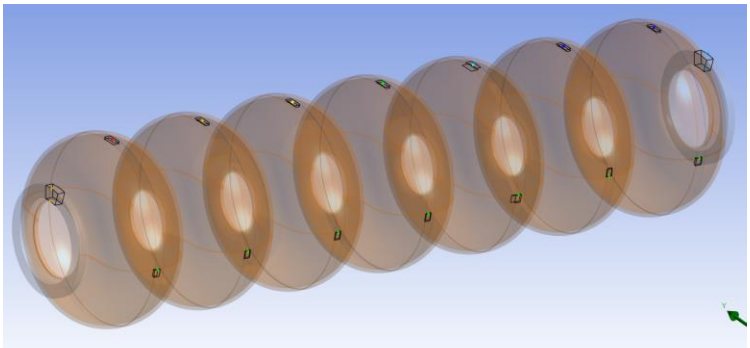

Figure 11: Cavity Model Prediction of the Accelerometer Motion (Image used courtesy of ANSYS, Inc.)

3.1.3 Model Calibration

Once a model begins producing reasonable output, it is necessary to calibrate it. It is first necessary to quantify the error between the model and reality. This error can then be used in an experiment of sorts to vary the parameters within the model to minimize this error and produce a sufficiently accurate model. Since the output of a modal model of a system is the mode shapes and frequencies of that system, it is necessary to quantify and minimize the error in both results in order to achieve calibration. Since this model is a modal model, the methods described in Section 2.5 can be used.

3.1.3.1 Test Configuration

As explained in Section 2.3, hammer tests are convenient for determining the modal behavior of a system. To collect information related to the modal characteristics of a real cavity, a series of hammer tests was performed on a pair of C100-representative cavities (#C100-01 and

#PJN7-1). The cavities were arranged in the simply-supported configuration on V blocks as shown in Figure 12. Seven 3-axis accelerometers and two 1-axis accelerometers were affixed to the cavity and oriented according to the principal directions (X – broadside, Y – vertical, and Z – axial) as indicated by the blue coordinate cube. Two sensor configurations were used as shown in Figure 12 (Top configuration) and Figure 13 (Side configuration). Sets of data were collected by striking the cavity with a special hammer having a load cell placed behind its rubber tip that allows the analyst to study the frequency profile of the energy imparted by the hammer onto the cavity. Five points on the cavity were chosen to be struck which were believed to sufficiently excite the modes of the cavities as shown in Figure 12.

Figure 12: C100-01 Cavity Hammer Strike Points (Image used Courtesy of Jefferson Lab)

To collect the data, the data acquisition device was programmed with a trigger on the hammer load cell such that it would start to record the accelerometer motion as soon as a force limit was met. After a hit, the motion of the accelerometers was then captured for a preset amount of time as the cavity experienced unforced vibration as in Equation (2.3.3). In so doing, the frequency response was captured and analyzed as described in Section 2.3. A set of ten such recordings were done using a particular strike point and the spectra of these recordings were used to produce one averaged spectrum of the set. It is important to note that this spectrum was of the form of a transfer function between the accelerometer motion and the hammer similar to that described in Equation (2.3.1). Two such averaged spectra were generated per strike point; that is, each strike point was excited twenty times per cavity per sensor configuration.

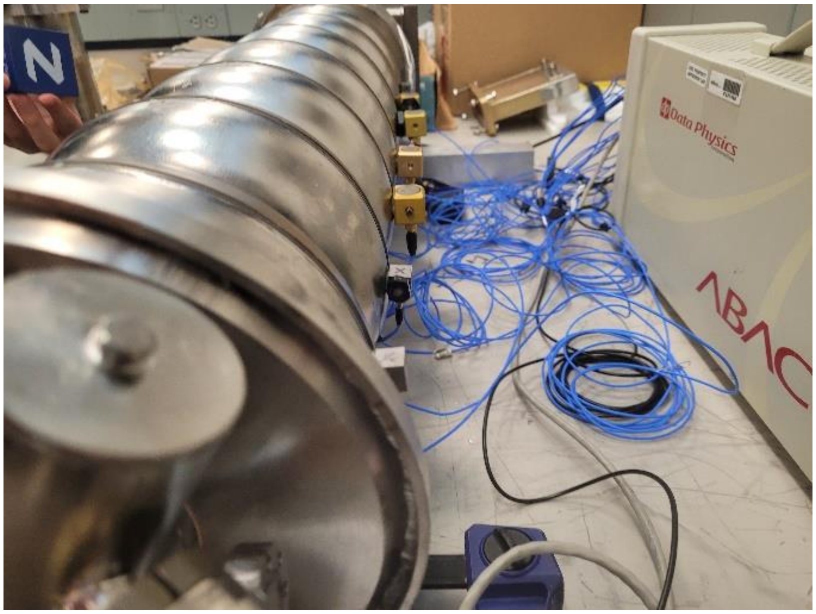

Figure 13: Accelerometers Affixed to the Side (Image used Courtesy of Jefferson Lab)

3.1.3.2 Data Analysis

With the data from the hammer test captured, it is necessary to extract the modal behavior of the system usable for calibration – that is, mode shapes and frequencies. The method leveraging the Normal MIF (MIF_1) as described in Section 2.2.1 was used to identify where in the spectra modes could be found. Each averaged spectrum (120 spectra total) was reviewed in this way. The first seven observed resonant frequencies which were reasonably close to the seven mode frequencies predicted by the FEA model were selected (40 sets of 7 frequencies). Once the resonant frequency was selected, the truncated ODS shape was extracted as described in Equations $(2.3.7)$ and $(2.3.8)$. These ODS shapes, being analogous to the model mode shapes, can be compared to the analytical mode shapes leveraging the methods described in Section 2.2.2 and Section 2.3.2. Knowing this, the Directional MACs (XMAC, YMAC, and ZMAC) were calculated on each extracted ODS shape. Once this was done, the error in the two response variables from the FEA model (mode shape and frequency) can be quantified for each mode in each averaged spectrum. Since there was a great amount of data collected and this data was collected under a wide variety of conditions, it was necessary to statistically describe the data as a whole.

As described in Section 2.5, the Directional MACs can be used to quantitatively indicate where the FEA mode shapes match the experimentally ODS shapes at a selected resonant frequency with a scalar quantity. One-dimensional descriptive statistics can be used to compare the modal behavior of a system to a model by looking at the statistical behavior of the Directional MACs and mode frequencies. It can therefore be argued that a modal model of a system is accurate if the Directional MACs between the analytical mode shapes and the ODS shapes are on average above a chosen limit – say, .80 – and that the predicted mode frequencies are representative of the observed resonant frequencies. Once the estimates of the mode frequencies are found, the FEA models can be adjusted and the model can be said to be calibrated.

A map of response types is provided in Figure 14. There are four distinct regions formed by two boundary types. The MAC limit is chosen by the analyst and represents the degree to which the predicted mode shapes are allowed to differ from the ODS shapes in the test data. The region above this limit represents where the ODS shape was found to acceptably match the analytical mode shape; the region below this limit represents where it was not. The Frequency Outlier Limit is determined after the observed resonant frequencies are statistically described and is derived from the definition of outliers as prescribed by the statistical distribution used. The region within these limits represents the range of frequencies where the studied instance of resonance was found; the regions outside of these limits represents where it was not found. The region bounded by both the MAC limit and the Frequency Outlier Limit represents where the analytical mode shape accurately represents the ODS shapes and the associated resonant frequencies were observed. In short, it is a statistical description of the observed mode.

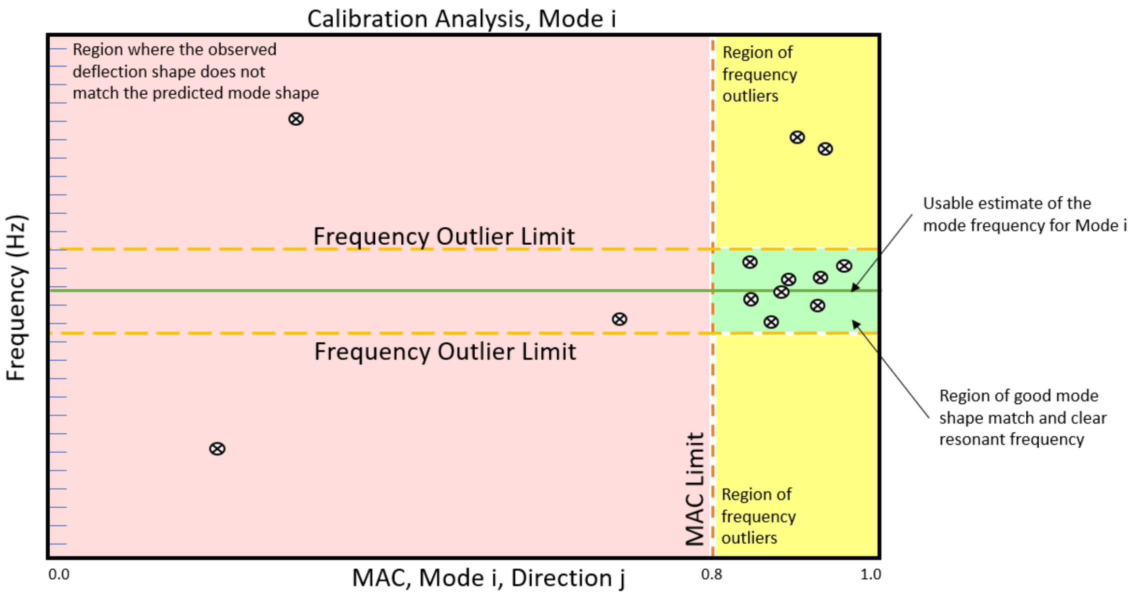

Figure 14: Map of Modal Calibration Data

While descriptive statistics would be convenient to use at this point, there are three independent variables that were adjusted over the course of the hammer tests: the hammer hit location, the cavity used, and the sensor configuration. While the modal behavior of the C100 SRF cavity geometry should theoretically be independent of these variables, they might have an impact in the real world. To study how the modal behavior changed with these independent variables, an ANOVA data analysis technique was used. An example of the modal calibration data map for Cavity Mode 3 in the X direction is provided in Figure 15 noting specifically trends in the cavity selected (differentiated by color) and sensor configuration (differentiated by shape).

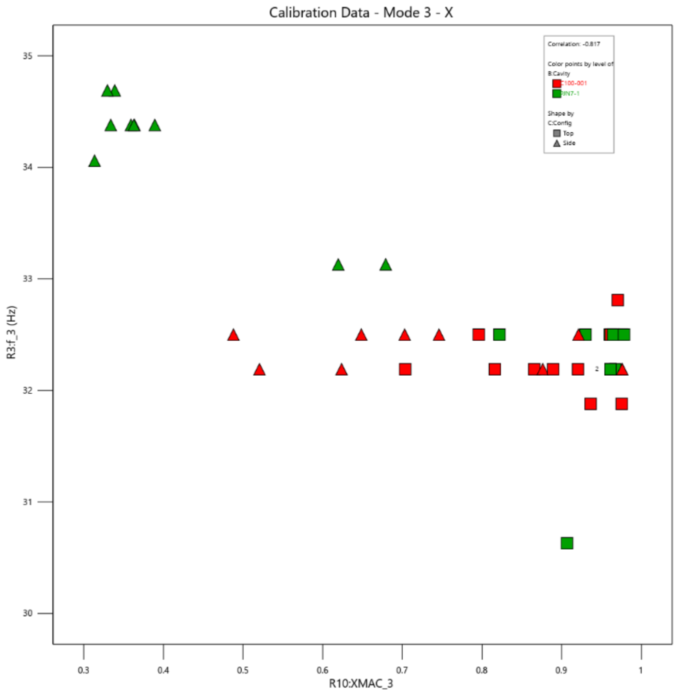

Figure 15: Example of Frequency vs Directional MAC

3.1.3.3 Statistical Methods

As conducted, this experiment lends itself to a factorial type of experiment design. Specifically, there are three factors of interest: hammer strike location (5-level categorical), cavity being tested (2-level categorical), and sensor configuration (2-level categorical). Because two averaged spectra were found per strike point per cavity per sensor configuration, this is a full factorial design with two replicates. A diagram of the experiment design is provided in Figure 16.

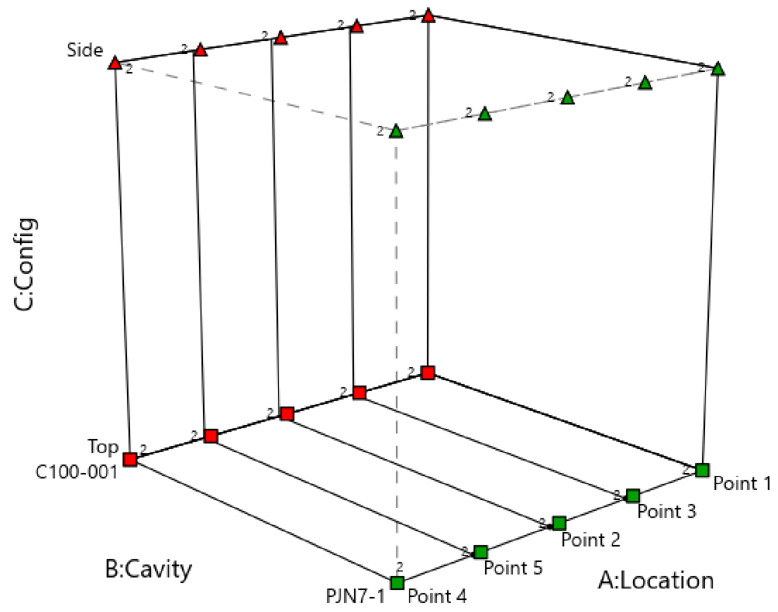

Figure 16: Cavity Hammer Test Experiment Design

As mentioned above, an accurate modal model predicts both the mode frequencies and the mode shapes. The Directional MAC values and the ODS frequencies were the experiment responses in this test (that is, three Directional MAC values and one frequency value per mode, seven modes per replicate, two replicates per design point, twenty design points in total, yielding 28 response variables and 1,120 response values). First-order regression models leveraging ANOVA within Design-Expert® Software [37] were developed based on the modal behavior of both cavities (C100-01 and PJN7-1) after removing all outliers for each of the 28 responses leveraging as many main effects and interactions as possible. A summary of the usability of the models for prediction (R^2_{Pred}), the average properties predicted by those models (mean), and a measure of the spread of the data (standard deviation) is provided for the ODS frequencies, XMAC, YMAC, and ZMAC in Table 3, Table 4, Table 5, and Table 6 respectively. For the regression models which had outliers removed, the significance/insignificance of the Lack of Fit (LoF) is also identified.

Table 3: Statistical Summary of Frequency Regression Models

Mode #	Frequency (Hz)					
	Mean	StdDev	R^2	R^2_{Adj}	R^2_{Pred}	LoF
1	18.36	0.120	0.948	0.929	0.901	Sig
2	25.83	0.671	0.809	0.678	0.456	Sig
3	32.83	0.128	0.988	0.979	0.955	Sig
4	61.36	0.921	0.910	0.889	0.854	Insig
5	70.24	2.739	0.830	0.668	0.320	
6	90.24	0.271	0.996	0.992	0.984	
7	97.42	0.407	0.960	0.922	0.840	

Table 4: Statistical Summary of XMAC Regression Models

Mode #	XMAC					
	Mean	StdDev	R^2	R^2_{Adj}	R^2_{Pred}	LoF
1	0.837	0.020	0.983	0.971	0.944	Insig
2	0.861	0.041	0.950	0.916	0.856	Sig
3	0.746	0.057	0.971	0.944	0.885	
4	0.403	0.064	0.947	0.911	0.851	Sig
5	0.434	0.060	0.939	0.899	0.833	Sig
6	0.621	0.031	0.994	0.988	0.976	
7	0.515	0.023	0.996	0.992	0.987	Sig

Table 5: Statistical Summary of YMAC Regression Models

Mode #	YMAC					
	Mean	StdDev	R^2	R^2_{Adj}	R^2_{Pred}	LoF
1	0.808	0.038	0.896	0.819	0.678	Insig
2	0.789	0.080	0.871	0.747	0.482	
3	0.796	0.028	0.985	0.975	0.957	Sig
4	0.634	0.068	0.875	0.791	0.637	Sig
5	0.687	0.076	0.714	0.520	0.183	Insig
6	0.468	0.042	0.920	0.844	0.680	
7	0.169	0.018	0.988	0.976	0.952	

Table 6: Statistical Summary of ZMAC Regression Models

Mode #	ZMAC					
	Mean	StdDev	R^2	R^2_{Adj}	R^2_{Pred}	LoF
1	0.725	0.051	0.961	0.935	0.883	Sig
2	0.144	0.050	0.950	0.916	0.859	Sig
3	0.801	0.024	0.992	0.985	0.969	
4	0.360	0.032	0.988	0.977	0.952	
5	0.243	0.045	0.940	0.899	0.827	Insig
6	0.712	0.022	0.991	0.982	0.963	
7	0.351	0.037	0.973	0.955	0.923	Sig

While these tables do not indicate the significance of the different effects on the responses, they identify the ranges of ODS frequencies and which ODS shapes were generally well captured. Specifically, all three Directional MAC values for Mode 1 and Mode 3 are relatively high compared to the rest of the sets which demonstrates that these eigenvectors were the most accurately predicted mode shapes from the FEA model. Additionally, the R^2_{Pred} values for these MACs and mode frequencies are higher than the rest, indicating that these regression models are generally usable for explaining the data [36]. Since these predictions are that the average Directional MAC values for these modes will be near or above .8, these results indicate that these mode shapes were reasonably well captured by the FEA model for the purpose of this investigation.

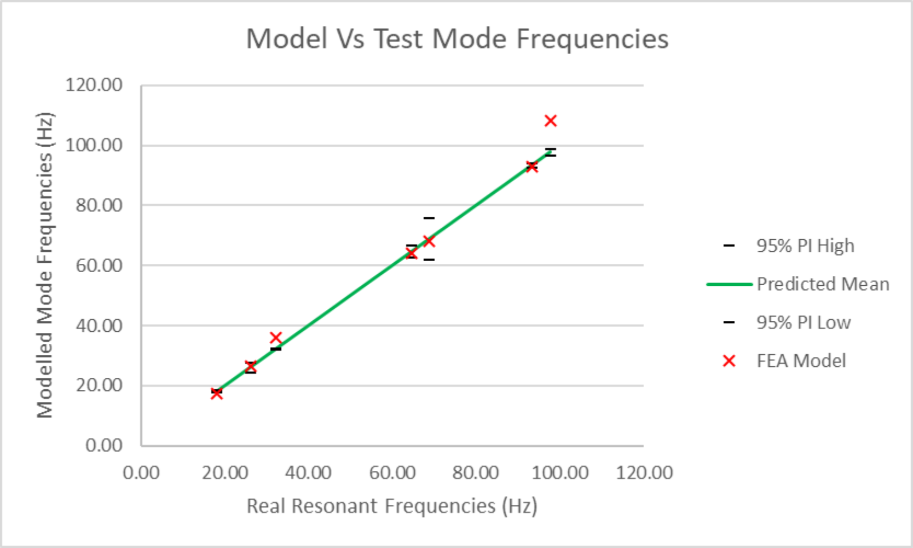

Figure 17: FEA Model vs Prediction Intervals of the Mode Frequencies

With respect to the mode frequencies, the PI is used to estimate the range of acceptable values for each mode frequency in the C100-01 and PJN7-1 cavities. Each PI is summarized in Table 7 and graphed in Figure 17. These values were automatically calculated within Design-Expert® Software [37] for each response. Just as the R^2_{Pred} was sufficient for the mode shapes, Table 7 indicates that the mode frequency estimates for Modes 1 and 3 are also usable for predictions. In these cases, the regression models of the test data predict that these mode frequencies are reasonably close to the predictions made by the FEA model; while the analytical mode frequencies for Modes 1 and 3 are not within the PI, they are still within an acceptable range of error (<4 Hz) to be considered reasonable estimations for the purpose of this modeling effort. Since the mode frequencies and modes shapes were found to be predictably well captured by the FEA model for both modes, the model was considered to be calibrated for the purpose of this investigation.

Table 7: Model vs Test Mode Frequencies

Model vs Test Frequencies							
Mode	95% PI Low	Predicted Mean	95% PI High	FEA Model	Percent Error	R^2_{Adj}	R^2_{Pred}
1	17.90	18.18	18.45	17.367	-4.45%	0.929	0.901
2	24.44	26.09	27.74	26.543	1.73%	0.678	0.456
3	31.84	32.16	32.47	35.838	11.45%	0.979	0.955
4	62.65	64.74	66.83	64.202	-0.83%	0.889	0.854
5	61.75	68.75	75.75	68.075	-0.98%	0.668	0.320
6	92.75	93.44	94.13	93.115	-0.35%	0.992	0.984
7	96.77	97.81	98.85	108.31	10.74%	0.922	0.840

It is worthy to note that there were many outliers in this data. To mitigate their impact, they were removed for each response variable individually so as to increase the R^2_{Pred} values though this process caused the statistical power to vary from response to response and decrease from the ideal power of a full factorial experiment. Outside of general sources of noise in experiments, there were also at least two sources of outliers in both frequency and in Directional MAC value which were caused by the way that the data collection process was done.

After running an uncalibrated but reasonable model of the cavity, the model results were used to inform the search for modes using the MIF_1 and peaks in the hammer test data. While these functions should provide clear indicators of resonance in an ideal world, two deviations from the expectations established in the theory were observed: regions where only one peak was expected had many and regions where one peak was expected had none. Since this selection process was done by hand, the best frequency was chosen based on the information available. An interesting result of this method being used is that if a mode frequency was difficult to identify in one replicate at a design point, it was often equally difficult to find it in the accompanying replicate because the hammer hit location – and therefore the accelerometer response – was the same. Also, the two spectra from a hammer hit point were often close enough that if the selected frequency in one replicate resulted in an outlier, the other replicate often did as well, resulting – quite frequently – in pairs of outliers instead of isolated cases. This was likely due to the fact that the affected modes were not sufficiently excited and the response observed at those frequencies was primarily governed by noise. Unfortunately, this noise made the selection of the frequencies challenging as they were hard to predictably find. As one would expect, this increased the PI and lowered R^2_{Pred} for these responses.

Once the frequencies were selected per the process above, the Directional MAC values were calculated. It is important to note the order of this process because the deflection shape of a vibrational system is predicted to be a combination of mode shapes at frequencies other than the mode frequencies as shown in Equation (2.1.18). As such, errors in frequency could technically also result in errors in ODS shape and thereby lower the Directional MAC values.

With respect to the calculated Directional MAC values, it is important to note how good results are realized noting from Section 2.3.2 that test articles in a hammer test can be excited along specific directions. In an FEA model, some mode shapes inherently have more energy along specific directions, resulting in a similar issue. Practically, this means that good Directional MAC values require that the FEA-predicted mode shape was modeled correctly, the predicted mode shape had clear motion in that direction, and that sufficient energy was deposited in that direction in the hammer test for the mode shape to be realized. Any compromise on these requirements could diminish the Directional MAC value.

With respect to the cavity, the data is still believed to be usable and that it is reasonably represented by the FEA model. That said, it is noted as a learned lesson that the placement of the accelerometers should be such that the experiment can be conducted without adjusting their configuration. Additionally, it is suggested that the hammer hit locations are chosen in oblique angles such that energy is deposited in as many axes as possible. This would have the effect of strengthening the signals captured by the accelerometers, improving the clarity of the data for finding magnitude peaks and MIF_1 dips, increasing the Directional MAC values, possibly removing the outliers, and improving experiment orthogonality.

3.1.4 Summary

The most significant product of this model is a calibrated mesh of the C100 SRF cavity. As a part of this effort, an FEA model of the cavity was developed using provided material properties and geometries. A mesh was developed and tested against a real cavity in a lab environment. The mode shapes and frequencies of the cavity in this configuration were extracted from the test data and were demonstrated to be well captured by the model. It is therefore concluded that this FEA model is calibrated. Because of this, it is reasoned that the behavior of this mesh leveraging application-representative boundary conditions and material properties will be accurate enough for predictions.

3.2 Study 2: Cavity String Model

3.2.1 Model Justification

With the C100 SRF cavity model built, it is necessary to determine what happens to the cavities when incorporated into the cryomodule. This information is desired for many reasons, but especially because it is not yet possible to measure the mechanical deformation of the cavities while the cryomodule is in use. Knowledge of the mode shapes and frequencies which significantly contribute to cavity deformation under these conditions would help identify solutions to cryomodule resonance.

One specific structure within the cryomodule which is believed to be particularly resonant is the cavity string. The cavity string contains the cavities, helium supply and return plumbing, and tuner assemblies. It is suspended by transverse nitronic rods and axial restraints which serve as a system of trusses. It is easy to justify the potential significance of this structure on RF detuning considering that this type of system can be characterized as a massive, flexible beam supported by a truss network of springs and that any cavity string mode shapes would directly deflect the cavities. To characterize its modal behavior, an FEA model was developed leveraging system representative geometry and the C100 SRF cavity model developed earlier.

3.2.2 Model Development

The first part of this model development effort was to simplify the geometry of a full C100 cryomodule such that any assembly desired to be studied can be isolated and studied. To indicate the difference in scale of the task between simplifying a cavity and cryomodule, consider that the cavity model was an assembly of ~10 parts whereas the C100 cryomodule began with more than 22,000 (shown in Figure 18). The approach adopted for this task began with multiple iterations of geometry simplification.

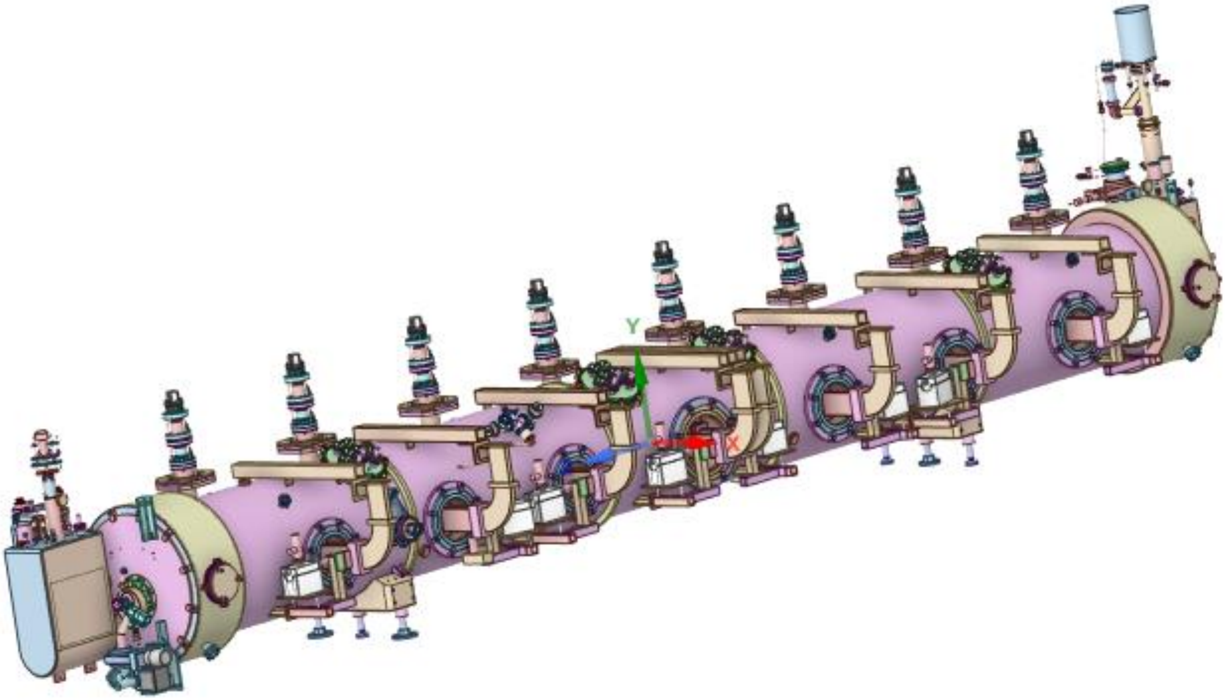

Figure 18: Cryomodule Geometry, ~22,000 Parts (Image used courtesy of ANSYS, Inc.)

The first pass of simplification served to remove trivial parts (nuts, bolts, washers, screws, holes for bolts and screws, chamfers, fillets, wires, etc.) and was responsible for the removal of more than 18,000 parts, leaving ~3,600. A second pass of simplification served to make each remaining part meshable, which involved the further removal of ~600 parts, leaving ~3000 parts. Each of the remaining parts were simplified as much as needed for an efficient mesh without significant compromise on geometric representation: many parts were simplified leveraging shell and beam geometry, dimensions were adjusted such that adjacent parts were in contact, and groups of parts were identified to become condensed geometry for CMS. Figure 19 captures the final product of this effort. With this done, parts of the cryomodule that an analyst wishes to study may be isolated and meshed to their benefit.

Figure 19: Simplified Cryomodule Geometry, ~3,000 Parts (Image used courtesy of ANSYS, Inc.)

In the case of this specific study, it is of interest to determine the modal behavior of the cavity string. To do this, the model was further reduced to only include the cavities, helium vessels, helium supply and return plumbing, tuners, and everything that connects them. This assembly is then suspended within the spaceframe using the 64 nitronic rods, connected to the vacuum vessel through the waveguides and tuners, and integrated with the helium circuit at the end cans. In the interest of model simplicity, it was reasoned that acceptable model results could be obtained by studying the motion of the suspended cavity string alone; this assumption allowed for the argument that the spaceframe and vacuum vessel are relatively immobile. The waveguides, end cans, and the nonvacuum assemblies which drive the tuners were removed as they were outside of the vacuum vessel. Finally, a symmetrical/anti-symmetrical boundary condition was applied at the middle of the cavity string, thereby splitting the model in half. Figure 20 shows what was left.

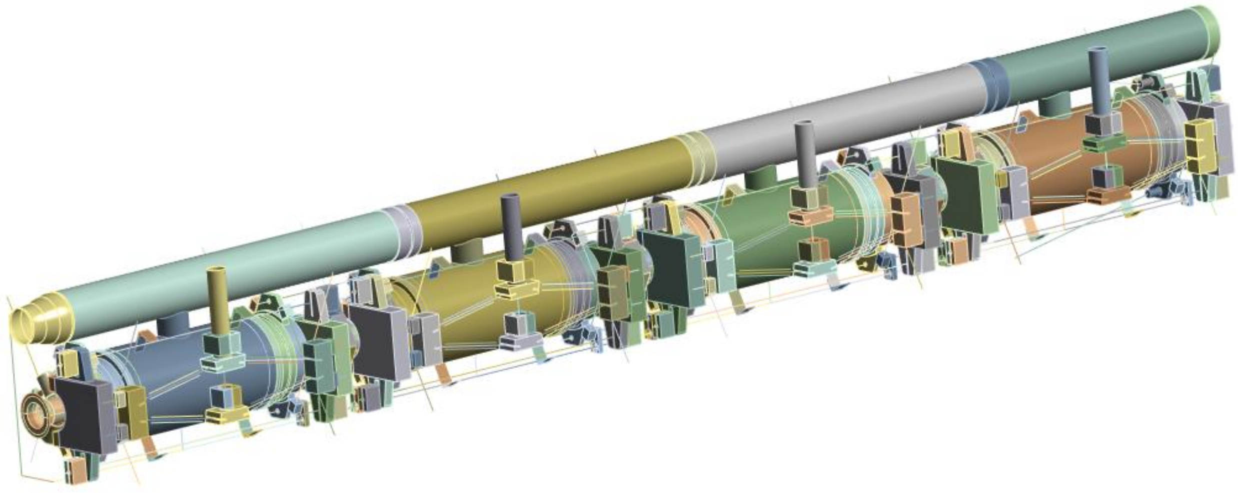

Figure 20: Cavity String Geometry,~902 Parts (Image used courtesy of ANSYS, Inc.)

With the minimum geometry isolated, the mesh was developed (shown in Figure 21). In the end, the model had 1,131,141 nodes; 585,396 elements; and a minimum mesh quality of .051. The act of substructuring the four cavities had the effect of reducing the number of equations in the model by ~20%, but this was found to make motion of the cavities unphysical as the number of modes calibrated and used (seven modes) in the CMS representation was insufficient. Nodes within the mesh were selected to represent the locations of accelerometers that were used during a hammer test. The results of a Static Structural model leveraging the effects of gravity was supplied to a Modal Analysis model within Ansys® Mechanical [35]. The first six modes were computed and the displacement of the accelerometer nodes was used to represent the truncated modes shapes. Note specifically that this model must be run twice to account for both the symmetrical and anti-symmetrical cases.

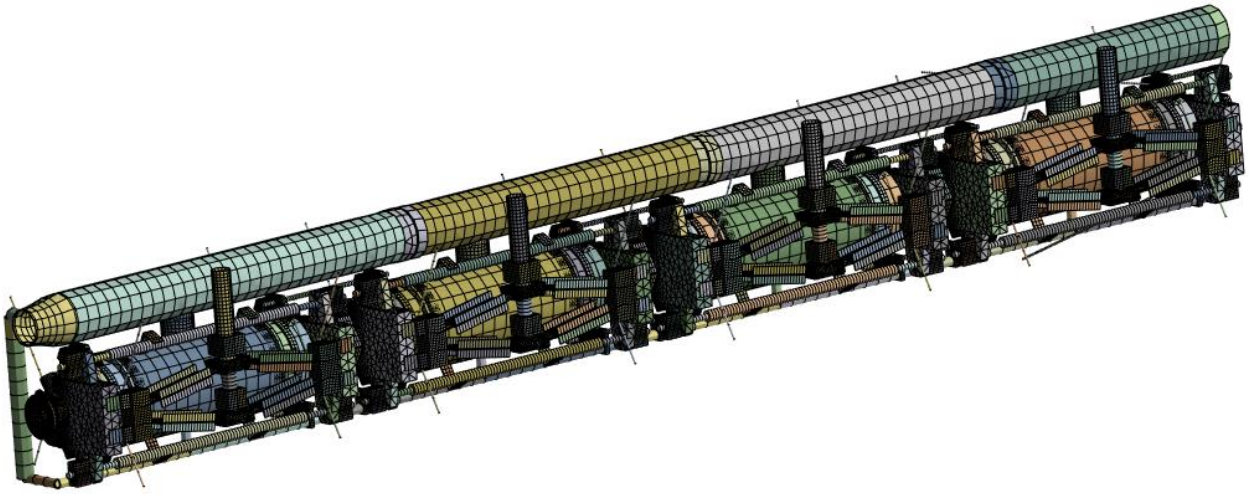

Figure 21: Cavity String Model Mesh (Image used courtesy of ANSYS, Inc.)

3.2.3 Model Calibration

As this is a modal analysis, its calibration follows the exact same method as was performed on the cavities in Section 3.1.3. As before, a representative system (a partially assembled C100 cryomodule, #C100-10R) was affixed with accelerometers in key places and hit with a hammer to excite the modes. The same statistical analysis can be done to indicate the quality of the model leveraging the Directional MAC values and mode frequency distribution.

3.2.3.1 Test Configuration

The C100-10R cryomodule was used as the test article for the calibration of the cavity string model. At the time that this test was done, it contained many of its crucial components: the cavities, helium vessels, tuners, helium supply and return pipes, nitronic rods, spaceframe, and thermal/magnetic shielding. This assembly was supported underneath at points located a quarter of its overall length inwards from either side as shown in Figure 22. Though the tuners were present, they were locked in place as shown in Figure 23 such that the tuners were not free to impact the cavities. In this configuration, the cavity string was able to resonate within the spaceframe under the influence of its own axial and transverse flexibility while primarily retained by the transverse nitronic rods, axial restraints, and tuners.

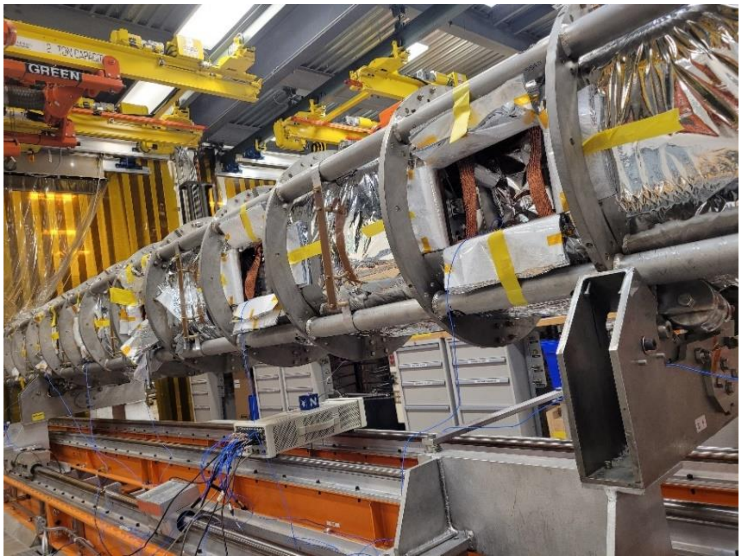

Figure 22: Partially-Assembled C100-10R (Image used Courtesy of Jefferson Lab)

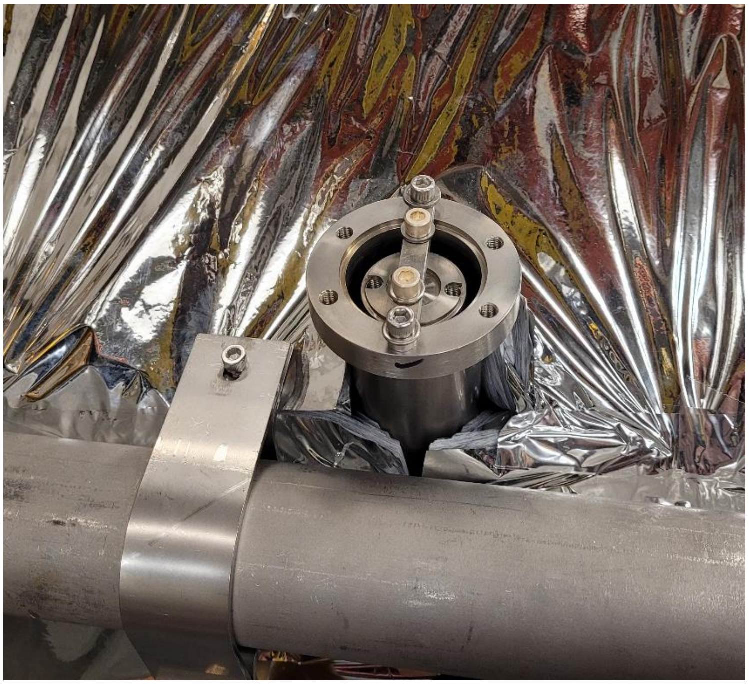

Figure 23: Temporarily-Locked Tuners (Image used Courtesy of Jefferson Lab)

The strategy behind this test was governed by two requirements: to capture the motion of the cavity string as a whole and to capture this information as closely to the cavities as possible. In this way, the modal properties of the cavity string can be identified while the significance of the transfer of mechanical energy from the various hammer hit points to each of the cavities can be estimated. This helps to confirm that energy imparted from those points would contribute to the disturbance of these cavities and cryomodule RF detuning. To achieve this goal, the accelerometers were placed on the outside pivot arm of each cavity tuner specifically just under the beam line as shown in Figure 24. In so doing, the exaggeration of axial motion by the rotation of the pivot arm was kept to a minimum. Also, note that the motion of the pivot arm is primarily used to stretch and compress the cavities. The selected location for the accelerometers captures this motion and provides insight into how much the cavities themselves can become mechanically excited.

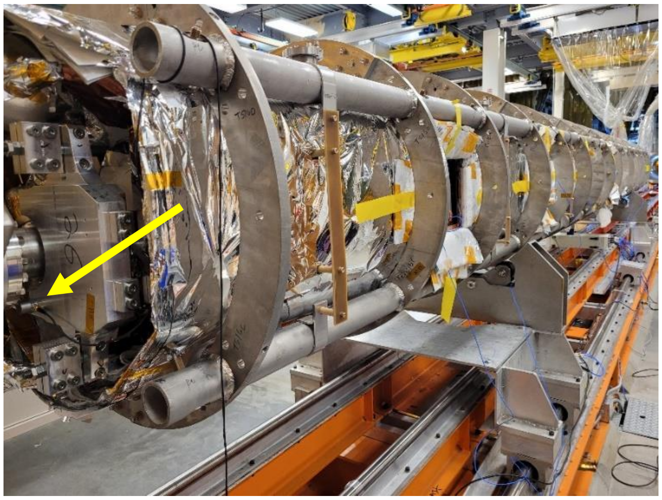

Figure 24: Accelerometer on a Tuner Pivot Arm (Image used Courtesy of Jefferson Lab)

A total of 16 hammer hit points were selected on the cryomodule to effectively excite the cryomodule in each test as shown in Figure 26. As with the cavity hammer tests, a set of 10 hammer hits were averaged to generate one averaged spectrum, two such averaged spectra were collected for each of the 16 points. Seven 3-axis accelerometers and two 1-axis accelerometers were used yielding 23 channels of responses and 736 spectra to review. The configuration of these sensors is shown in Figure 25, noting that +Z points to the Return End Can side.

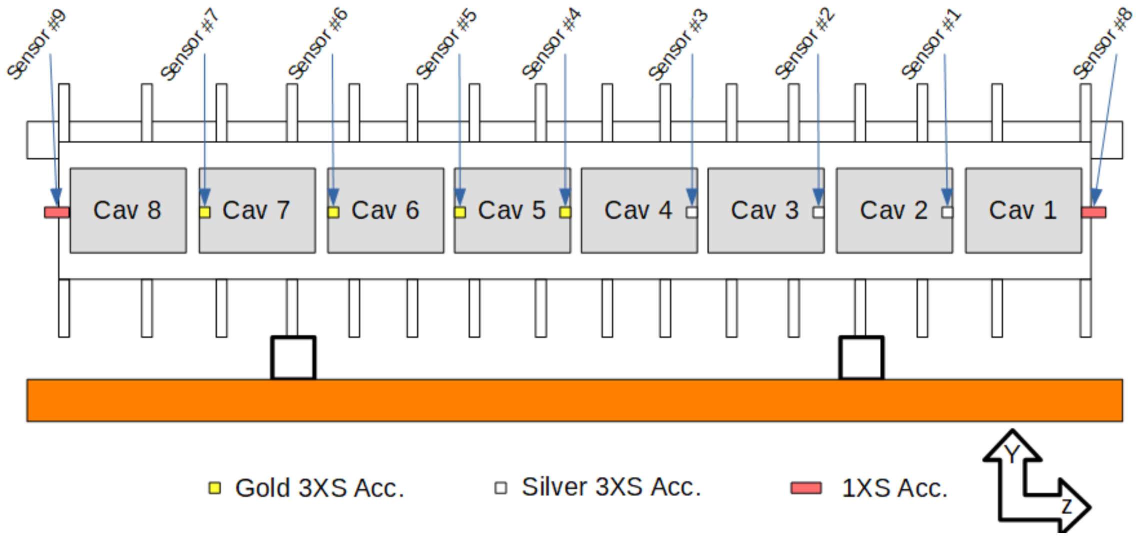

Figure 25: Accelerometer Locations

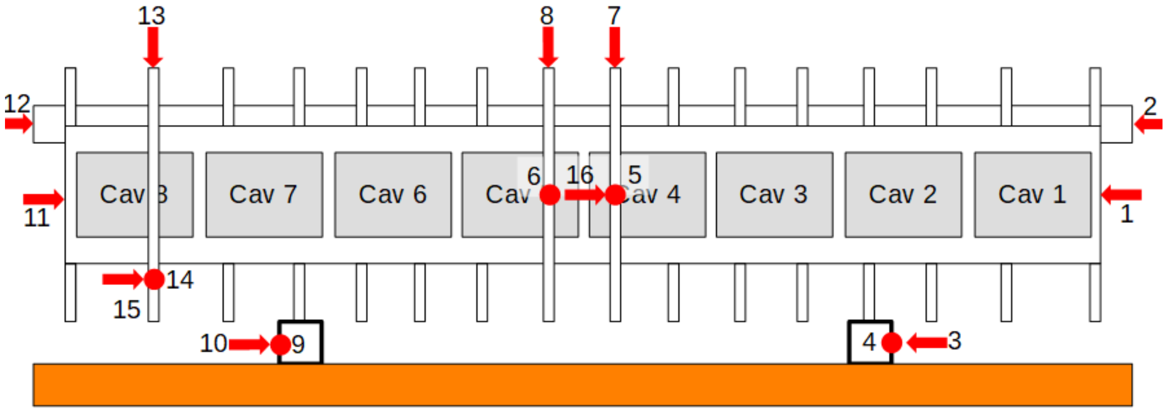

Figure 26: Hammer Hit Locations

3.2.3.2 Data Analysis

As done with the cavity during Section 3.1.3, the modal behavior of the cavity string must be determined from the hammer test data. The same method leveraging the Normal MIF (MIF_1) as described in Section 2.2.1 was used to identify mode frequencies. The clearest indicators of modes were found in the X direction when excited with Points 5 and 6 (Figure 27) at 7 Hz and 23 Hz; the Y direction when excited with Points 7 and 8 (Figure 28) 7.5 Hz, 11 Hz, and 23.5 Hz; and the Z direction when excited with Point 2 (Figure 29) at 13.13 Hz and 28.75 Hz. The ODS shapes were extracted at these frequencies. Due to the number and size of the figures showing the ODS shapes, they are presented in the Appendix, Section A.

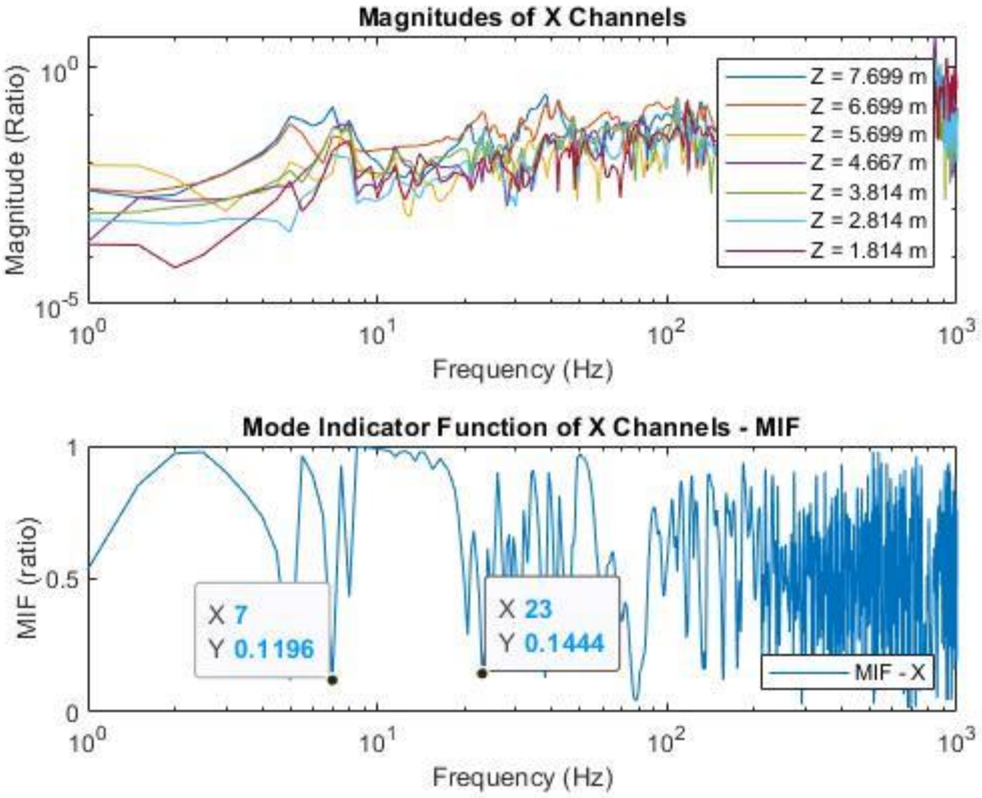

Figure 27: Magnitude and MIF_1 from Horizontal Bending Hits

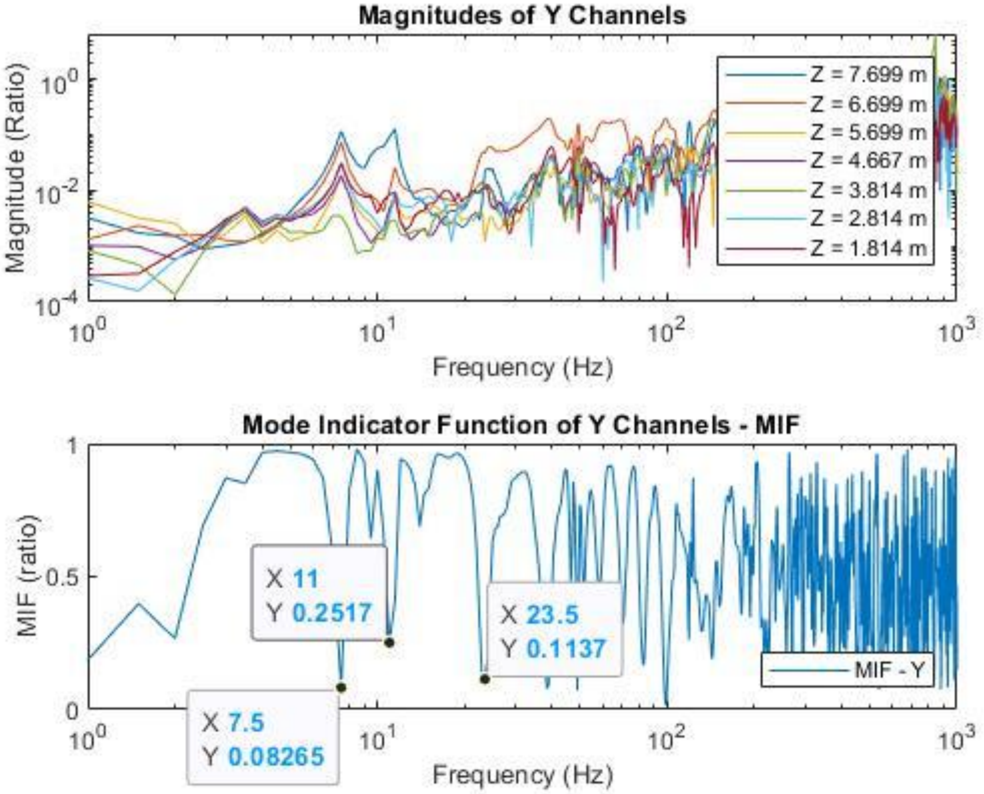

Figure 28: Magnitude and MIF_1 from Vertical Bending Hits

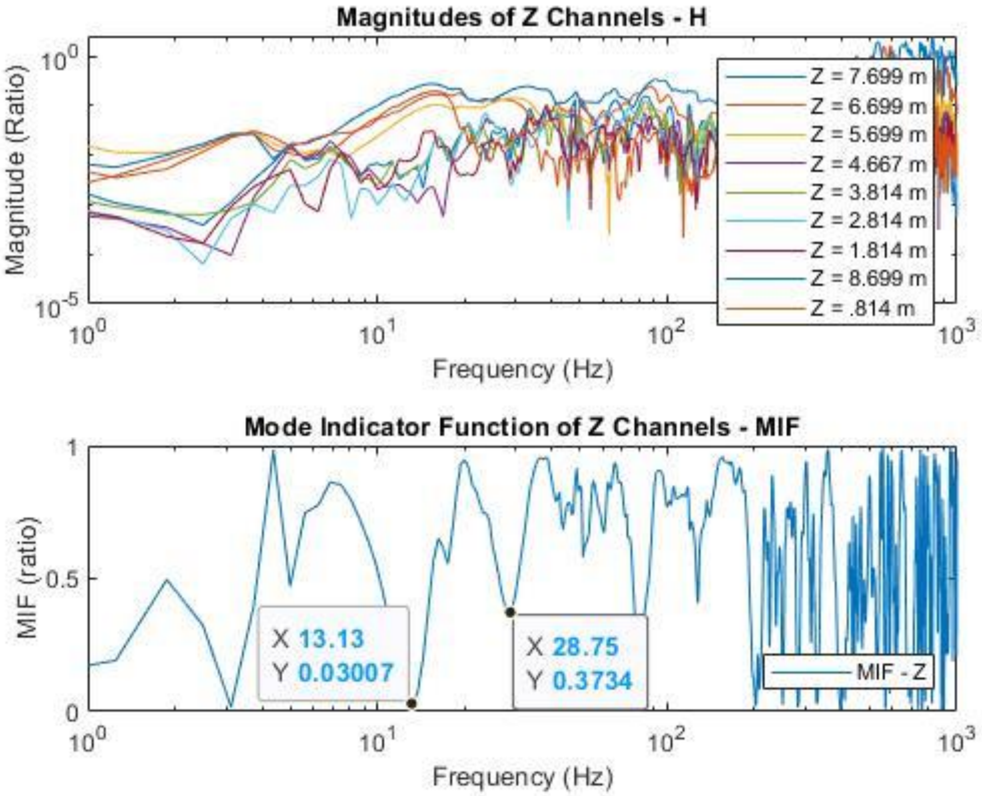

Figure 29: Magnitude and MIF_1 from Axial Hits

3.2.3.3 Model Results

Unfortunately, the cavity string model was not found to accurately represent the test data. The predicted mode frequencies are far too high to represent the modes identified in the associated hammer test. For example, Figure 30 shows that the first axial mode is predicted to occur at 27 Hz, though a similar mode shape was found in the test data to occur at 13 Hz. To help identify why these mode frequencies were so high, the nitronic rods were replaced with a similar representation leveraging springs, the results were roughly similar. Decreasing the spring rate of the nitronic rods by some 50% was needed to get one horizontal mode close to the right frequency range, but this adjustment is not reasonable and the model output is not usable. This indicates that the nitronic rods are not the source of error and that the problem likely lies in the cavity string itself. FEA modal models make predictions generally based on stiffness and mass, both of which are governed in different ways by geometry, material properties, and mesh composition. It is possible that adjusting the parameters within the existing model will resolve this problem; it is also possible that other assemblies (the space frame, magnetic shield, etc.) and their contribution to mass and stiffness will have to be added to achieve reasonable results.

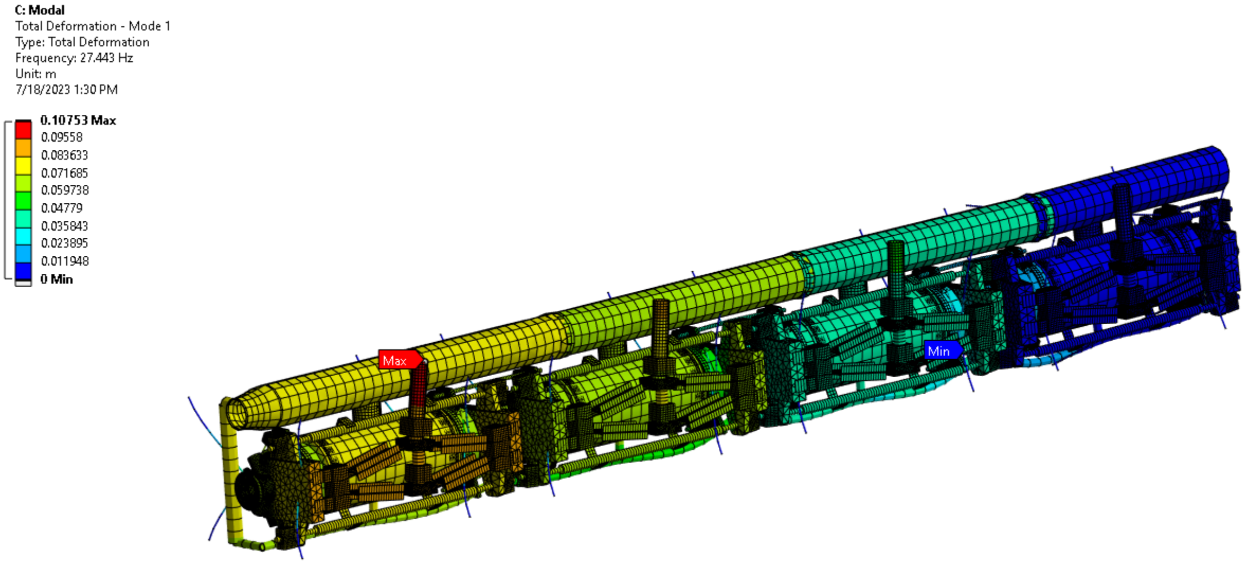

Figure 30: Mode 1 of the Cavity String Model, 27 Hz (Image used courtesy of ANSYS, Inc.)

In an effort to characterize the effects of material properties, the definition of 316L stainless steel – which was used to model most of the structural elements in the cavity string – was manipulated to have a 75% increase in density and 43% decrease in Young's modulus. Even though these changes are unreasonably large, the model did not provide the desired results. Considering this evidence, it is concluded that the issue lies somewhere between the geometry and the mesh used to represent the cavity string and it is recommended that further work be done to develop them more carefully.

Even though the results need improvement, this model does have potential to become a modal model of the cavity string. While the mode frequencies were not correct, the mode shapes are somewhat representative of what is seen in the test data. Even though the model is large, it was able to run in a reasonable amount of time (~30 minutes) and consume a reasonable amount of hard disk space (<70 GB) on a suitably strong computer. Additionally, the model itself leverages system-representative geometry, which – if calibrated correctly – could be used to study the effects of prototype solutions before they are tested in a lab environment.

3.2.4 Summary

While it was desired to develop an FEA model of the cavity string leveraging system-representative geometry, the model developed was not found to be accurate. Even so, it is still possible to accomplish the objective of this effort: the resonance behavior of the cavity string was captured in the hammer test data. While hammer testing does not necessarily provide a perfect picture of the modal behavior of the test article, the hammer tests performed on the partially-assembled cryomodule does strongly indicate several modes when excited in the principal directions. The ODS shapes have been extracted at those resonant frequencies. This combination of ODS shape and frequency can be used in this investigation to describe the resonance behavior of the cavity string.

3.3 Study 3: CMTF Test of the C100-10R Cryomodule

3.3.1 Test Justification

The purpose of this test was to correlate mechanical resonance in the C100-10R cryomodule to RF detuning of the cavities while in use. The theory of vibrations described in Section 2.1 indicates that vibrational systems will experience vibration modes at specific frequencies, resulting in resonance. If some phenomenon is related to the resonance of a system, it is expected that it can be observed as the system experiences resonance – that is, unforced vibration initiated by a mechanical disturbance. While it is not possible to measure the actual modal behavior of the cryomodule being tested, the vibration modes of critical systems within the cryomodule have been estimated with the hammer test in Section 3.2.3 leveraging the partially assembled cryomodule. Evidence that mechanical resonances contribute to RF detuning should therefore be said to be found if peaks in the RF detuning spectrum are found to be coincident with the identified vibration modes.

There is another side to this experiment: BNNT, LLC has developed a set of canisters which have been designed to be a solution to microphonic disturbances. These canisters are similar in form and function as automotive dampers in that friction is used to dissipate kinetic energy into heat. Unlike other dampers, these canisters have samples of Boron Nitride Nanotubes (BNNT) which serve as the material which causes the necessary friction for damping. It was desired to assess the effectiveness of these devices while the system is in use; such an assessment was easily incorporated into the this test as a study into how these devices affect RF detuning in the cryomodule. The configuration of the canisters in the C100-10R cryomodule is shown in Figure 31 with the canisters highlighted with the red boxes.

Figure 31: BNNT Canisters in the Cavity String (Image used Courtesy of Jefferson Lab)

As mentioned before, an appropriate test for resonance is a hammer test, but the RF detuning – not acceleration – is to be collected in response to the hammer hits. For this test to accurately represent the conditions of the cryomodule while it is in use, liquid helium and high-power RF must be supplied. The helium is critical in that it drives the temperature of the cavities which changes their material properties and modal behavior. The high-power RF is an application-representative signal that is detuned by the cavities. As the detuning of this signal is the measured output, this experiment will provide a picture of similar effects during real-world use.

3.3.2 Experiment Design

A test of this arrangement was performed at the Jefferson Lab Cryomodule Test Facility (CMTF) between January 31 and February 1, 2023. The CMTF is an environment which allows a cryomodule to be tested as if it were a part of a particle accelerator without an electron beam present. Specifically, a cryomodule can be bolted to the floor, provided cryogenic helium, and fed high-power RF. Additionally, the RF performance of the cryomodule can be captured using a set of installed RF sensors and an automatically actuated hammer is available for the performance of hammer tests in a potentially radioactive environment. In short, this is an ideal facility to conduct this test.

To perform the hammer test, the automatic hammer was configured as shown in Figure 32. The hammer was used to impact the beam line on the Helium Return side and excite the cavity string. Additionally, a set of eight enDAQ S3-D16 accelerometers were arranged at critical points along the cryomodule shown in orange in Figure 33. These devices did not have integrated timing with the hammer; instead, these sensors were used to capture ambient noise at those points.

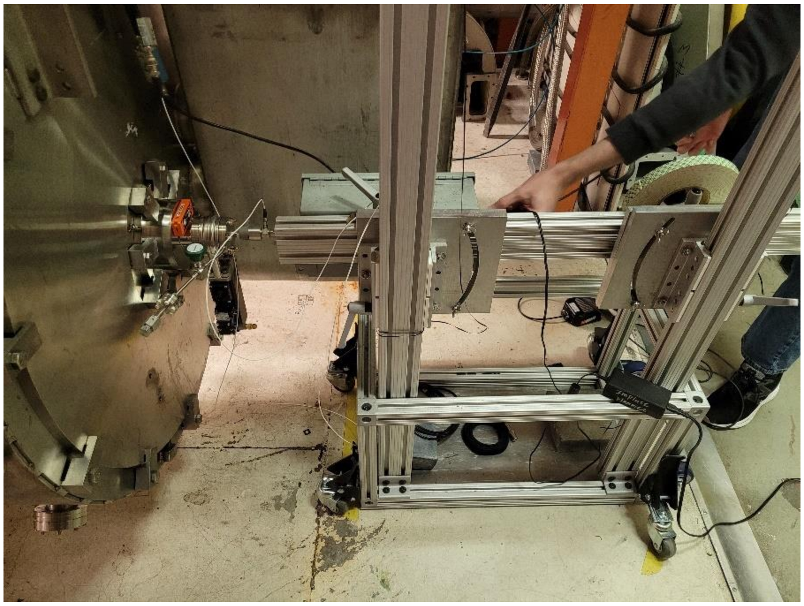

Figure 32: CMTF Hammer Configuration (Image used Courtesy of Jefferson Lab)

This test collected two types of information on RF detuning: ambient noise and dynamic response. Ambient noise was collected by simply recording the RF signals for a period of 30 seconds. The dynamic response was collected in a similar form to that described in Section 2.3 except that the response term $A_i(f)$ in Equation (2.3.1) is replaced with the RF frequency shift Δf_{RF} of a particular cavity which is used to quantify the degree to which it is detuned. The response function analogous to Equation (2.3.1) as applied here becomes:

$$H_i(f) = \frac{\Delta f_{RF,i}(f)}{F(f)} \frac{[Hz]}{[lbF]} \tag{3.3.1}$$

By studying the changes in this function when varying the resonance properties of the cavity and cryomodule, the effects of those changes on RF detuning can be quantified.

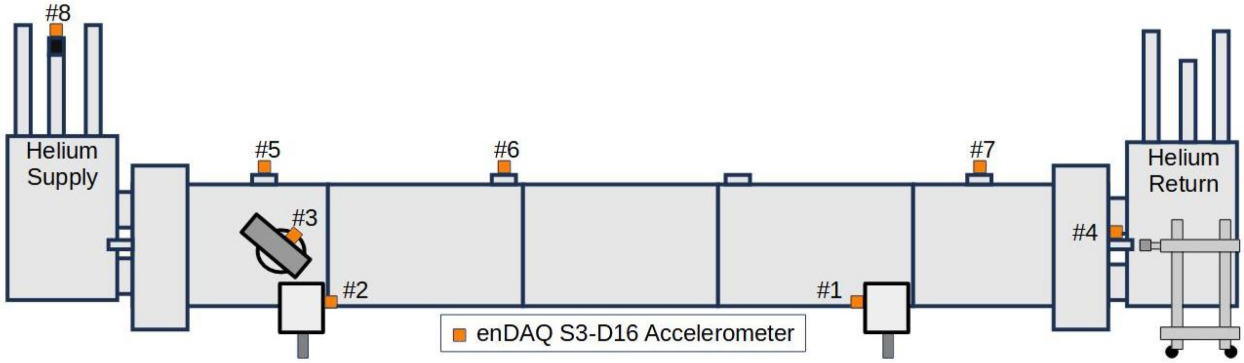

Figure 33: Locations of Accelerometers and Hammer

3.3.3 Data Analysis Methods

The values of Δf_{RF} were automatically calculated by the data acquisition system and was measured in each cavity one at a time. This data was reported in the form of a frequency response function $\left(\frac{\Delta f_{RF}}{F}\right)_{(f)}$ in which the spectrum of Δf_{RF} was normalized by the spectrum of the hammer hit forces. Given this, the spectrum of $\left(\frac{\Delta f_{RF}}{F}\right)_{(f)}$ provides an effects-based perspective of resonance based on direct measurements of RF detuning and impact forces. Evidence of resonance contributing to RF detuning can be said to be found if peaks in this spectrum coincide with the mode frequencies from the FEA model under cryogenic conditions and/or the hammer test data used to calibrate this model.

To assess the effect of the BNNT canisters on RF detuning, it is necessary to perform these resonance tests with and without them present. While it is not feasible to fully remove them, it is possible to engage and disengage the canisters using the cavity tuners. The tuners on the cryomodule are driven by motors and serve to compress or stretch the cavities. One benefit of this configuration is that the tuners can compress the helium vessel around the cavities to the extent that the BNNT canisters become disengaged. By performing identical tests on the cryomodule under the engaged and disengaged configurations, the differences in the detuning response spectra can be studied and the effects of the canisters can be determined.

To find the differences between two spectra, one can simply subtract one spectrum from another. In this case, the difference spectra between any two sets of data collected on a cavity was found to be rather noisy. To help smooth the spectra such that trends could be observed, the difference in the spectra of RF detuning was integrated in a similar fashion as done with the Power Spectral Density:

$$I(f) = \int_0^{\log_{10}\left(\frac{f}{1\,Hz}\right)} \left[\left(\frac{\Delta f_{RF}}{F}\right)_{(f)_{ENG}} - \left(\frac{\Delta f_{RF}}{F}\right)_{(f)_{DISENG}}\right] d\left(\log_{10}\left(\frac{f}{1\,Hz}\right)\right) \frac{[Hz\ RF]}{[lbF]} \qquad (3.3.2)$$

In the case of a random noise test where the applied forces are not measured:

$$I(f) = \int_0^{\log_{10}\left(\frac{f}{1\,Hz}\right)} \left[(\Delta f_{RF})_{(f)_{ENG}} - (\Delta f_{RF})_{(f)_{DISENG}}\right] d\left(\log_{10}\left(\frac{f}{1\,Hz}\right)\right) [Hz\ RF] \qquad (3.3.3)$$

3.3.4 Preliminary Results

An example of the RF detuning spectra of a C100 cavity (C100-10R, Cavity 6) from a hammer test is shown in Figure 34. In this graph, the red line represents the RF detuning of the cavity when the canisters are disengaged and the blue line represents the same but with the canisters engaged.

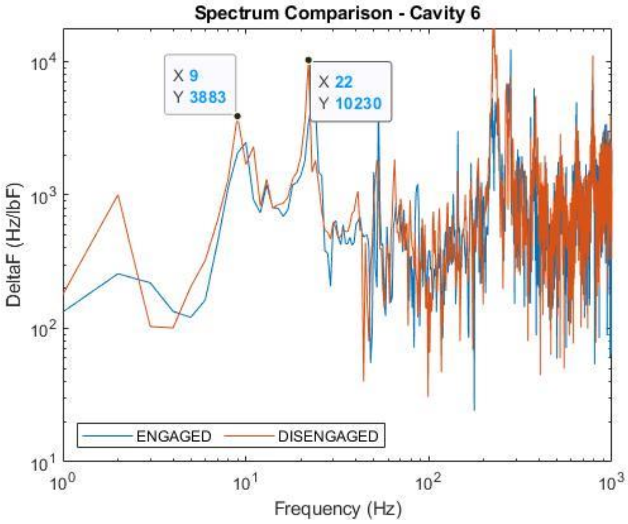

Figure 34: Comparison of RF Detuning Spectra from Hammer Hits

It is worthy of note that the two identified peaks are consistently observed in all detuning spectra in for all cavities. It is also observed that the frequencies change slightly between when the BNNT canisters are engaged and disengaged. The average and standard deviation of the peak frequencies are presented in Table 8.

Table 8: Summary of Peak Frequency Locations

	Lower, Engaged	Lower, Disengaged	Upper, Engaged	Upper, Disengaged
Average (Hz)	10.0	9.6	23.7	22.6
Standard Deviation (Hz)	0.2	0.5	0.4	0.5

One trend that can be studied to see if the canisters had a positive effect on RF detuning would be the decrease in magnitude of RF detuning between the two spectra. This would be realized in the form of a generally negative difference spectrum found by subtracting the disengaged spectrum from the engaged spectrum. In this example, this ‘difference spectrum’ is presented as the blue line in Figure 35. Integrating this difference spectrum with Equation (3.3.2) would transform these negative values into negative slopes; improvements in RF detuning would therefore be found if this integral function generally trends downward. Improvement in RF detuning across a feature in the spectrum can be found if the integral function across the frequency range of the feature decreases. The ‘integral spectrum’ in this example is shown as the red line in Figure 35. The integral functions for all cavities studied is presented in Figure 36.

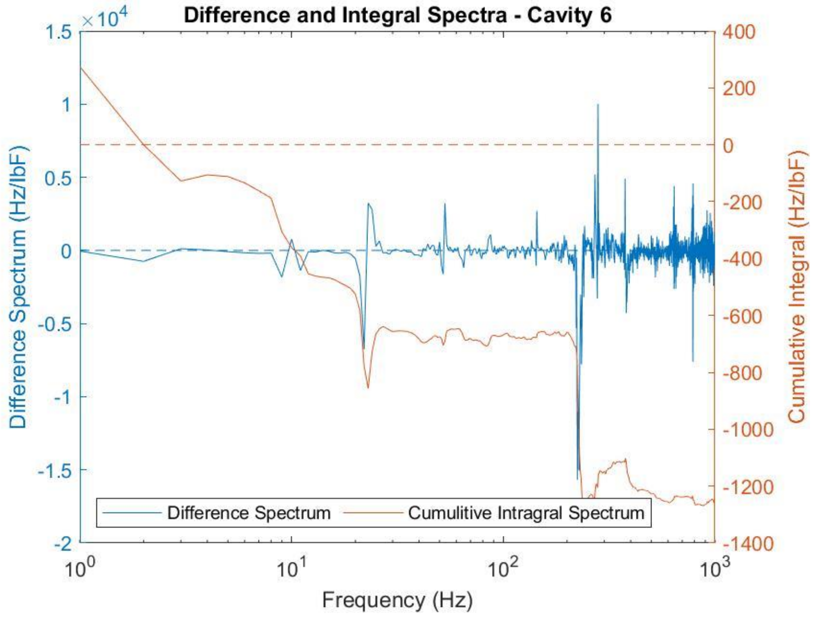

Figure 35: Difference and Integral Spectra from Hammer Hits

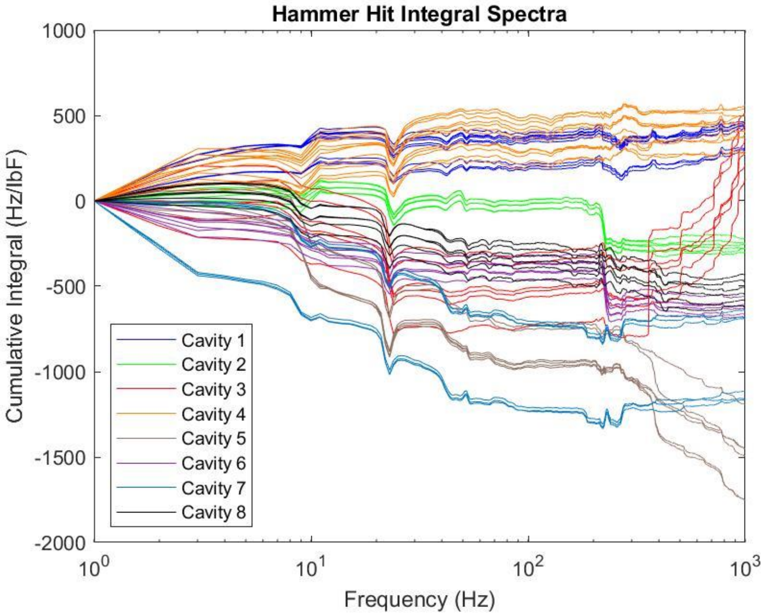

Figure 36: All Integral Spectra from Hammer Testing

These methods can also be applied to the ambient noise data, noting that ambient factors (all manner of disturbance inside and outside of the cryomodule, possibly including electromagnetic sources) are the sources of disturbances, not measurable hammer hit forces. Because of this, the spectra presented in this graph are not in any way normalized. This data instead represents the response of a real system to its environment. An example of the noise spectra (C100-10R, Cavity 6) with and without the canisters engaged is presented in Figure 37. The associated difference and integral spectra are presented in Figure 38. All integral spectra tested are presented in Figure 39.

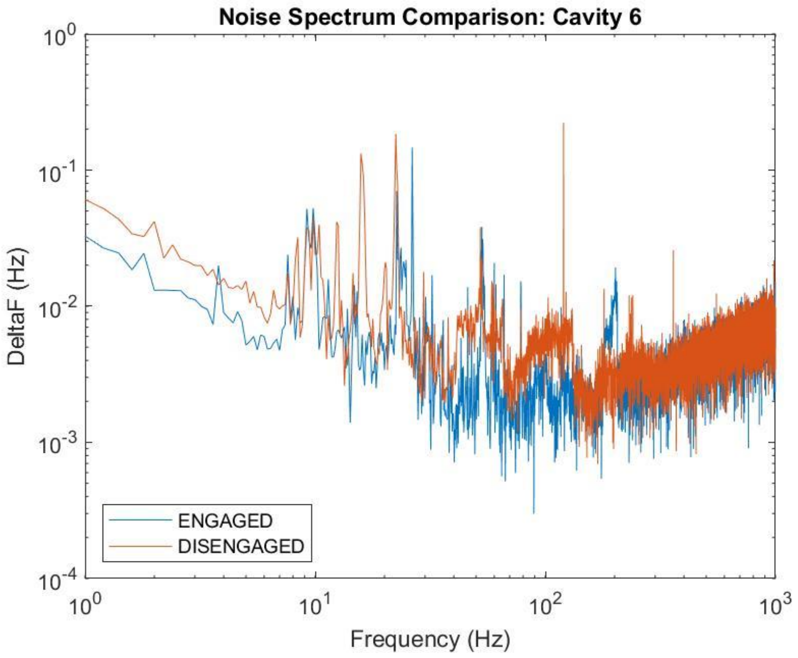

Figure 37: Comparison of RF Detuning Spectra from Noise

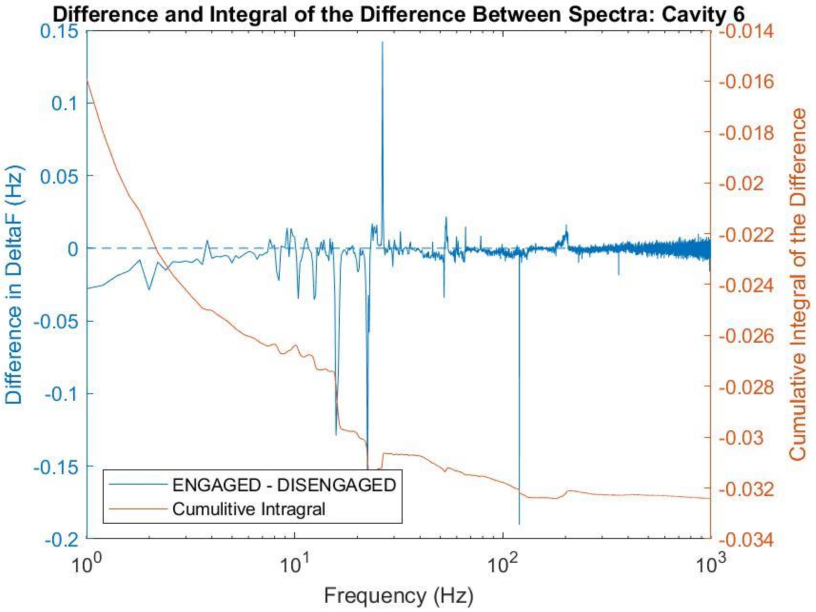

Figure 38: Difference and Integral Spectra from Noise

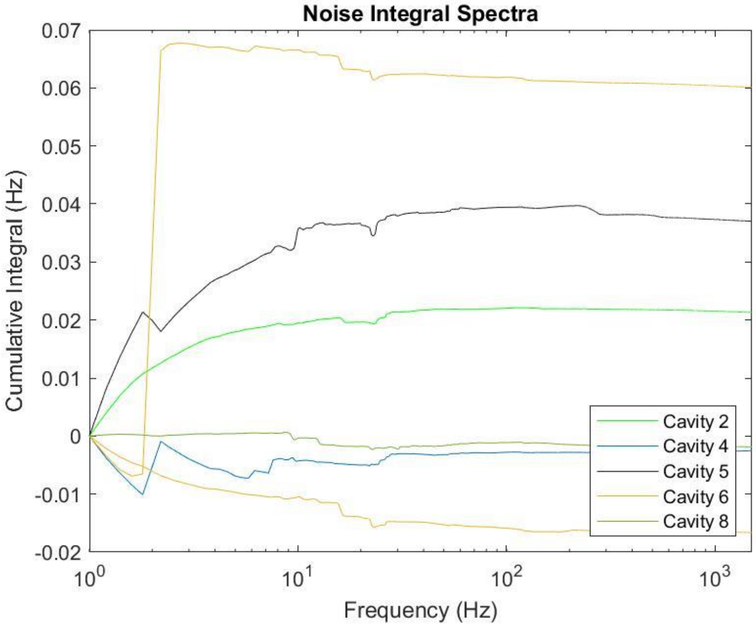

Figure 39: Integral Spectra from Noise for all Cavities Tested

It is of critical importance to consider the presence of lurking variables when drawing conclusions from this data. Due to the order of events, hammer tests and noise recordings with the BNNT canisters engaged were performed on January 31, 2023, and the same tests were done with the canisters disengaged on February 1, 2023. Because of this, the main effect (the engagement of the canisters) is perfectly aliased with the day that the data was collected. As such, it is possible that the variations observed could also be the result of variables that change day-by-day: the weather, the ground vibration profile, helium levels in the cryomodule, etc. An example of how the environment changed can be seen in Figure 40. These figures represent the averaged spectrum of acceleration captured by enDAQ accelerometer #5 during the two days of testing. One can clearly see that the noise floor at this point changed between these two days, indicating that lurking variables were likely present. A fully randomized run order would mitigate these issues.

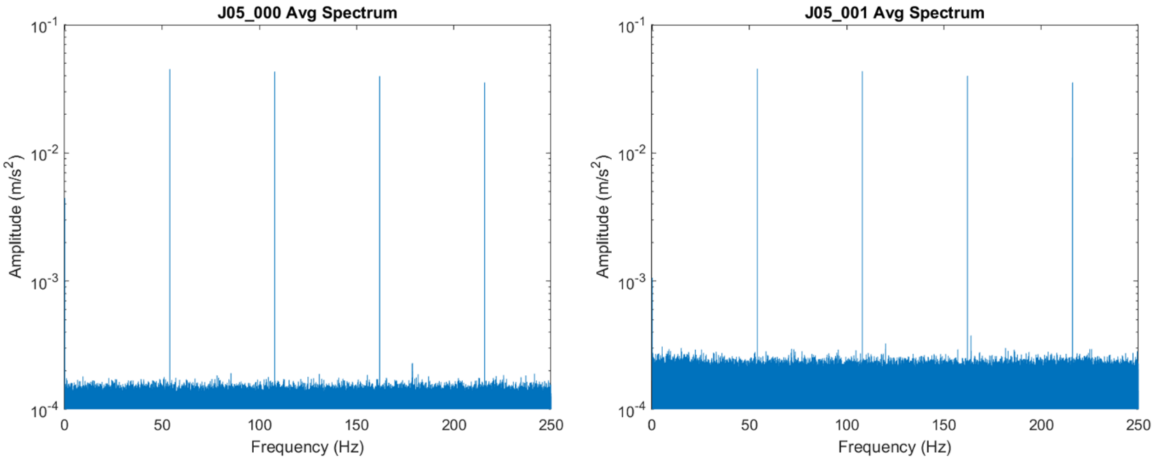

Figure 40: Noise Captured by Accelerometer #5 on January 31 (Left) and February 1 (Right)

It is also worthy of note that the method used to disengage the canisters technically also introduces other sources of variation. For example, tension and compression is known to influence the mechanical resonance properties of structures; the tuners were used to compress the cavity in order to disengage the canisters, which might have resulted in a shift in cavity modal behavior and/or its mechanical/RF coupling properties. Additionally, it is possible that the tuner mechanism – being in a non-nominal configuration – was also affected in its ability to maintain low RF detuning. It is therefore possible that the method used to disengage the BNNT canisters played a role in how each cavity brought about the measured RF detuning spectra.

Finally, it is worth noting that the hammer was placed on one location in this hammer test which likely deposited more energy on some cavities than others. Because of this, some canisters might have been more effectively tested than others. Table 9 provides a summary of the hammer test and noise test by interpreting the overall trends in the integral function. Table 10 provides a summary of the results of the hammer test by interpreting the trends in the integral function around the 9 Hz and 22 Hz peaks.

Table 9: Interpretation of General Trends

Cavity	**Hammer Test**	**Noise**
Cavity 1	Degraded	N/A
Cavity 2	Neutral	Degraded
Cavity 3	Improved	N/A
Cavity 4	Degraded	Neutral
Cavity 5	Improved	Degraded
Cavity 6	Improved	Improved
Cavity 7	Improved	N/A
Cavity 8	Improved	Neutral

Table 10: Interpretation of Features in the Hammer Test Responses

Cavity	**9 Hz**	**22 Hz**
Cavity 1	Degraded	Improved
Cavity 2	Degraded	Improved
Cavity 3	Improved	Improved
Cavity 4	Degraded	Degraded
Cavity 5	Improved	Improved
Cavity 6	Improved	Improved
Cavity 7	Improved	Improved
Cavity 8	Improved	Improved

CHAPTER 4

RESULTS AND DISCUSSION

4.1 Mechanical Resonance and RF Detuning

As a part of this study, it must first be established if resonance in the cryomodule contributes to RF detuning. To do this, a correlation between modal behavior and RF detuning must be observed. Hammer tests – which are appropriate tests for resonance – were performed on the C100-10R cryomodule while it was partially assembled and while it was installed in the CMTF once it was completed. The former test yielded strong indicators of several mechanical modes in the cavity string; the latter test yielded strong indicators of consistent RF detuning peaks in the cavity responses. While it was desired to use an FEA model to provide further evidence of the modal behavior of the cavity string when the cryomodule was completed and cryogenically cooled, the model built was not found to be accurate.

To show a correlation between RF detuning and mechanical resonance, the RF detuning peaks observed must be coincident in frequency with the mechanical modes. For the sake of completeness, consider the cases where frequency coincidence is not observed. In the case where an identified mode frequency is not coincident with a peak in RF detuning, it could be that:

- The applied forces from the hammer in the CMTF RF detuning hammer test were small at that mechanical mode frequency,

- The applied forces did not effectively excite the cavity string mode,
- The disturbed cavity string did not effectively disturb the cavities at that mechanical mode frequency, or
- The disturbed cavities did not effectively cause RF detuning in that mechanical mode.

In the case where a peak in RF detuning occurs where a mode is not predicted, it could be that:

- The forces from the hammer in the RF detuning hammer test overcame the cavity string non-resonance, the cavity string effectively disturbed the cavities, and the cavities were sensitive to RF detuning at that peak frequency,
- Resonance was excited, but not in the cavity string, or
- The RF detuning observed in the CMTF hammer test was brought about by other means.

However, if frequency coincidence is observed and the mechanical mode was excited effectively, a correlation between the cavity string modal behavior and RF detuning can be argued.

As shown in Section 3.3.4, the two peaks in the detuning spectrum in Figure 34 were found to be consistent features in the detuning spectra of all cavities. To correlate RF detuning to mechanical resonance, modes in the cavity string would need to be shown to be coincident in frequency with 9-10 Hz and 22-23 Hz. It is important to note that the completion of the cryomodule and the cryogenic cooling of the cavity string changed its modal behavior between the cavity string hammer test and the CMTF RF detuning hammer test. In general, cooling has the effect of making components stiffer which raises mode frequencies. While this frequency increase was not estimated or measured as a part of this thesis, it is noted that the observed mode frequencies likely changed from where they were originally observed in the hammer test.

Considering this, it is noted that the 7 Hz and 23 Hz horizontal mechanical modes and 7.5 Hz and 23.5 Hz vertical mechanical modes are close to the observed RF detuning peak frequencies. Knowing that the mechanical modes likely shifted in frequency, it is reasonable to believe that the mechanical modes shifted to the observed RF detuning peak frequencies at 9-10 Hz and 22-23 Hz. It could therefore be argued that these four instances of cavity string resonance correlate to RF detuning. However, the lack of sure frequency shift estimation makes it impossible to confirm the exact changes that occurred in these four modes or to completely discount the significance of any others. More in-depth research will need to be done to know for certain.

4.2 BNNT Canister Effectiveness

With respect to the BNNT canisters, Figure 36 shows that five out of the eight cavities were improved by the engagement of the canisters during the CMTF hammer test. While those five integral functions follow negative slopes overall, Cavity 1 and Cavity 4 show positive slopes and Cavity 2 holds a level slope. With respect to the specific RF detuning peaks, Table 10 shows that the trends around the RF peak frequencies show improvement at the 9-10 Hz peak in five out of the eight cavities and at the 22-23 Hz peak in seven out of eight cavities. This indicates that the canisters were sometimes – though not always – effective against these mechanical resonances. These are promising results that the BNNT canisters could be used for this application.

With respect to random noise, the overall trends in Figure 39 appear to show that one cavity was improved, two were not affected, and two were degraded by the engagement of the canisters during this test. However, lurking variables in these two experiments – especially the aliasing of the main effect with the day, any effect brought about from changes in cavity/tuner dynamics caused by canister disengagement, etc. – renders this test somewhat inconclusive. To increase the certainty in this test, it is recommended to repeat this experiment leveraging a randomized run order in order to remove the aliasing from the environment.

CHAPTER 5

CONCLUSION AND FUTURE WORK

5.1 Conclusion

Resonance is a type of structural behavior in which the application of a small excitation at a specific frequency produces significant motion. Prior research has been done which indicates that external mechanical disturbances – called microphonics – can cause RF detuning of the SRF cavities in cryomodules. Resonance is therefore important to the study of microphonics as it characterizes how external disturbances can most effectively result in cavity motion, leading to RF detuning. It is the purpose of this thesis to correlate mechanical resonance behavior in a C100 cryomodule with the RF detuning of its cavities leveraging FEA.

Modal analysis through finite element modeling was chosen to study the resonance of the C100 cavity and cavity string. FEA techniques were used to ensure that the models of the cavity and cavity string were small enough to run yet accurate enough to use. Hammer testing was used to experimentally determine the modal behavior of the cavity and cavity string using real systems. A statistical method leveraging the Design of Experiments was developed to validate the FEA models leveraging the hammer test data collected.

Three studies were carried out: the development of a cavity FEA model, the development of a cavity string FEA model, and the hammer test of the C100-10R at the CMTF. The cavity FEA model was developed using geometry provided by Jefferson Labs. A quality mesh was developed from this geometry and known material properties were applied. The resulting model was found to accurately predict two out of seven modes of the cavity in a simply supported configuration.

Once done, a cavity string FEA model was developed leveraging the cavity FEA model. This also involved geometry provided by Jefferson Labs but was extensively defeatured and simplified. A mesh of a sufficiently low node count but high quality was developed, though the resulting model was not found to accurately predict the modal behavior of a real cavity string. Even so, the modal behavior of a real cavity string inside the C100-10R cryomodule was captured during a hammer test while it was partially assembled and certain mode frequencies and shapes were identified.

To capture the impact of resonance on a real system, the C100-10R cryomodule was placed in the CMTF to characterize how the cryomodule becomes detuned. The RF detuning spectra during hammer hits and background noise was captured. The results of the hammer testing indicate two strong peaks at low frequencies (9-10 Hz and 22-23 Hz). These two frequencies were found to be nearly coincident to four instances of mechanical resonance found during the hammer testing done on the partially-assembled C100-10R. This evidence is offered to suggest that mechanical resonance from these two modes did contribute to RF detuning of the cryomodule.

As a part of the CMTF test event, the effects of the BNNT canisters were captured. This was done by performing an identical set of hammer tests and noise recordings on the cryomodule with and without the BNNT canisters engaged. While these tests show promising results, the lurking variables in this experiment render these tests somewhat inconclusive.

5.2 Future Work

The first recommendation would be to continue improvement of the FEA models so that they can be used as a virtual test bed for prototype assessment.

It is also recommended to rerun the test of the BNNT canisters as described in Section 3.3 leveraging full run randomization. This is primarily because the cryomodule can be affected by its environment and the environment is able to change. Additionally, it has been recommended [38] to investigate the effects of the canisters on the quality factor Q of the cavities.

It would be recommended to identify other instances where resonance could lead to RF detuning. For example, could other components that contain high-power RF (say, the waveguides) cause detuning before the RF arrives at the cavity?

A possibly helpful investigation would be to consider the effects of simple resonators. A test of this nature has been performed at Jefferson Labs by Owen [39]. It may be possible to correlate RF detuning to the resonant frequency of simple resonators and that restricting their motion would yield improvement.

REFERENCES

[1] A. Seryi, *Unifying Physics of Accelerators, Lasers and Plasma*. Boca Raton, FL: Taylor & Francis Group, 2016.

[2] "Science." Thomas Jefferson National Accelerator Facility. https://www.jlab.org/research/science (accessed 2023).

[3] J. R. Delayen, "Phase and Amplitude Stabilization of Superconducting Resonators," Ph.D. thesis, Physics, California Institute of Technology, Pasadena, California, 1978.

[4] N. Banerjee, Hoffstaetter, G., Liepe, M., Quigley, P., Zhou, Z., "Active Suppression of Microphonics Detuning in High Q_L Cavities," *Physical Review. Accelerators and Beams*, vol. 22, no. 5, 2019.

[5] N. R. Usher, "Digital Low-Level Radio Frequency Control and Microphonics Mitigation of Superconducting Cavities," M.S. thesis, Department of Electrical and Computer Engineering, Michigan State University, 2007.

[6] J. A. Diaz Cruz, Biedron, S. G., Martines-Ramon, M., Sosa, S. I., Pirayesh, R., "Studies in Applying Machine Learning to LLRF and Resonance Control in Superconducting RF Cavities," presented at the Low-Level RF Workshop, Chicago, Illinois, 2019.

[7] J. C. Slater, "Microwave Electronics," *Reviews of Modern Physics*, vol. 18, no. 4, pp. 441-512, 1946.

[8] J. C. Slater, *Microwave Electronics*. D. Van Nostrand Company, Inc., 1950.

[9] C. Contreras-Martinez, "Electromagnetic and Mechanical Properties of Medium β SRF Elliptical Cavities," Ph.D. thesis, Michigan State University, 2021.

[10] T. H. Kandil, "Adaptive Feedforward Cancellation of Sinusoidal Disturbances in Superconducting Radio Frequency Cavities," M.S. thesis, Department of Electrical and Computer Engineering, Michigan State University, 2005.

[11] J. R. Delayen, "Ponderomotive Instabilities and Microphonics—a Tutorial," *Physica. C, (Superconductivity and its Applications)*, vol. 441, no. 1, pp. 1-6, 2006.

[12] S. Posen, Liepe, M., "Mechanical Optimization of Superconducting Cavities in Continuous Wave Operation," *Physical Review Special Topics - Accelerators and Beams*, vol. 15, 2012.

[13] X. Zhang, Sha, P., Pan, W., Zhai, J., Li, Z., Dong, C., Zheng, H., Mi, Z., He, X., Ge, R., Han, R., Sun, L., "The Mechanical Design, Fabrication and Tests of Dressed 650 MHz 2-Cell Superconducting Cavities for CEPC," *Nuclear Instruments & Methods in Physics Research. Section A, Accelerators, Spectrometers, Detectors and Associated Equipment*, vol. 1031, 2022.

[14] W. Schappert, "Resonance Control for Future Linear Accelerators," presented at the Linear Accelerator Conference, East Lansing, MI, 2016.

[15] H. Luck, Trepp, C., "Thermoacoustic Oscillations in Cryogenics. Part 1: Basic Theory and Experimental Verification," *Cryogenics*, vol. 32, no. 8, 1992.

[16] H. Luck, Trepp, C., "Thermoacoustic Oscillations in Cryogenics. Part 2: Applications," *Cryogenics*, vol. 32, no. 8, 1992.

[17] H. Luck, Trepp, C., "Thermoacoustic Oscillations in Cryogenics. Part 3: Avoiding and Damping of Oscillations," *Cryogenics*, vol. 32, no. 8, 1992.

[18] B. J. Hansen, Al Atassi, O., Bossert, R., Einstein-Curtis, J., Holzhauer, J., Hughes, W., Hurd, J., Kaluzny, J., Klebaner, A., Makara, J., Pischalnikov, Y., Schappert, W., Stanek,

R., Theilacker, J., Wang, R., White, M. J., "Effects of Thermal Acoustic Oscillations on LCLS-II Cryomodule Testing," presented at the IOP Conference Series. Materials Science and Engineering, 2017.

[19] H. Padamsee, *RF Superconductivity*. Weinheim, Germany: WILEY-VCH Verlag GmbH & Co. KGaA, 2009.

[20] H. Padamsee, "Superconducting Radio-Frequency Cavities," *Annual Review of Nuclear and Particle Science*, vol. 64, pp. 175-196, 2014.

[21] G. Davis, Delayen, J., Drury, M., Hiatt, T., Hovater, C., Powers, T., Preble, J., "Microphonics Testing of the CEBAF Upgrade 7-Cell Cavity," 2001.

[22] F. Qiu, Zhu, Z., Ma, J., Jiang, T., Xue, Z., Gao, Z., Chen, Q., Xu, C., Huang, G., He, Y., Michizono, S., Matsumoto, T., Miura, T., "An Approach to Characterize Lorentz Force Transfer Function for Superconducting Cavities," *Nuclear Instruments & Methods in Physics Research. Section A, Accelerators, Spectrometers, Detectors and Associated Equipment,* vol. 1012, 2021.

[23] P. Echevarria, Aldekoa, E., Jugo, J., Neumann, A., Ushakov, A., Knobloch, J., "Superconducting Radio-Frequency Virtual Cavity for Control Algorithms Debugging," *Review of Scientific Instruments*, vol. 89, no. 8, 2018.

[24] M. Keikha, Moallem, M., Zhu, G., Fong, K., "Microphonic Noise Cancellation in Super-Conducting Cavity," presented at the Conference of the IEEE Industrial Electronics Society, Lisbon, Portugal, 2019.

[25] S. Simrock, Petrosyan, G., Facco, A., Zviagintsev, V., Andreoli, S., and Paparella, R., "First Demonstration of Microphonic Control of a Superconducting Cavity with a Fast Piezoelectric Tuner," presented at the Particle Accelerator Conference, 2003.

[26] S. Zimmermann, "Active Microphonic Noise Cancellation in Radiation Detectors," *Nuclear Instruments and Methods in Physics Research Section A,* vol. 729, pp. 404–409, 2013.

[27] K. Davis, Matalevich, J., Powers, T., Wiseman, M., "Vibration Response Testing of the CEBAF 12 GeV Upgrade Cryomodules," presented at the Linear Accelerator Conference, Tel-Aviv, Israel, 2012.

[28] A. Brandt, *Noise and Vibration Analysis: Signal Analysis and Experimental Procedures*. Hoboken, NJ: John Wiley & Sons, Ltd., 2011.

[29] *MATLAB*. (2019). The MathWorks, Inc. [Online]. Available: https://www.mathworks.com

[30] R. J. Allemang, "The Modal Assurance Criterion - Twenty Years of Use and Abuse," *Sound and Vibration*, vol. 37, no. 8, pp. 14-23, 2003.

[31] ANSYS, *Theory Reference*. Canonsburg, PA: ANSYS, Inc., 2022.

[32] ANSYS, *ANSYS Meshing User's Guide*. Canonsburg, PA: ANSYS, Inc., 2023.

[33] *Ansys® SpaceClaim 2023 R1*. (2023). ANSYS, Inc.

[34] ANSYS, *Mechanical User's Guide*. Canonsburg, PA: ANSYS, Inc., 2023.

[35] *Ansys® Mechanical 2023 R1*. (2023). ANSYS, Inc.

[36] D. Montgomery, *Design and Analysis of Experiments, International Student Version*, 8th ed. Singapore: John Wiley & Sons Singapore Pte. Ltd., 2013.

[37] *Design-Expert® Software*. (2023). Stat-Ease, Inc., Minneapolis, MN. [Online]. Available: www.statease.com

[38] R. R. Whitney, "Thesis Submission for Review by BNNT, LLC," C. Hull, Ed., ed, 2023.

[39] P. Owen, "Hammer Test of C100-10R Summary," Thomas Jefferson National Accelerator Facility, unpublished, 2023.

APPENDIX

A. C100-10R Cavity String Mode Shapes

A.1 Excitation at Point 5

A.1.1 Motion at 7 Hz

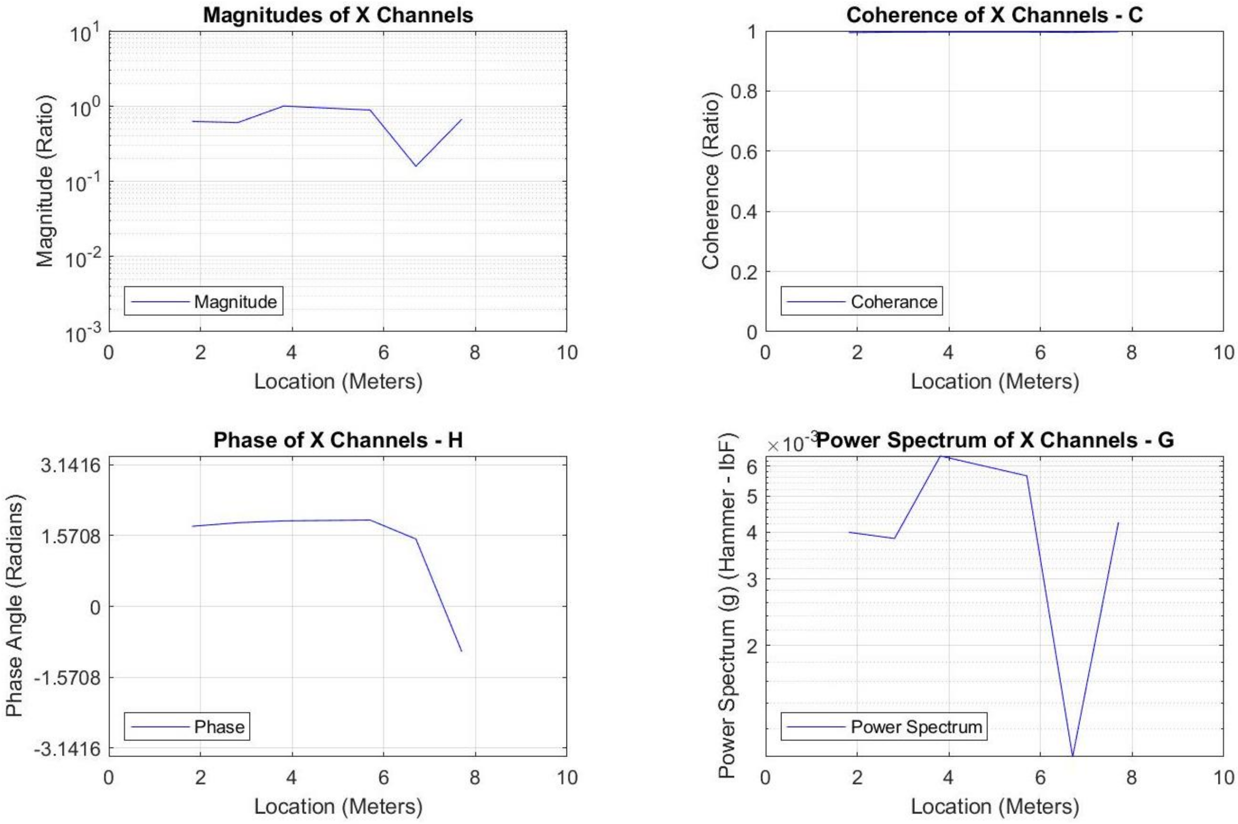

Figure 41: Cavity String ODS Shape, 7 Hz, Point 5 Excitation, X Direction

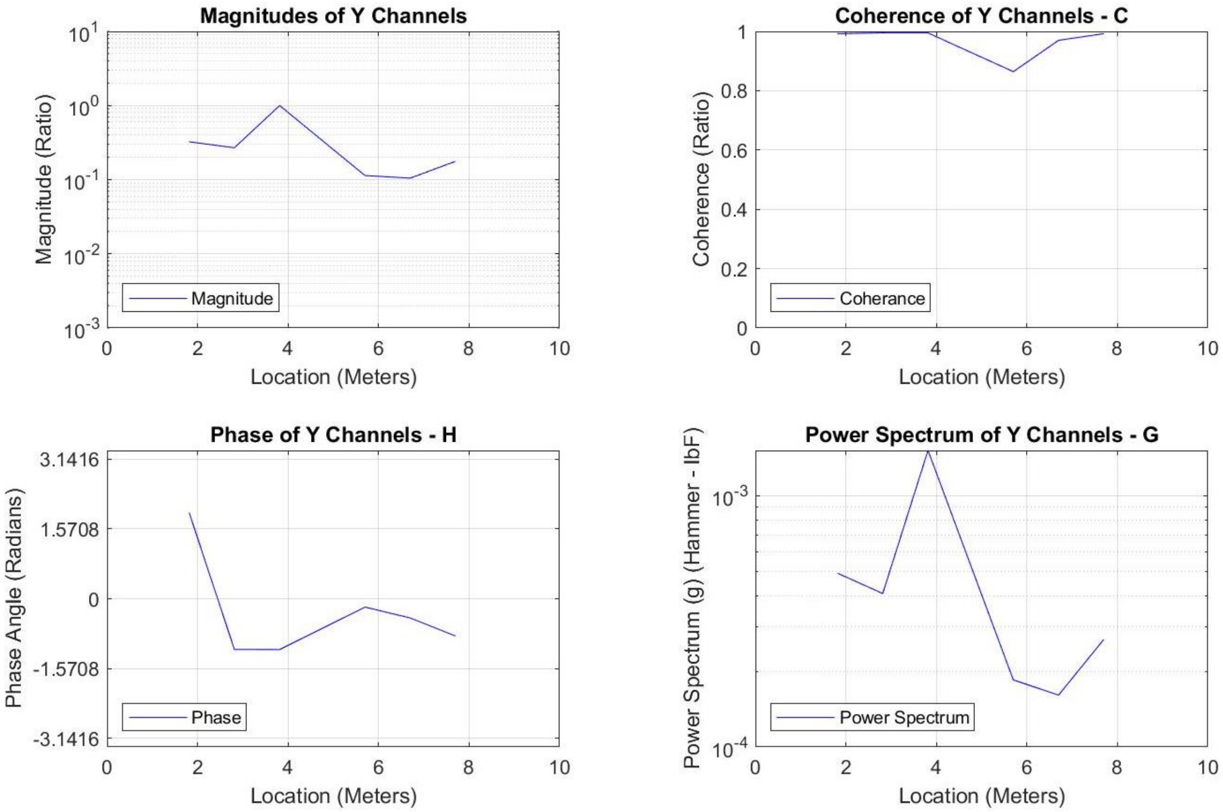

Figure 42: Cavity String ODS Shape, 7 Hz, Point 5 Excitation, Y Direction

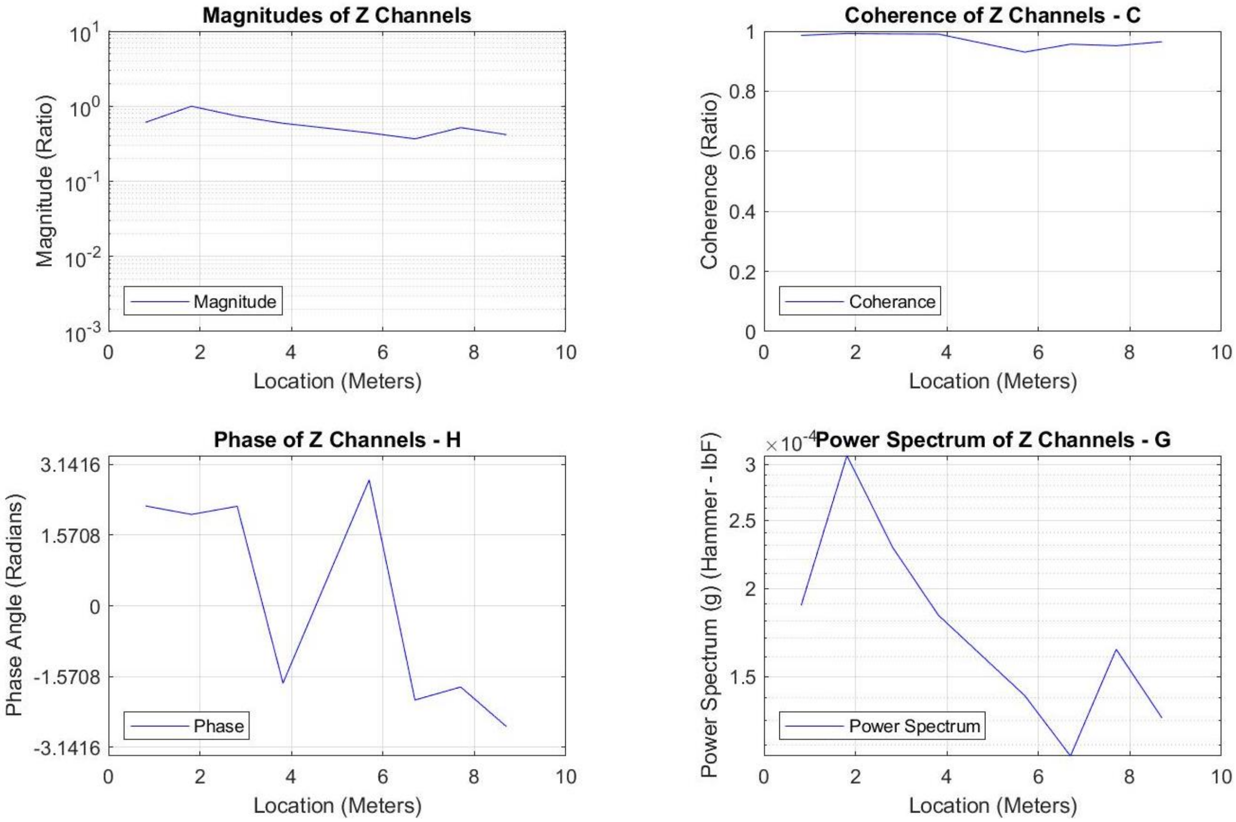

Figure 43: Cavity String ODS Shape, 7 Hz, Point 5 Excitation, Z Direction

A.1.2 Motion at 23 Hz

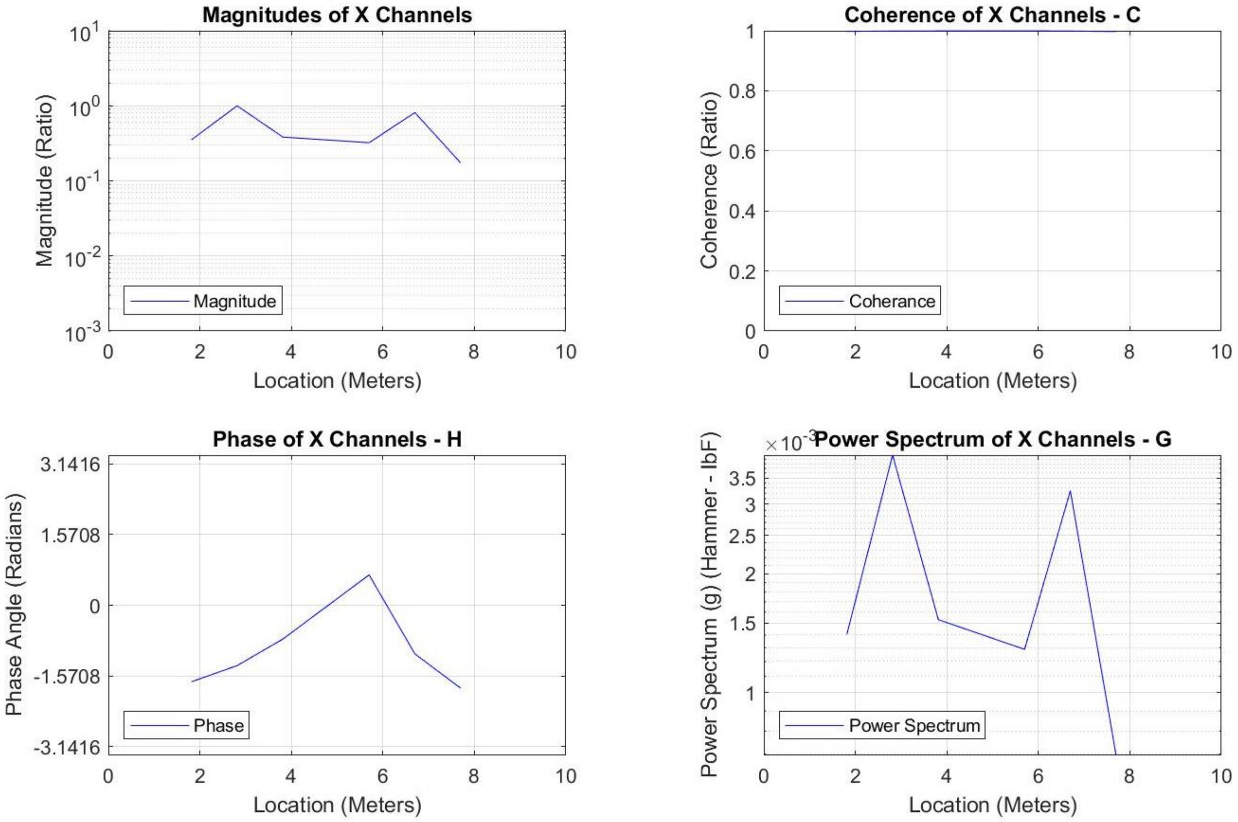

Figure 44: Cavity String ODS Shape, 23 Hz, Point 5 Excitation, X Direction

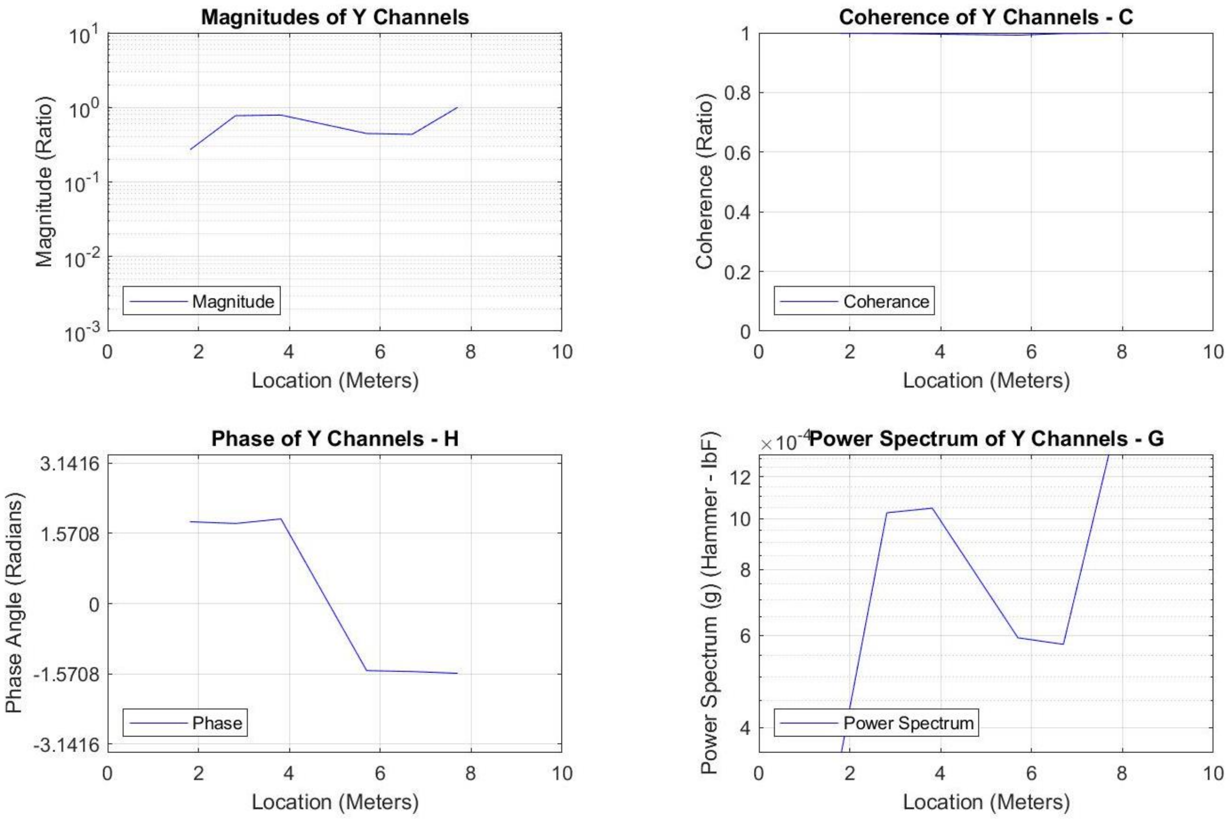

Figure 45: Cavity String ODS Shape, 23 Hz, Point 5 Excitation, Y Direction

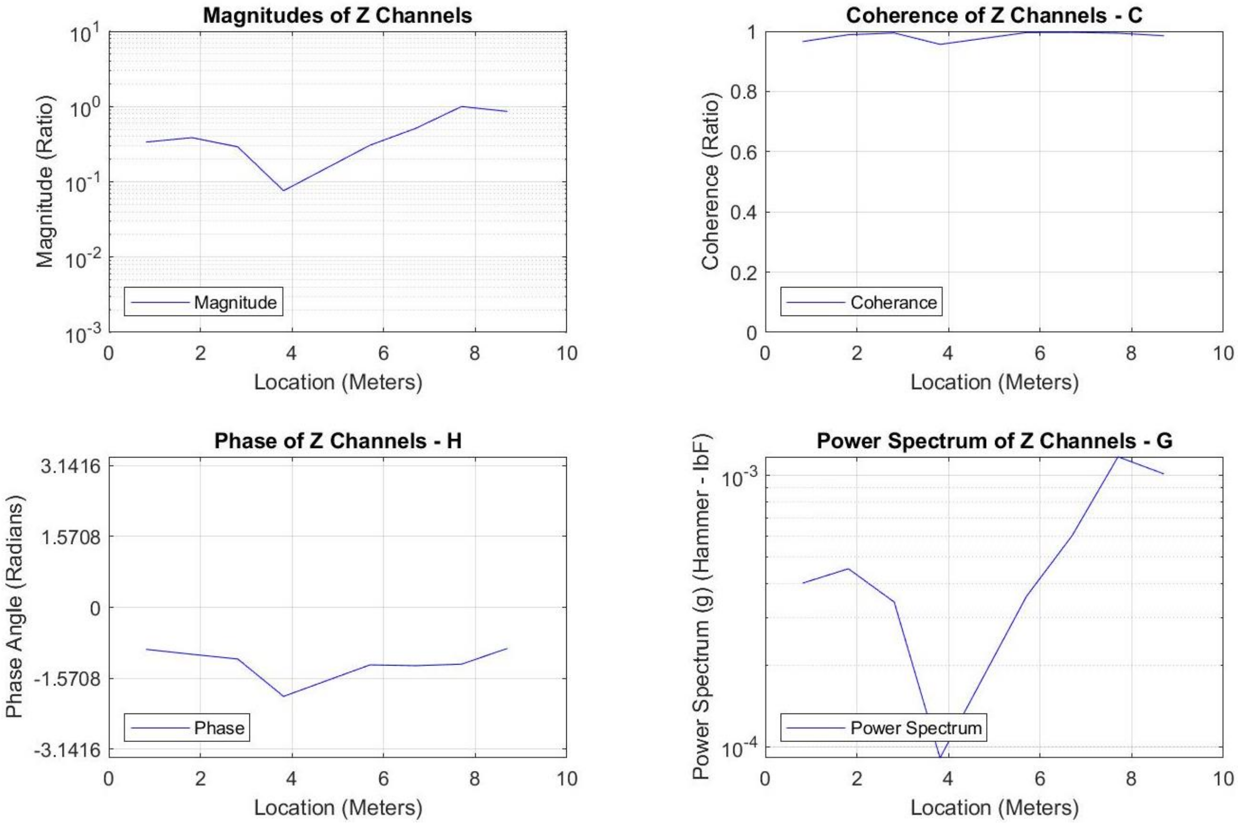

Figure 46: Cavity String ODS Shape, 23 Hz, Point 5 Excitation, Z Direction

A.2 Excitation at Point 7

A.2.1 Motion at 7.5 Hz

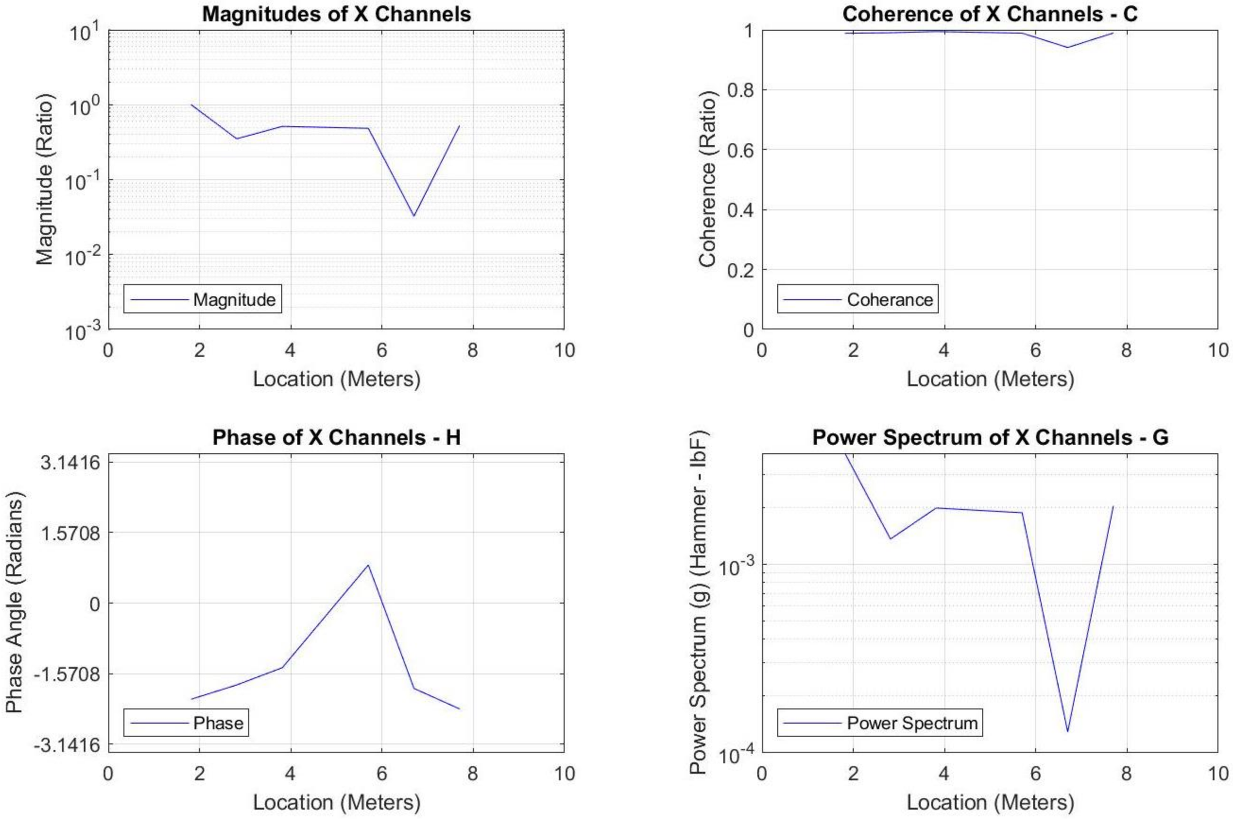

Figure 47: Cavity String ODS Shape, 7.5 Hz, Point 7 Excitation, X Direction

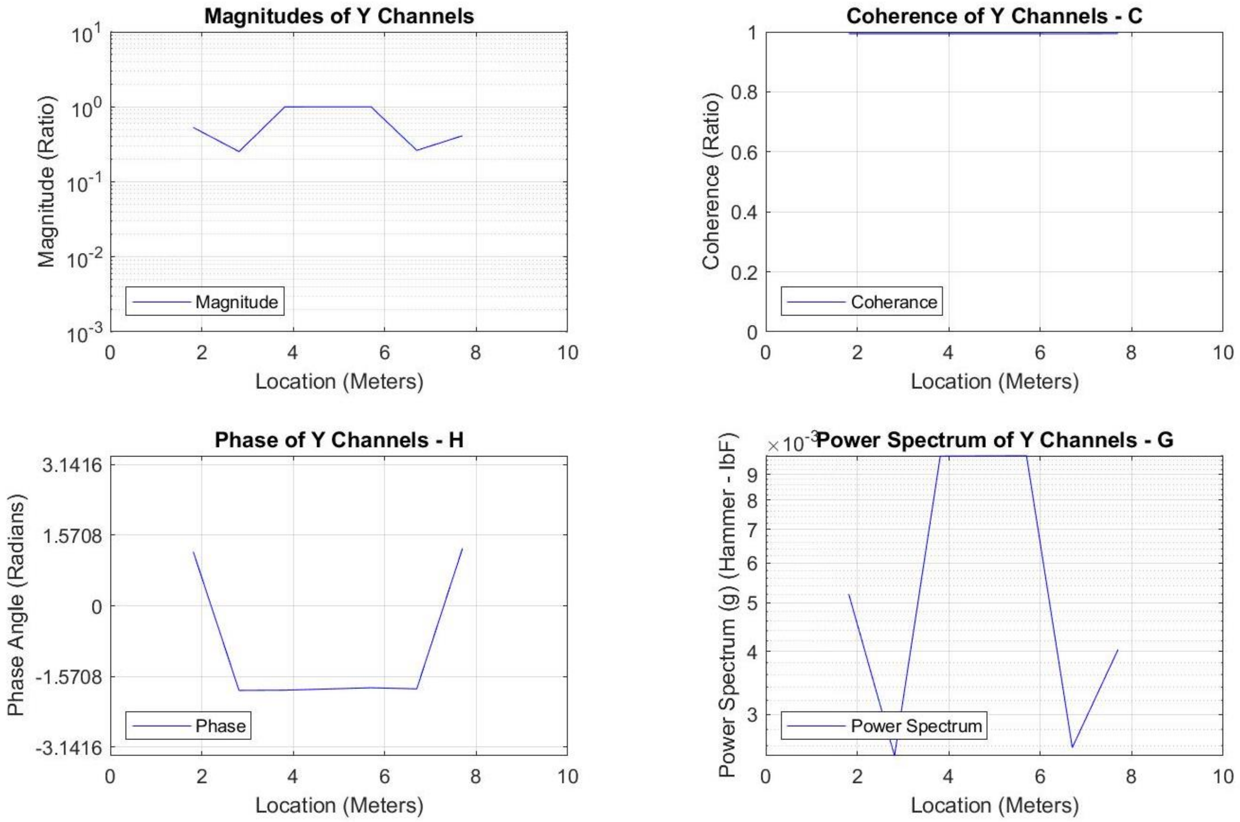

Figure 48: Cavity String ODS Shape, 7.5 Hz, Point 7 Excitation, Y Direction

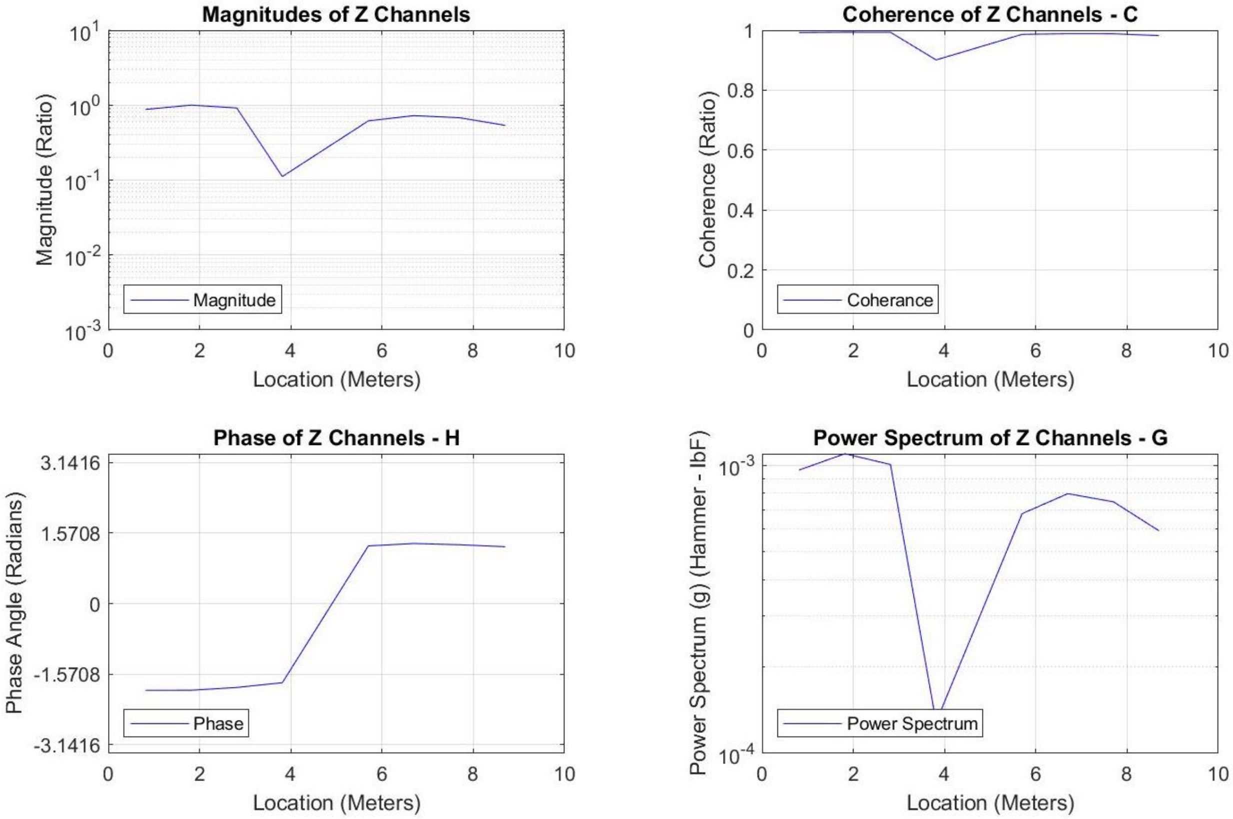

Figure 49: Cavity String ODS Shape, 7.5 Hz, Point 7 Excitation, Z Direction

A.2.2 Motion at 11 Hz

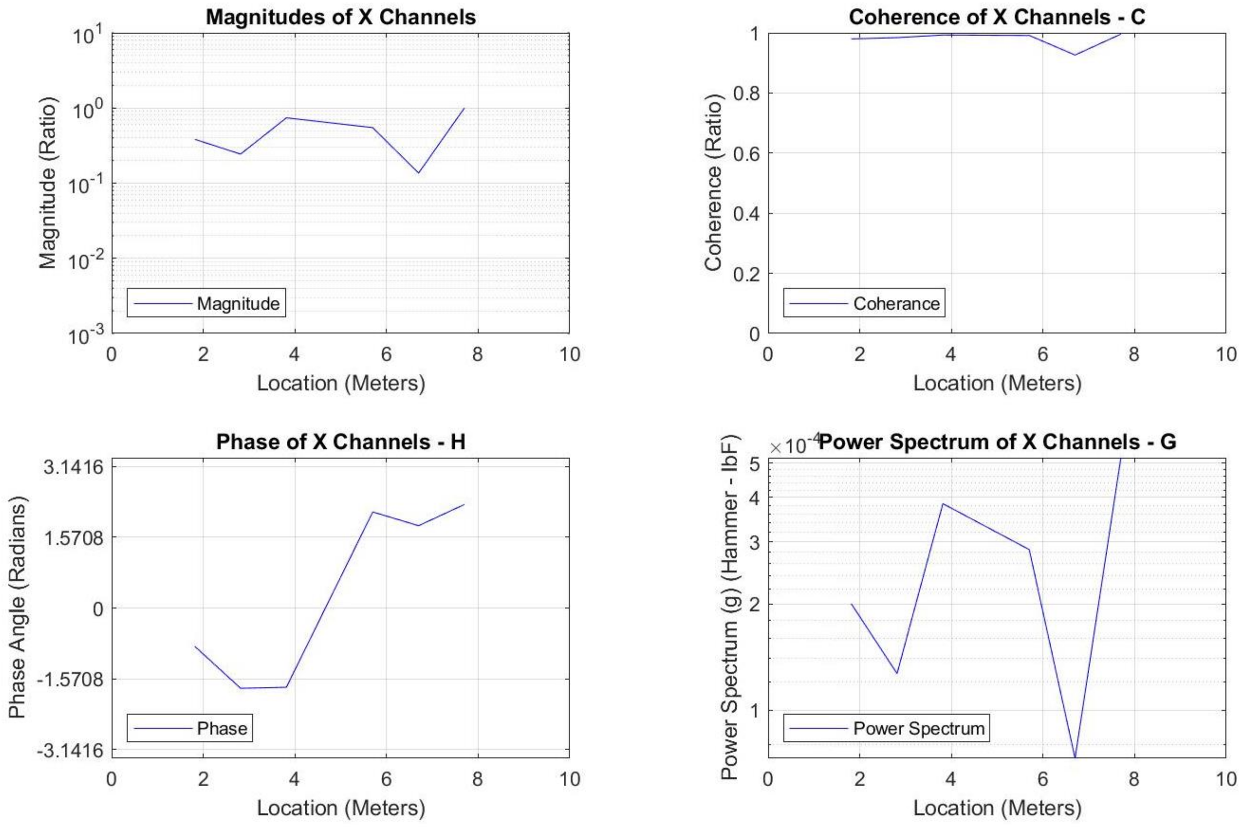

Figure 50: Cavity String ODS Shape, 11 Hz, Point 7 Excitation, X Direction

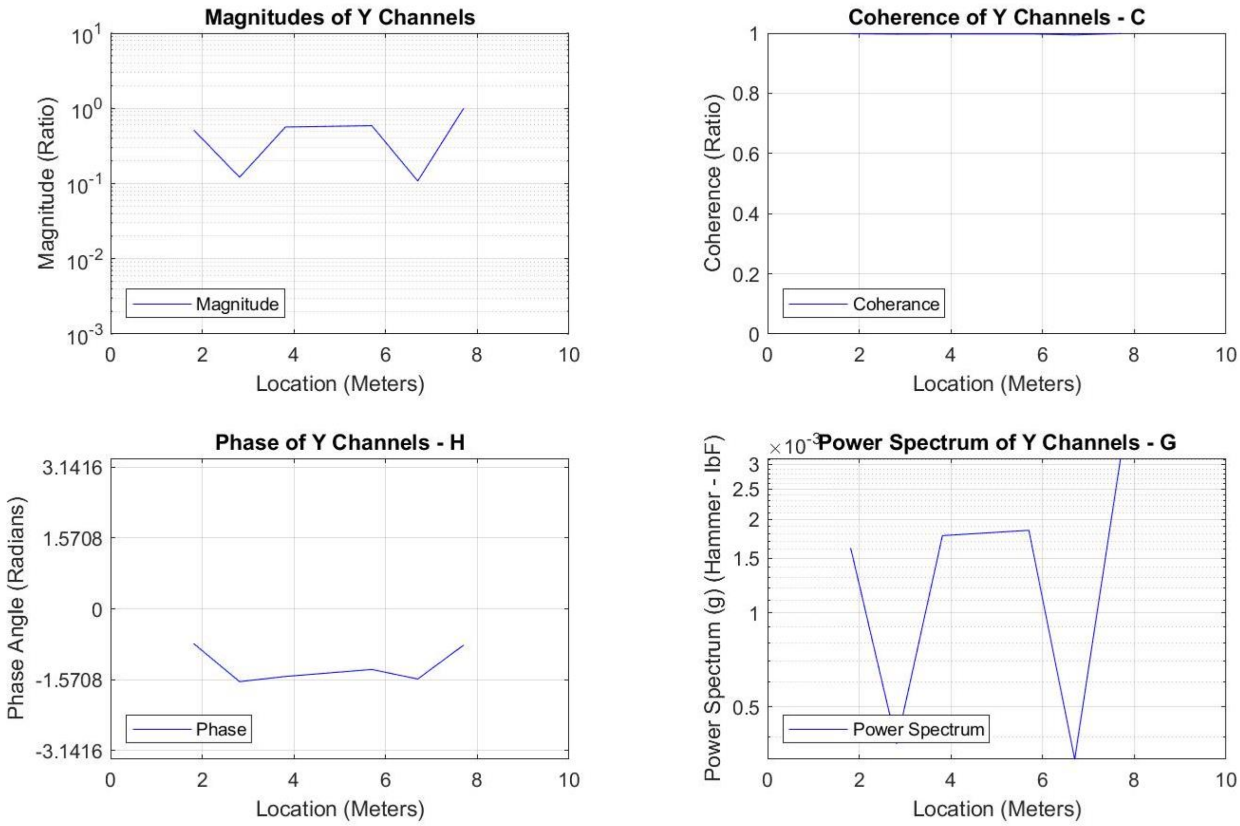

Figure 51: Cavity String ODS Shape, 11 Hz, Point 7 Excitation, Y Direction

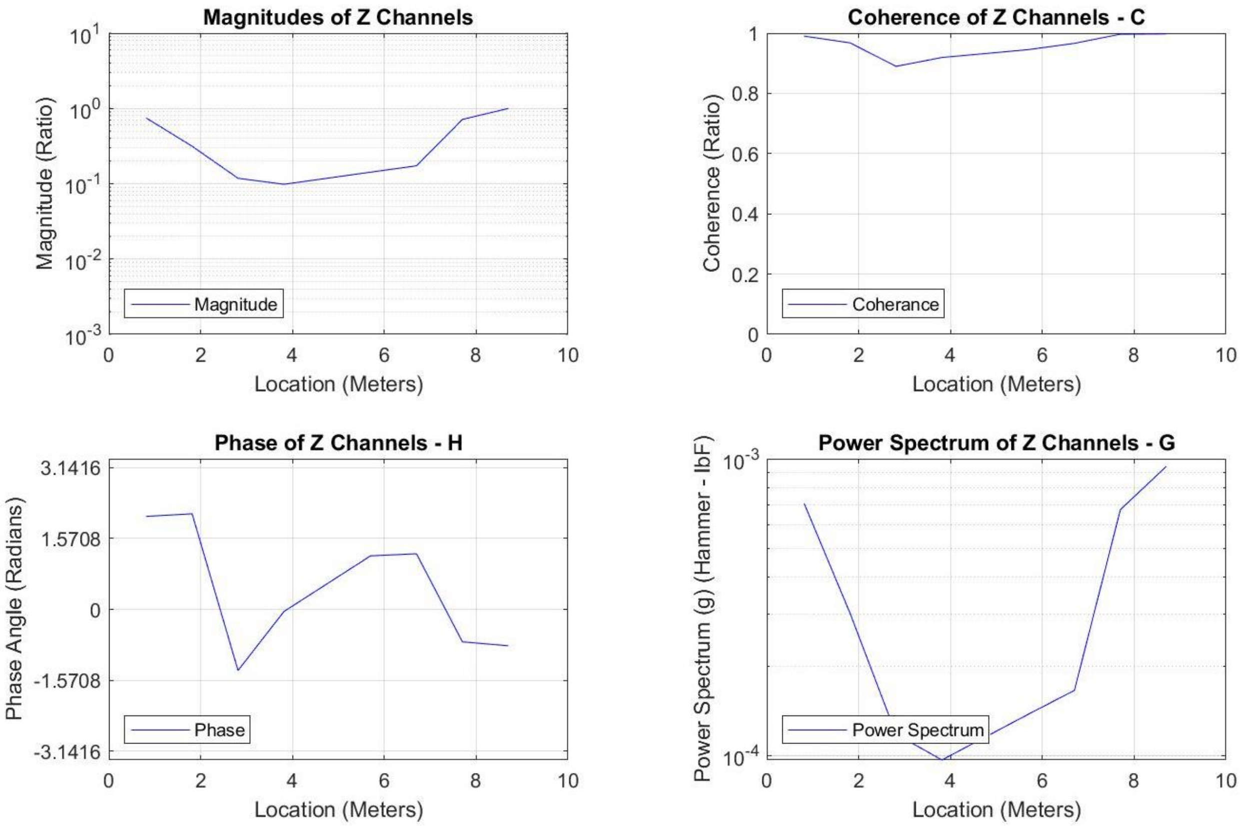

Figure 52: Cavity String ODS Shape, 11 Hz, Point 7 Excitation, Z Direction

A.2.3 Motion at 23 Hz

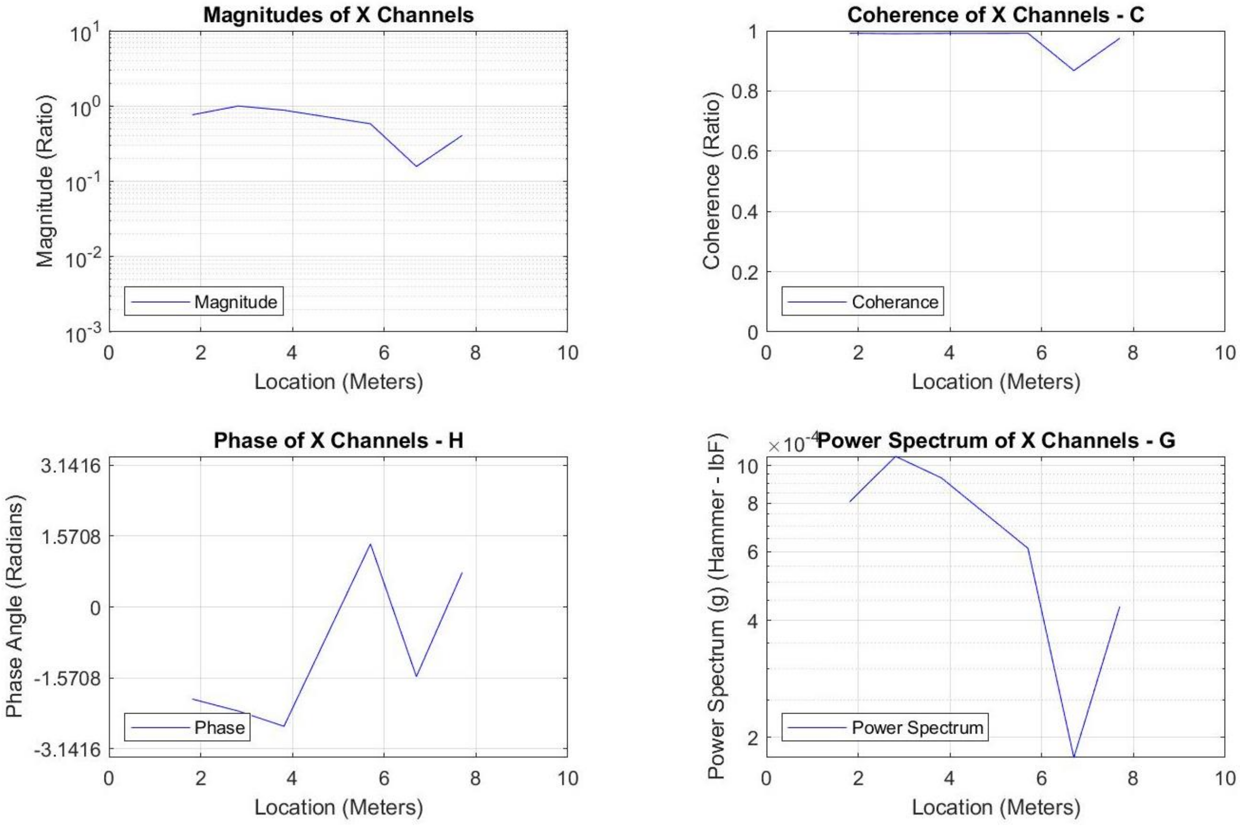

Figure 53: Cavity String ODS Shape, 23 Hz, Point 7 Excitation, X Direction

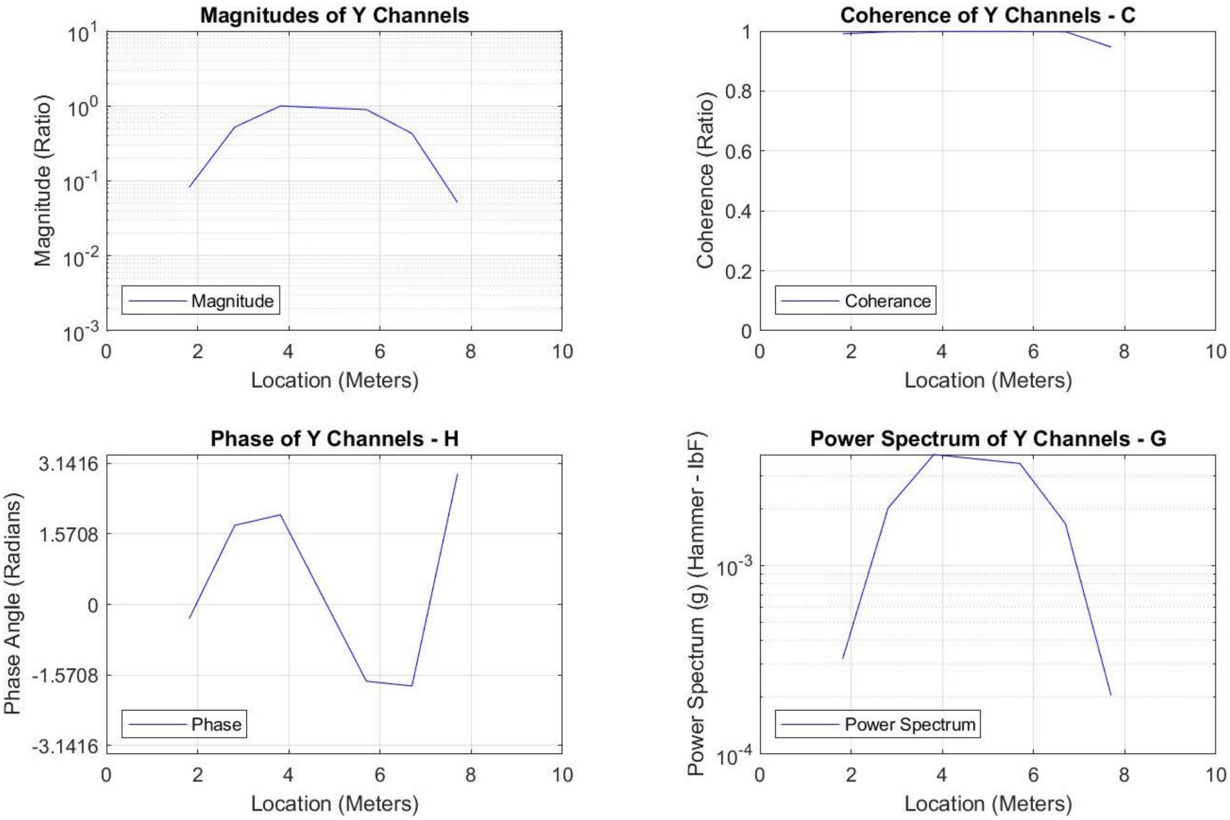

Figure 54: Cavity String ODS Shape, 23 Hz, Point 7 Excitation, Y Direction

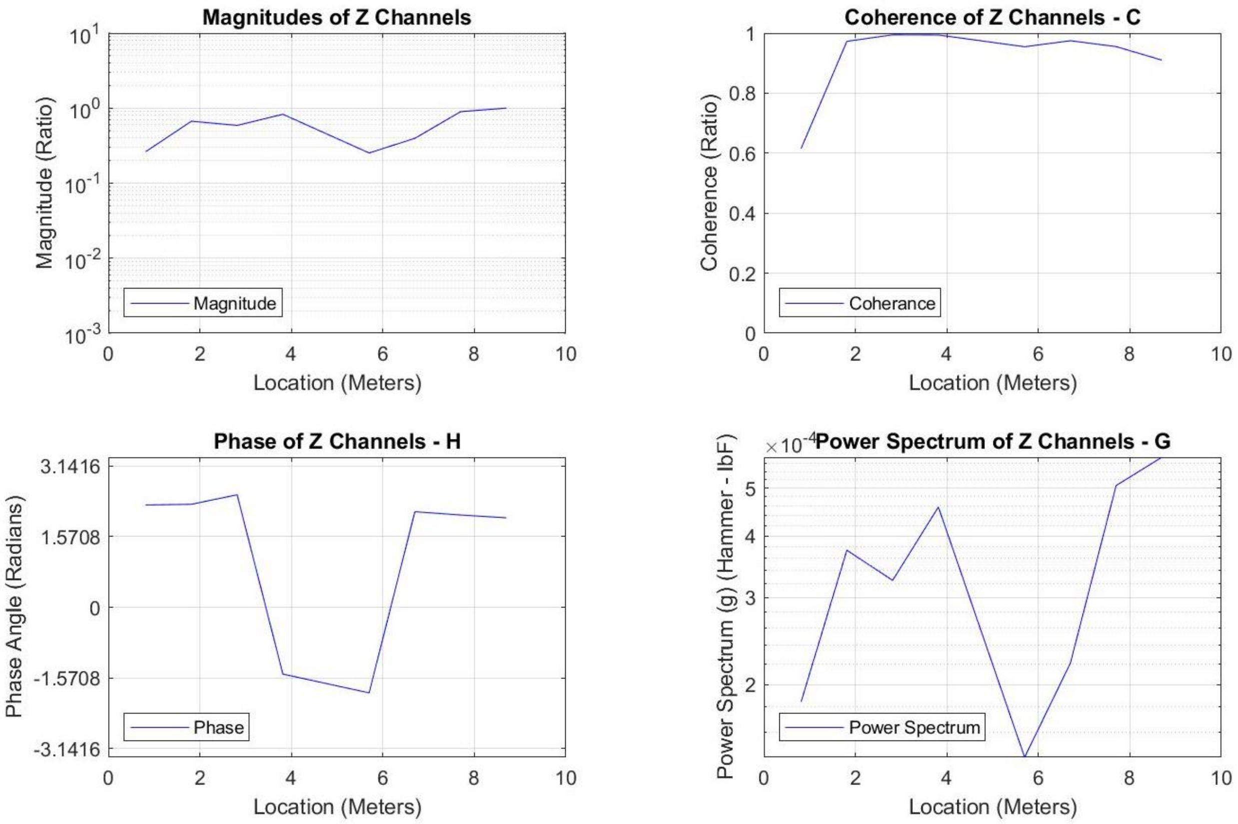

Figure 55: Cavity String ODS Shape, 23 Hz, Point 7 Excitation, Z Direction

A.3 Excitation at Point 2

A.3.1 Motion at 13 Hz

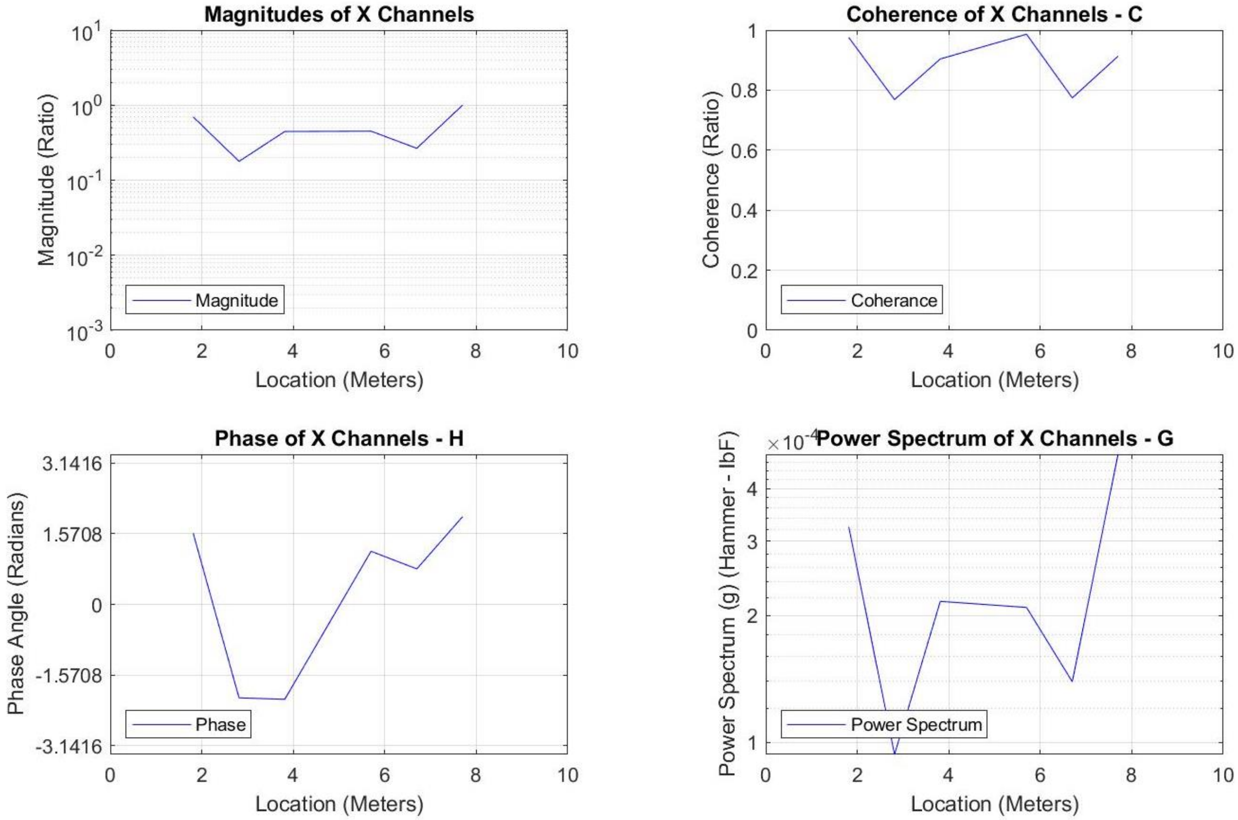

Figure 56: Cavity String ODS Shape, 13 Hz, Point 2 Excitation, X Direction

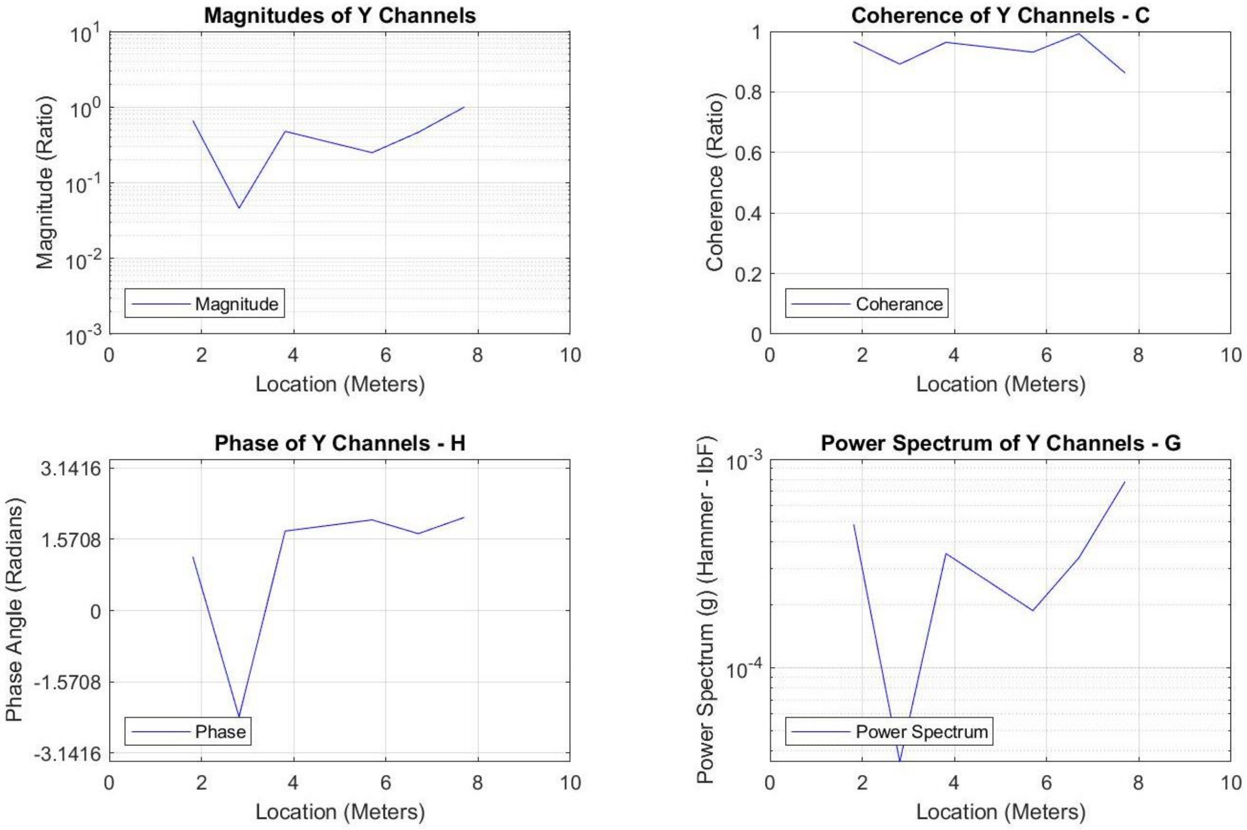

Figure 57: Cavity String ODS Shape, 13 Hz, Point 2 Excitation, Y Direction

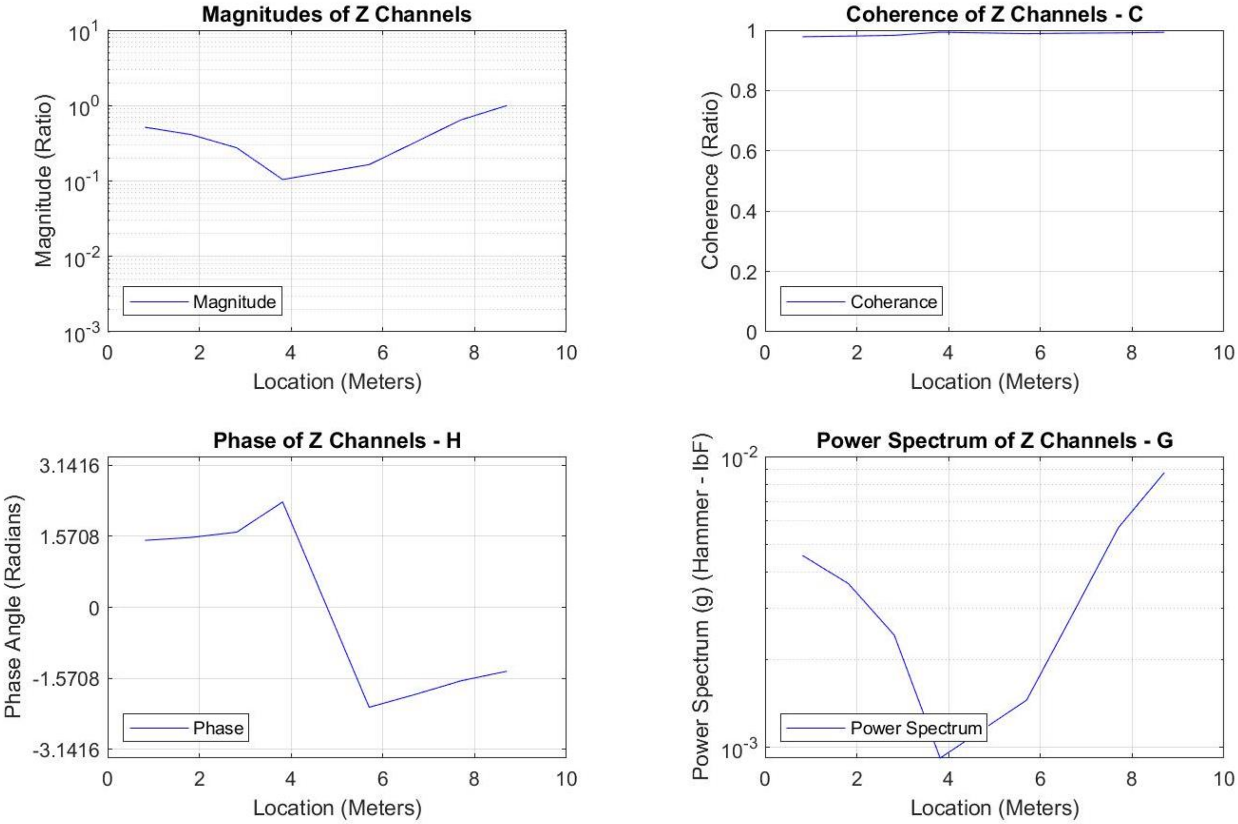

Figure 58: Cavity String ODS Shape, 13 Hz, Point 2 Excitation, Z Direction

A.3.2 Motion at 29 Hz

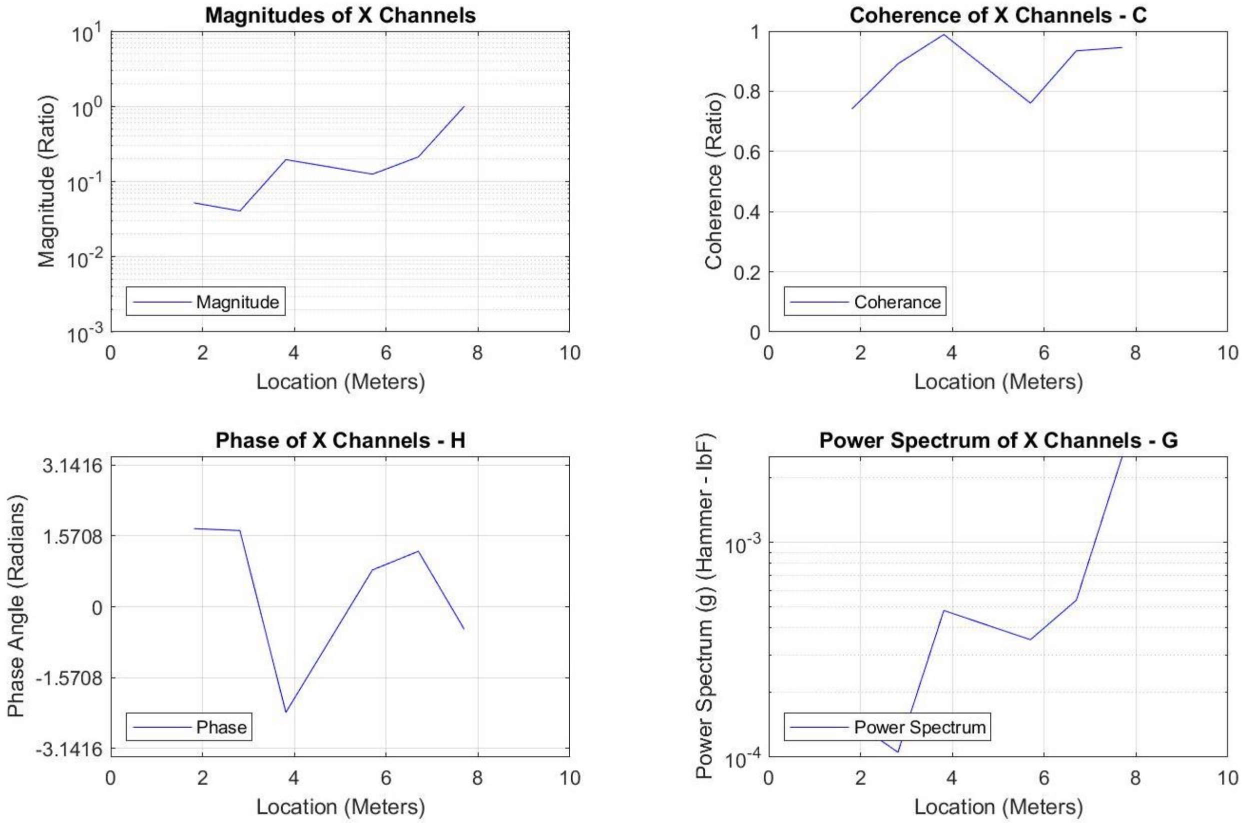

Figure 59: Cavity String ODS Shape, 29 Hz, Point 2 Excitation, X Direction

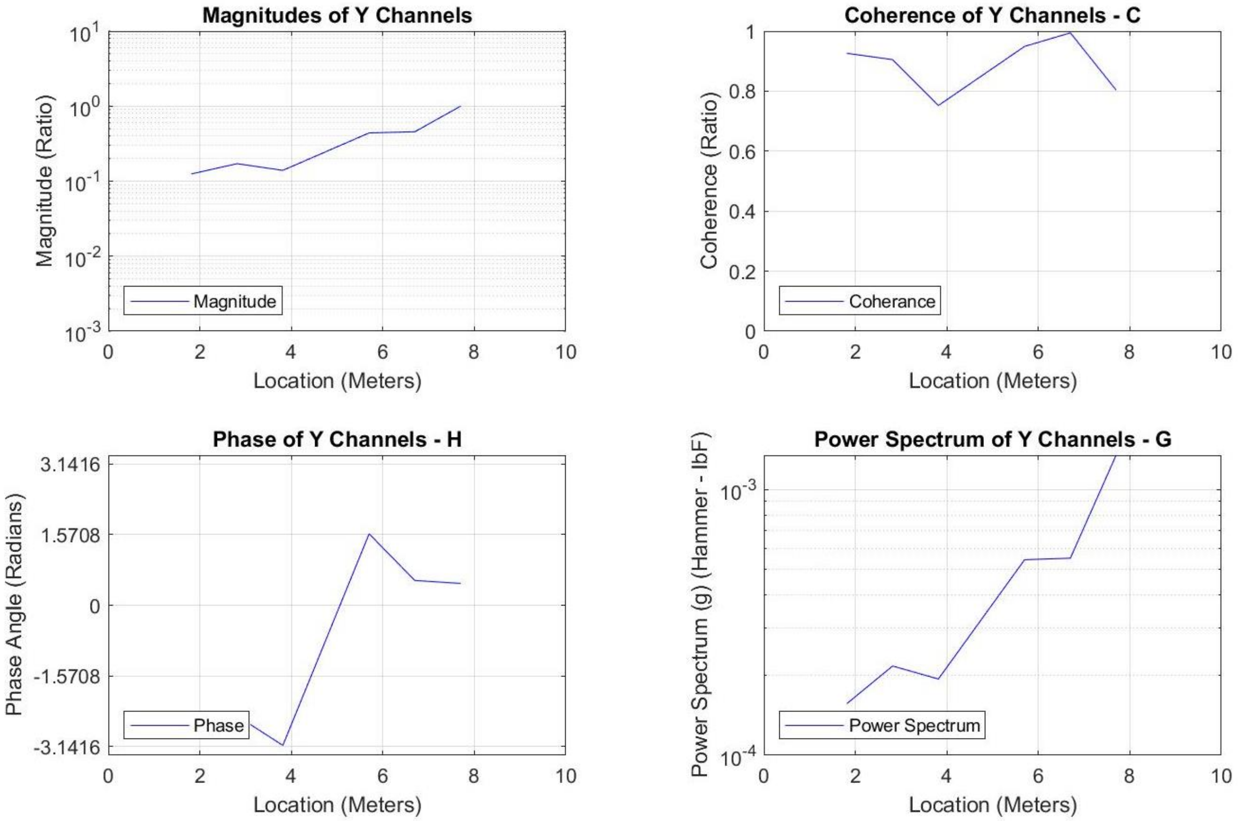

Figure 60: Cavity String ODS Shape, 29 Hz, Point 2 Excitation, Y Direction

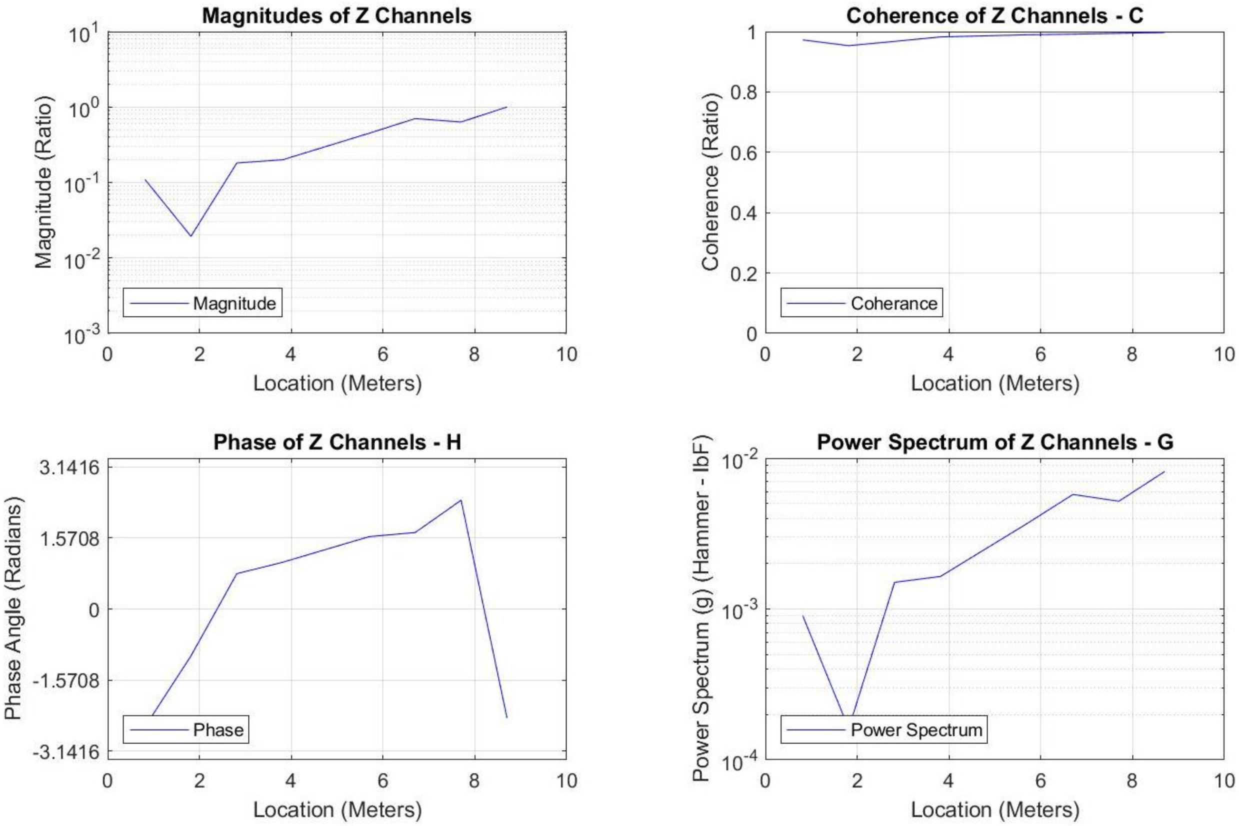

Figure 61: Cavity String ODS Shape, 29 Hz, Point 2 Excitation, Z Direction